RENORMALIZATION–GROUP THEORY OF QUANTUM PARTICULATE SYSTEMS

A Dissertation by

Ozan Sabahattin Sarıyer

Submitted to the
Graduate School of Sciences and Engineering
in partial fulfillment of the requirements
for the degree of

Doctor of Philosophy

in

Physics

Koç University

August, 2011

Koç University

Graduate School of Sciences and Engineering

This is to certify that I have examined this copy of a doctoral dissertation by

Ozan Sabahattin Sarıyer

and have found that it is complete and satisfactory in all respects,
and that any and all revisions required by the final
examining committee have been made.

Chair of Supervisory Committee: Prof. Dr. A. Nihat Berker:

Reading Committee:

Prof. Dr. A. Nihat Berker

Prof. Dr. Sondan Durukanoğlu Feyiz

Asst. Prof. Dr. Menderes Işkın

Asst. Prof. Dr. Alkan Kabakçıoğlu

Assoc. Prof. Dr. Özgür E. Müstecaplıoğlu

Date: August 25, 2011

ABSTRACT

The global phase diagram of the spinless Falicov–Kimball model in $d = 3$ spatial dimensions is obtained by renormalization-group theory. This global phase diagram exhibits five distinct phases. Four of these phases are charge-ordered phases, in which the system forms two sublattices with different electron densities. The charge-ordered phases occur at and near half-filling of the conduction electrons for the entire range of localized electron densities. The phase boundaries are second order, except for the intermediate and large interaction regimes, where a first-order phase boundary occurs in the central region of the phase diagram, resulting in phase separation (phase coexistance) at and near half-filling of both localized and conduction electrons. These coexistence regions are between different charge-ordered phases, between charge-ordered and disordered phases, and between dense and dilute disordered phases. The second-order phase boundaries terminate on the first-order phase transitions via critical endpoints and double critical endpoints. The first-order phase boundary is delimited by critical points. The cross-sections of the global phase diagram with respect to the chemical potentials and densities of the localized and conduction electrons, at all representative interactions, hopping strengths, and temperatures, are calculated and exhibit a multitude of distinct topologies.

PACS numbers: 71.10.Hf, 05.30.Fk, 64.60.De, 71.10.Fd

ÖZETÇE

Spinsiz Falicov–Kimball modelinin bütünsel faz diyagramı, $d = 3$ boyut için, renormalizasyon grubu kuramı kullanılarak elde edilmiştir. Bu bütünsel faz diyagramı beş ayrı fazı içermektedir. Bunlardan dördü yük-düzenli fazlardır ve bu fazlarda sistem farklı elektron yoğunluklarına sahip iki altörgüye bölünür. Lokalize elektron yoğunluğunun tüm değerleri için, yük-düzenli fazlar, iletim elektronları için yarı dolu bölgede ve civarında gözlemlenmektedir. Faz sınırları ikinci derecedir, ancak orta ve kuvvetli etkileşim rejimlerinde, faz diyagramının merkez bölgesinde birinci derece bir faz sınırı ortaya çıkar. Bunun sonucunda hem lokalize hem de iletim elektronları için yarı dolu bölge ve civarında faz ayrılığı (fazların birarada bulunması) olgusu gözlemlenir. Bu faz ayrılığı bölgelerinde, (a) farklı yük-düzenli fazlar, (b) yük-düzenli ve düzensiz fazlar, ve (c) farklı yoğun ve seyrek düzensiz fazlar birarada bulunur. İkinci derece faz sınırları, birinci derece faz geçişi üzerinde, kritik son noktalar ve çift kritik son noktalarla biter. Birinci derece faz sınırı kritik noktalarla sonlanır. Bütünsel faz diyagramının izdüşümleri, lokalize ve iletim elektronlarının kimyasal potansiyelleri ve yoğunlukları tabanında hesaplanmıştır. Bu izdüşümler, tüm etkileşimler, hoplama kuvvetleri ve sıcaklıklar için hesaplanmıştır ve pek çok farklı ilinge (topoloji) sergilemektedirler.

ACKNOWLEDGMENTS[1]

I would like to thank my supervisor, Prof. Dr. A. Nihat Berker (Sabancı University), not only for his scientific guidance throughout my studies in physics, but also for being such an excellent idol showing me which paths to follow for the rest of my research career, and my life in general. These paths pass through a range of critical issues, from ethics to collaboration, from reasoning to hardworking, and so on. Professor Berker influenced my character on a large scale, and helped me to become who I am now. It is a great honor for me to be the first full *doctorant* of him in Turkey. I acknowledge his endeavor and will take a great effort to deserve this support, that began from the very first day we met eleven years ago.

My parents and my sister have always been with me supporting my ideas, my beliefs and my way of life. Words of thanks would be inadequate to remark their support. I consider myself lucky for having parents who encouraged me when I realized that the answers to my questions, the roots of my curiosity can be found in physics.

I learned much of my practical knowledge on scientific computing and applications of renormalization-group theory from Dr. Michael Hinczewski (University of Maryland). I would like to thank him for being such a perfect teacher, a collaborator, and a friend as well. During my doctoral studies, Douwe J. Bonthuis and Klaus F. Rinne, from Prof. Dr. Roland R. Netz' group, helped me much to establish my working knowledge on molecular dynamics simulations. I would like to thank Professor Netz (Technical University Munich) for opening up the opportunity.

Our scientific discussions with Assoc. Prof. Dr. Alkan Kabakçıoğlu (Koç University) and Asst. Prof. Dr. Menderes Işkın (Koç University), on my research subject during our periodic meetings, helped me to improve this thesis dissertation, and I grabbed a lot from their way of critical thinking. I am thankful to them both, for they teached me different ways of handling a physics problem. I should also note that our discussions with Ulaş S. Gökay (Koç University), Seçkin Sefi (Max Planck Institute for the Science of Light), and Pamir Talazan (TÜBİTAK–TBAE)

[1]FINANCIAL SUPPORT BY THE SCIENTIFIC AND TECHNOLOGICAL RESEARCH COUNCIL OF TURKEY (TÜBİTAK) UNDER GRANT NO. 108 T 491 AND THE SCIENTIST SUPPORTING OFFICE TÜBİTAK-BİDEB IS GRATEFULLY ACKNOWLEDGED.

on the phase diagrams I calculated and on fundemantal physics in general, from quantum teleportation to complexity, from chaos theory to cosmology, cultivated my overview of science.

Without the *Gilgamesh* cluster at Feza Gürsey Institute (TÜBİTAK–TBAE), this dissertation would have never been published. I would like to acknowledge the hospitality of the Institute and the efforts of both Dr. Hinczewski and Pamir Talazan to keep the Gilgamesh up and running all the time. Whenever I went trouble with the cluster, I knew that Michael or Pamir were always there for a call of technical support, whether it is day or night.

I enjoyed very much to study at Koç University, where any kind of financial, technical, or mental support is unexceptional. I would like to thank all the academic and the administrative personnel of Koç University, especially Prof. Dr. Tekin Dereli, director of the Graduate School of Sciences and Engineering. It will be an honor for my whole life to be the first doctoral graduate of Koç University Physics Programme. The quiet atmosphere around the campus and the delightful ambiance of friendship at Koç University also helped me much in carrying through my doctoral studies.

The pleasant housing policy of the University allowed me to easily get in touch a fellow graduate student when I need to. I would like to thank Fatih Pelik, Ramazan Uzel, Şeyda İpek, Ahad Khaleghi, Mustafa Gündoğan, Utkan Gündoğdu, Evren Karakaya, Neşe Aral, Yasa Ekşioğlu, Zeynep Özkul, Yeliz Akça, Seçil Gürkan, Ulaş S. Gökay, A. Ümit C. Hardal, Duygu Can, Osman Dülek, Hasan Yılmaz, Ersin Hüseyinoglu, A. Tolga Görgülü, Ekin Karayiğit, and many others, who formed the intimate cloud around me, as soon as I moved to Koç University.

I should also mention the names, Aykut Erbaş, Pamir Talazan, Burcu Yücesoy, Cem Ersöz, Seçkin Sefi, Can Güven, C. Nadir Kaplan, Erhan Onfidan, Bilâl S. Oğuz, Barış Avşaroğlu, Durşen Saygın Hinczewski, Volkan Barmakçı, Laura Barmakçı, M. Cenk Uçar, Bora Coşkun, and many other friends that I knew before moving to Koç University, for their great support during my stay in Istanbul, and visits to Antalya, Boston, Washington DC, and Munich.

Last but not least, I would like to especially thank Neslihan Oflaz, for always being with me, encouraging, supporting, and tolerating me during my doctoral studies.

TABLE OF CONTENTS

LIST OF TABLES

LIST OF FIGURES

NOMENCLATURE

MIT	metal-insulator transition
RG	renormalization-group
FKM	Falicov–Kimball model
SFKM	spinless Falicov–Kimball model
CO	charge-ordering
CNT	carbon nanotube
MD	molecular dynamics

Chapter 1

INTRODUCTION

The Falicov–Kimball model has been a long standing problem in condensed matter physics, still lacking rigorous results particularly in finite $d > 1$ dimensions for finite-temperatures. In this thesis, we calculated the global phase diagram of the model in the spinless case for all interactions and temperature regimes. The outline of this thesis is as follows:

In Chapter 2, we first establish briefly the central concerns of the condensed matter physics, starting from the discovery of electron, following by various theoretical attempts to solve the physics of conducting electrons in a condensed medium, which turns out to be greatly affected by the correlations between electrons. We introduce the strong electron correlation induced metal-insulator transition phenomenon on experimental grounds first. Next, Mott's theoretical explanation to the metal-insulator transition is discussed and the equivalent approach of Hubbard is introduced.

In Chapter 3, we introduce the second quantization formalism of the quantum field theory, in which the particles are considered as fields. This discussion is initiated with the elementary formalism of quantum mechanics (first quantization) and wrapped up with the introduction of tight-binding approximation for the quantum field theoretical fermionic creation and annihilation operators, that leads to the Hubbard model.

The following Chapter 4 is devoted to the discussion on renormalization-group theoretical methods. Practical techniques to calculate thermodynamic properties of a model system, such as densities, response functions, and phase diagrams associated by the model Hamiltonian, are provided. A whole discussion on renormalization-group theory is omitted, since it would take several volumes.

In the light of these chapters, in Chapter 5, we present our results on the global phase diagram of the spinless Falicov–Kimball model (SFKM), which is derived from the Hubbard model as a limiting case. Connection to experimental systems is provided as a conclusion. The charge-ordering phenomenon, that we capture within the SFKM, is an essential feature interplaying with the high-temperature superconductivity and colossal magnetoresistance. Therefore, understanding the nature of the charge-ordered phases would give a better physical insight on these types of phenomenon, that lies in the heart of condensed matter physics today.

As a final chapter, brief discussions on other problems, that the present author worked during the doctoral studies, are provided in Chapter 6. These problems include hard-spin mean-field theory of $\pm J$ spin glass model, sequence alignment via simulated anneling, and molecular dynamics of water flow through carbon nanotubes.

Chapter 2

METAL-INSULATOR TRANSITION

2.1 Conduction in metals: a brief histocal survey

2.1.1 Prologue

Metals have been of great importance throughout the history of mankind, since they exhibit fascinating physical properties. Their durability, ease of processing and abundancy on the Earth's crust led to some of the early innovations, and the periods following the Stone Ages are named after the main metals that were in weighted use by the prehistoric communities. Alongside these properties, their extraordinary thermal and electrical conductivity shaped the modern technological cloud around us. It is especially the low resistance of metals to electrical current that made them the main elements of almost all gadgets that we use in everyday life. The progress in semiconductor technology was the next step, that led us to the age of electronics and computers. But what determines a material to be a conductor (metal) or an insulator?

2.1.2 Free electron theories of metals

It was Thomson's experiments that yielded to the discovery of the electron in 1897 [1]. Three years later, in 1900, treating the electrons as classical particles that collide with stationary ions, and applying the kinetic theory onto this electron gas, Drude proposed a mechanism for electrical conductivity of metals [2, 3, 4]. Thus, it was understood that the "*free electrons*" detached from the ions were the source of low resistivity in metals. According to Drude model, current density and applied electric field are parallel and the linear proportionality is given by

$$\vec{J} = \frac{ne^2\tau}{m}\vec{E} \ , \tag{2.1}$$

where $\vec{J}$ is the current density, $\vec{E}$ is the electric field, n is the electron number density, e and m are the electron charge and mass, and τ is an adjustable parameter of the model, namely the mean-free-time between electron-ion collisions. We can define the conductivity, σ, as[1]

[1]We give the definition of the linear electrical conductivity here. We omit the anisotropy effects, which can be included by the definition of a conductivity tensor in three spatial dimensions.

$$\vec{J} = \sigma \vec{E} \ . \tag{2.2}$$

This results in the conductivity given by the Drude model as

$$\sigma = \frac{e^2 \tau}{m} n \ . \tag{2.3}$$

Thus, as the main result of the Drude model, the conductivity, σ, increases linearly with the increasing electron density, n.

Later in 1905, Lorentz rehashed the problem and treated the free electrons in a more rigorous fashion by describing the velocity distribution of moving electrons via Maxwell-Boltzmann statistics [5]. The Drude-Lorentz model essentially explains the DC and AC electrical conductivities, thermal conductivity, and Hall effect in metals. However, among many other phenomena, it fails to explain the specific heat due to mobile electrons. The model was further improved with the work of Sommerfeld [6], where the electrons are not considered as classical particles but as quantum mechanical fermions, in accord with the Pauli exclusion principle. Basically, the velocity distribution of classical particles obey the Maxwell-Boltzmann statistics, while one should consider the Fermi-Dirac distribution for fermionic particles. This consideration provided an improvement over the thermal properties of metals calculated in the Drude-Lorentz model. Furthermore, Sommerfeld predicted a mean-free-path in the order of 1 cm at room temperature, that is 10 times larger than the one predicted by Drude and Lorentz. These free electron theories of metals still lacked for the physical explanation of electron scattering mechanism and the reletively long distances travelled by free electrons between two successive scattering incidents. As a more important problem regarding the scope of this thesis, the free electron models are also unable to explain why some materials are insulators.

2.1.3 Bloch electrons and the band theory of metals

The electron-ion interactions are restricted only to the incidents of collisions in the free electron models. In fact this is the definition of the "*free electron approximation*". We can relax this assumption by considering a potential created by the ions

of the metal, and letting the electrons travel in this potential landscape instead of in a pure vacuum space between the ions. But what will determine the shape of this potential landscape?

It is demonstrated via X-ray diffraction by von Laue [7, 8, 9] and Bragg [10] that the metallic ions form a periodic structure in space. This crystal structure leads to a periodic potential created by ions given by

$$V(\vec{r}) = V\left(\vec{r} + \vec{R}\right) \ , \tag{2.4}$$

where $\vec{r}$ is a position vector and $\vec{R}$ can be any one of the Bravais lattice vectors corresponding to the underlying crystal structure. The electron-electron interactions can be further integrated into $V(\vec{r})$ to obtain an effective potential. Thus, one needs to examine the one-electron motion in this periodic potential by solving the Schrödinger equation

$$\mathscr{H}\psi = \left[-\frac{\hbar^2}{2m}\vec{\nabla}^2 + V(\vec{r})\right]\psi = E\psi \tag{2.5}$$

in order to obtain the metallic behavior. The periodicity of the potential $V(\vec{r})$ leads to a very important theorem, which states that the eigenstates of $\mathscr{H}$ have the form of a plane wave multiplied by a function with the periodicity of the underlying Bravais lattice. This is formally given as below:

Theorem 1. *The eigenstates of the Hamiltonian $\mathscr{H}$ given in* Eq.(2.5) *with a periodic potential given in* Eq.(2.4) *can be chosen as $\psi_{n,\vec{k}}(\vec{r} + \vec{R}) = \mathrm{e}^{\mathrm{i}\vec{k}\cdot\vec{R}}\psi_{n,\vec{k}}(\vec{r})$, for every Bravais lattice vector $\vec{R}$.*

This theorem is known as the "*Bloch theorem*" [11] and the electrons descibed by these periodic wave functions are called "*Bloch electrons*" that reduce to the free electrons in the case of $V = 0$, which is still periodic. The vectors $\vec{k}$ lie in the momentum space that is the Fourier transformed "*reciprocal lattice*" of the original Bravais lattice, and the examination can be restricted onto the "*first Brillouin zone*" of the reciprocal lattice without any loss of generality. This is a direct consequence of the periodicity in the "*direct lattice*".

Furthermore, there exists many independent eigenstates for each $\vec{k}$ and this is denoted by the index n of the wave functions defined in Theorem 1. This index is

called the "*band index*". The Bloch electrons in a periodic crystal yields different "*energy bands*" and thus the "*band theory of solids*".

Quite genarally, application of perturbation theory for a weak periodic potential, $V \ll E(\vec{k})$, suggests "*band gaps*" at the edges of the first Brillouin zone. A schematic picture of the dispersion curves for the first three bands of a one dimensional solid is given in Fig.2.1 below, where the striped regions denote the band gaps. Electrons cannot assume the energy values that lie inside these band gap regions. This yields to the definition of metals and insulators.

The number density of electrons or the energetic "*density of states*" determine the "*Fermi energy*" of the solid. When the electrons are filled into a band structure upto the Fermi energy level there are two possibilities in the broadest sense: (i) the electrons can exactly fill the last band, or in other words, the Fermi energy level may lie within a band gap; and (ii) the last band may be partially filled, *i.e.*, the Fermi level may be within an allowed band. The last band that

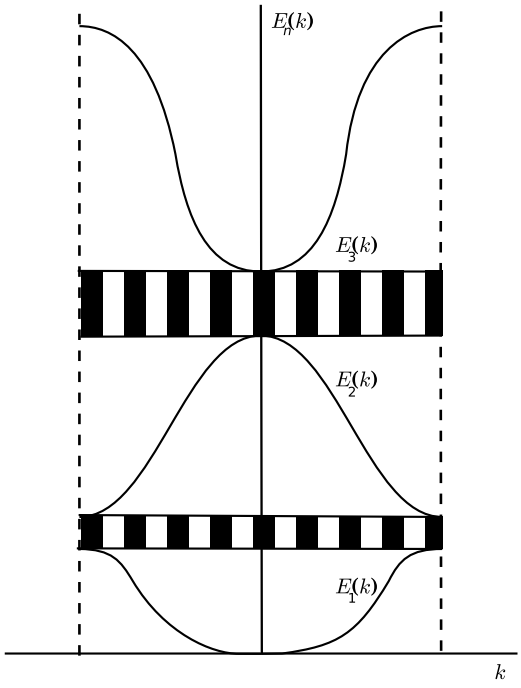

Figure 2.1: A schematic representation of the first three bands of a one-dimensional lattice in the reduced-zone scheme of the first Brillouin zone. The striped regions denote the band gaps that are forbidden for any electron.

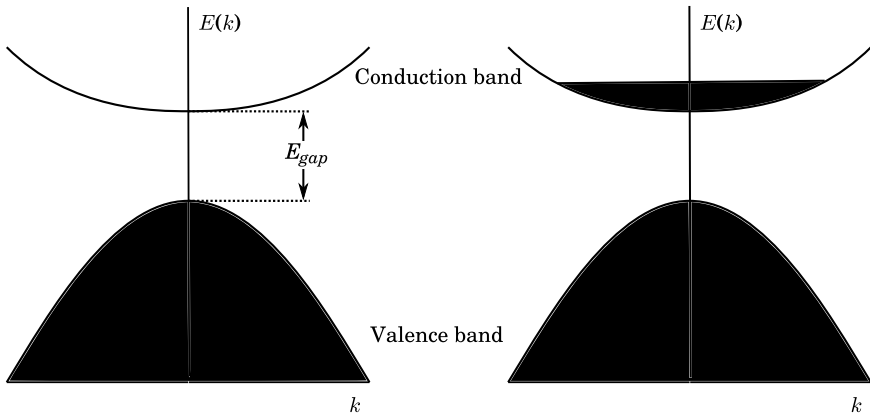

Figure 2.2: A schematic illustration of the bands filled with electrons (denoted by black filled regions) up to the Fermi energy level for an insulator on the left and for a metal on the right.

is completely filled with electrons is called the "*valence band*" and the next band is called the "*conduction band*". Thus, the two possibilities above mean that the conduction band can be either (i) comletely empty or (ii) partially filled. These two possibilities, illustrated in Fig.2.2 above, refer to an insulator and a metal respectively. In the metallic case there exist conduction electrons that can move within the material, while for the insulator, electrons in the valence band that are tightly bound to the ions must be excited to the conduction band by absorbtion of thermal or photonic energy, or by other means. In some cases, this can be easily achieved and those materials are called "*semiconductors*", which is a subject well outside the scope of this thesis. We will also not discuss the "*semimetal*" case for which the valence and conduction bands touch each other.

2.1.4 Tight-binding approximation

Both the free-electron and the Bloch electron models described above assume a common property. Both type of electronic models ignore the electron-electron interactions. However, in reality, the wave functions of the localized electrons may not vanish within the interatomic spacing and may overlap with the wave functions of the localized electrons in the nearby lattice points. This is actually the case especially for the electrons in the higher energy levels of nearest-neighboring atoms.

In the "*tight-binding approximation*" (also known as "*linear combination of atomic orbitals*" or "*LCAO*") these overlaps are taken into account [11, 12, 13, 14, 15, 16, 17, 18, 19, 20, 21, 22, 23, 24, 25].

The tight-binding approximation assumes that the independent "*atomic orbitals*" are known, and constructs the "*crystal orbitals*" via linear combination of atomic orbitals. Let us consider an independent one-atom Schrödinger equation given by

$$\mathscr{H}_{atom}\phi_n(\vec{r}) = \left[-\frac{\hbar^2}{2m}\vec{\nabla}^2 + V_{atom}(\vec{r})\right]\phi_n(\vec{r}) = E_n\phi_n(\vec{r}) \ , \tag{2.6}$$

where $\mathscr{H}_{atom}$ and $V_{atom}(\vec{r})$ are the single atomic Hamiltonian and potential respectively, while $\phi_n(\vec{r})$ is the single atomic orbital wave function. The crystal orbital wave functions that are the solutions to Eq.(2.5) are then formed as the linear combination of the localized atomic orbital wave functions as

$$\psi_{n,\vec{k}}(\vec{r}) = \frac{1}{\sqrt{N}}\sum_{\ell=1}^{N}\left[\mathrm{e}^{\mathrm{i}\vec{k}\cdot\vec{R}_\ell} \ \ \phi_n\left(\vec{r}-\vec{R}_\ell\right)\right] \ , \tag{2.7}$$

where the intoduction of Bloch wave vector $\vec{k}$, that can assume any point in the first Brillouin zone, allows the crystal orbital wave function to extend over the whole lattice. Here the sum runs over the whole set of possible Bravais direct lattice vectors. It is easy to show that this crystal orbital wave function satisfies the Bloch theorem (Theorem 1). The basis set that is used in the tight-binding approximation need not to be the atomic orbital wave functions set, but can assume any functions set that have the periodicity of the lattice. The atomic orbital set of $\{\phi_n(\vec{r})\}$, that actually form an orthonormal basis set, is the most effective one to work with and is called "*Wannier functions*" or "*Wannier states*".

2.1.5 Hartree–Fock theory

The tight-binding approximation is not the only way to deal with the electron – electron interactions. Another method is the "*Hartree–Fock theory*" that is basically a self-consistent field approximation, or in other words, a "*mean-field theory*". Considering both the electron – electron and electron – nucleus interactions, the

real answer we seek to obtain is the solution to the many-electron Schrödinger equation given as

$$\mathscr{H}_N\psi_N = \sum_{i=1}^{N}\left[-\frac{\hbar^2}{2m}\vec{\nabla}_i^2 + V_i^{e\text{-}n} + \sum_{j\neq i}^{N-1} V_{ij}^{e\text{-}e}\right]\psi_N = E\psi_N \ , \tag{2.8}$$

where $\mathscr{H}_N$ is the N-electron Hamiltonian and $\psi_N = \psi_N\left(\{\vec{r}_i, s_i\}\right)$ is the N-electron wave function with $\vec{r}_i$ and s_i being the position and spin of the ith-electron. The ith-electron – nucleus interaction potential $V_i^{e\text{-}n}$ is given by [2]

$$V_i^{e\text{-}n} = \sum_{\ell}\frac{-Ze^2}{|\vec{r}_i - \vec{R}_\ell|} \ , \tag{2.9}$$

and the ith-electron – jth-electron interaction potential $V_{ij}^{e\text{-}e}$ is given by

$$V_{ij}^{e\text{-}e} = \frac{1}{2}\frac{e^2}{|\vec{r}_i - \vec{r}_j|} \ . \tag{2.10}$$

The kinetic energy for nuclei can be safely ignored in accord with the Born–Oppenheimer approximation, for the nuclei are much heavier than the electrons [26]. As a result, the nucleus – nucleus interactions term, $\sum_{\ell\neq m}\frac{Z^2e^2}{|\vec{R}_\ell - \vec{R}_m|}$, can also be treated as a constant addition to the Hamiltonian, since there exists no other nuclear degree of freedom left in the Hamiltonian. However, one still cannot treat such a huge problem even with the use of modern techniques, and it is obvious that we need some further simplifications. This is established by switching back to the one-electron problem. The one-electron – nucleus interaction can be written as

$$V_1^{e\text{-}n}(\vec{r}) = \sum_{\ell}\frac{-Ze^2}{|\vec{r} - \vec{R}_\ell|} \ , \tag{2.11}$$

where we did not do any approximation in fact. The approximate nature of the mean-field fashion comes with the electron – electron interaction part. We will treat the interaction of a single electron with the remaining $N-1$-electrons as the interaction of that single electron with an electron soup of charge density $\rho(\vec{r})$. Thus, we write the one-electron – other-electrons interaction as

[2] We can always choose a unit system with the vacuum permittivity $\epsilon_0 = \frac{1}{4\pi}$ in order to simplify the electrostatic potential, which will be the case throughout this thesis.

$$V_1^{e\text{-}e}(\vec{r}) = \int d\vec{r}\,' \frac{-e\rho(\vec{r})}{|\vec{r}-\vec{r}\,'|} \ . \tag{2.12}$$

But the electron charge density is in fact given by

$$\rho(\vec{r}) = -e\sum_j |\psi_j(\vec{r})|^2 \ . \tag{2.13}$$

This simplificaltion together with the single-electron – nucleus interaction yields to the set of Schrödinger equations

$$\left[-\frac{\hbar^2}{2m}\vec{\nabla}^2 + \sum_\ell \frac{-Ze^2}{|\vec{r}-\vec{R}_\ell|} + \sum_j \int d\vec{r}\,' \frac{e^2|\psi_j(\vec{r}\,')|^2}{|\vec{r}-\vec{r}\,'|}\right]\psi_i(\vec{r}) = E_i\psi_i(\vec{r}) \ , \tag{2.14}$$

which is named as "*Hartree equations*" after the work of Hartree in 1928, and can be solved numerically via iterative methods [27].

The method can be further improved by the consideration of the fermionic antisymmetry and the Pauli exclusion principle, that is established by replacing the N-electron wave function ψ_N with a Slater determinant of the form [28]

$$\psi_N\left(\{\vec{r}_i, s_i\}\right) = \frac{1}{\sqrt{N!}}\begin{vmatrix} \psi_1(\vec{r}_1,s_1) & \psi_1(\vec{r}_2,s_2) & \cdots & \psi_1(\vec{r}_N,s_N) \\ \psi_2(\vec{r}_1,s_1) & \psi_2(\vec{r}_2,s_2) & \cdots & \psi_2(\vec{r}_N,s_N) \\ \vdots & \vdots & \ddots & \vdots \\ \psi_N(\vec{r}_1,s_1) & \psi_N(\vec{r}_2,s_2) & \cdots & \psi_N(\vec{r}_N,s_N) \end{vmatrix} \ . \tag{2.15}$$

This procedure yields to the addition of an exchange term to the left-hand-side of the Hartree equation, Eq.(2.14). This exchange term resulting from the repulsion of electrons with parallel spins is given by

$$V_1^X(\vec{r}) = \sum_j \int d\vec{r}\,' \frac{-e^2}{|\vec{r}-\vec{r}\,'|}\psi_j^*(\vec{r}\,')\psi_i(\vec{r}\,')\psi_j(\vec{r})\delta_{s_i s_j} \ , \tag{2.16}$$

and with this improvement of Fock in 1930, the method is known as Hartree–Fock theory [29].

2.1.6 Density functional theory

Developed by Hohenberg, Kohn, and Sham in 1964 [30, 31], the "*density functional theory*" (or "*DFT*") can be seen as the successor of the Hartree–Fock theory.

Basically, the exchange term $V_1^X(\vec{r})$ in Hartree–Fock theory given by Eq.(2.16) is replaced by an exchange correlation term $V_1^{XC}[n(\vec{r})]$ that is a functional derivative of the exchange correlation energy $E^{XC}[n(\vec{r})]$, which is a functional of the electron number density $n(\vec{r})$. The dynamic correlation effect results from the Coulomb repulsion between electrons with antiparallel spins and is ignored in the Hartree-Fock theory. The other difference between the two methods is that, in density functional theory, the wave functions which form the Slater determinant are not necessarily the single electron wave functions, but they can assume any functional form that are used to obtain the electron density.

One can obtain the exchange correlation potential approximately by beginning with the exchange correlation energy of a homogeneous electron gas, that is known as the "*local density approximation*" or "*LDA*". If the spin degrees of freedom are also considered the local-density approximation is improved to a method known as "*local spin density approximation*" or "*LSDA*".

2.1.7 Epilogue

The models and techniques mentioned in this section provide a brief introduction for the quest of metallic behavior, while detailed analyses, derivations, and conclusions are ommited. The aforementioned subjects along with basic solid state concepts (like Bravais lattices, *etc.*) and many other techniques to calculate the electronic structure of metals, *e.g.*, orthogonalized plane wave method, pseudopotential method, augmented plane wave method, Korringa–Kohn–Rostoker (Green's function) method, linear-muffin-tin orbital (LMTO) method, linear response theory, Car–Parinello method, cellular method, *etc.*, can be found in advanced level textbooks [32, 33, 34, 35, 36, 37, 38, 39, 40] and encyclopedic references on condensed matter physics [41, 42].

The methods mentioned in this section all depend on the independent-electron approximation that is established on the conversion of the N-electron Schrödinger equation into a one-electron problem. In the tight-binding approximation, the atomic orbital wave functions are linearly superposed to obtain the crystal orbital wave functions. In the Hartree–Fock approximation and the density functional

theory, the many-electron effects are integrated into the one-electron potential in order to obtain an effective Hamiltonian. However, the independent-electron approximations become inadequate when the problem in consideration involves strong correlations between electrons. In the next section we will see that it is in fact the strongly correlated electrons that give rise to exceptional phenomena in some metallic materials.

2.2 Electron correlations and the exchange mechanisms

2.2.1 Prologue

The methods described in the previous section rely on the independent-electron approximation. However, in the study of condensed matter systems we actually work with many-electrons, while the word "*many*" here, means a number, N, that is far much larger than any other number that we can find in our physical world to study. More precisely, N is in the order of 10^{23}, that is the order of the Avogadro's number. Well, you can insist on the idea of studying with smaller pieces of materials of the size of a cube milimeter instead of a cube centimeter, and claim that $N \sim 10^{20}$, however, let us recall that this number is the order of the age of the universe in *miliseconds* according to ΛCDM concordance model and recent *WMAP* data [43]. Thus, we can rightfully justify that we work in the limit $N \to \infty$. In fact, this limit, among with a fixed density, describes the so called "*thermodynamic limit*":

$$\begin{aligned} N &\to \infty \,, \\ V &\to \infty \,, \\ \frac{N}{V} &= \text{constant} \,, \end{aligned} \tag{2.17}$$

where V denotes the volume of the system under study.

This is an essential point in condensed matter physics. It gives rise to one of the most awesome physical phenomena, namely "*phase transitions*". Phase transitions are characterized by abrupt changes in the physical properties of matter at specific temperatures or external fields. In a "*first-order phase transition*", densities, that are the first derivatives of the free-energy with respect to thermodynamic fields, show singularities, *e.g.*, discontinuities, while a "*second-order phase transition*" is characterized by nonanalytic behavior, *e.g.*, asymptotic divergence, in response functions, that are the derivatives of densities. It is known that phase transitions among with some other phenomena occur only in the thermodynamic limit.

Thus, we must be losing some physical reality once we assume the independent-electron approximation. What we miss actually is the correlations between electrons. "*Correlation*" has a specific meaning in statistics, *i.e.*, for two correlated

random variables, p and q,

$$\langle pq \rangle \neq \langle p \rangle \langle q \rangle \ , \tag{2.18}$$

where $\langle \cdot \rangle$ denote averaging. The correlation function between p and q, defined as

$$\Gamma(p,q) \equiv \langle (p - \langle p \rangle)(q - \langle q \rangle) \rangle = \langle pq \rangle - \langle p \rangle \langle q \rangle \ , \tag{2.19}$$

vanishes if p and q are uncorrelated, but assumes a finite value if p and q are correlated. Thus, a correlation between p and q mathematically means whenever p deviates from its average value $\langle p \rangle$, q also deviates from its average value $\langle q \rangle$, so that the average of the multiplication of the deviations do not vanish.

In the independent-electron approximation, the correlations between the electron wave functions are neglected. We assume that the crystal orbital wave function that describes the material can be written as the linear combination of atomic orbital wave functions in the tight-binding approximation. In the mean-field approximations of Hartree–Fock and density functional theories, we assume that the Coulombic electron-electron correlations can be written as an effective one-electron potential, namely as the interaction of a single electron with the averaged charge density of the remaining electrons. In turn, in self-consistent field type approximations, the wave function can be factorazible in single-electron wave functions, which contradicts with Eq.(2.18) if the electrons are correlated.

Most of the remarkable phenomena that arise for lantinates and actinides (collectively referred as "*heavy-fermions*"), transition metals, and the compounds and alloys of these elements are due to strong correlations between electrons. Among these are magnetism, superconductivity, mixed valence, Wigner crystallization, charge ordering, spin ordering, fractional quantum Hall effect, colossal magnetoresistance, and the metal-insulator transition [37, 44].

2.2.2 Two-electron interactions

Although phase transitions and spontaneous ordering emerge in the thermodynamic limit, the effects of electron-electron interactions become evident even in

the two-electron problem. Let us start by defining the hydrogen atom problem, that can be solved exactly and taught at undergraduate level.

2.2.2.1 Hydrogen atom

The hydrogen Hamiltonian for the single electron in the electric field of a single proton is given by

$$\mathscr{H}_H = -\frac{\hbar^2}{2m}\vec{\nabla}^2 - \frac{e^2}{r} \ , \tag{2.20}$$

and have the eigenfunction solutions labeled by three quantum numbers n, l, m as $\psi_{nlm}(\vec{r}) = R_{nl}(r)Y_l^m(\theta,\varphi)$. The eigenenergy solutions depend only on n and given as $E_n = -\frac{e^2}{2a_0n^2}$, where $a_0 = \frac{\hbar^2}{2me} \approx 0.529$ Å is the Bohr radius. The lowest lying state is the $1s$ state of ψ_{100} with energy $E_{1s} \approx -13.6$ eV. The spin state of the electron has no relevance in the hydrogen atom problem, for the spin-up and spin-down states are degenerate. For further details, one may refer to any elementary textbook on quantum mechanics.

2.2.2.2 Hydrogen molecule and the exchange interactions

Adding one more hydrogen atom to the above mentioned hydrogen problem brings in new phenomena. Essentially, the states with diferent total spin are split and this is caused by the electron-electron interaction. The most crucial effects are the so called "*direct exchange*" and "*kinetic exchange*" interactions. There also exist the indirect exchange and the superexchange that we will not mention here, but one can refer to [32, 40] for details on these mechanisms.

The H_2 hydrogen molecule Hamiltonian can be written as

$$\mathscr{H}_{H_2} = \sum_{i=1}^{2}\left[-\frac{\hbar^2}{2m}\vec{\nabla}_i^2 - \frac{e^2}{|\vec{r}_i - \vec{R}_1|} - \frac{e^2}{|\vec{r}_i - \vec{R}_2|}\right] + \frac{e^2}{|\vec{r}_1 - \vec{r}_2|} + \frac{e^2}{|\vec{R}_1 - \vec{R}_2|} \ , \tag{2.21}$$

where $\vec{r}_i$ and $\vec{R}_j$ are the positions of ith electron and jth proton respectively. Here in the sum, the first term is the electron kinetic energy term, while the other two terms are electron-proton interaction terms. The last two terms are succesively the electron-electron and proton-proton interaction terms. We assume that the

protons are stationary due to the Born–Oppenheimer approximation, and thus, treat the last proton-proton term in Eq.(2.21) as a constant [26]. The low lying states of such a system is a 6-dimensional Hilbert space that has the basis set given by the $1s$ atomic orbitals, for exciting the electrons above the $1s$ state costs a relatively large energy.[3] This basis set is given by

$$\{|\uparrow\uparrow\rangle, |\uparrow\downarrow\rangle, |\downarrow\uparrow\rangle, |\downarrow\downarrow\rangle, |\Updownarrow\bigcirc\rangle, |\bigcirc\Updownarrow\rangle\} \ , \tag{2.22}$$

where the first and second symbols refer to the electrons localized on the first and the second proton. The single arrows denote the spin states of the singly localized electrons, while a double arrow and a circle are for an H^- and an H^+ ion respectively. Thus, we name the first four states as neutral and the last two as ionized. Since there exist Coulomb repulsion between electrons, we note that the ionized states have higher energy levels than the neutral states, for in the ionized states both electrons are on the same proton site. Again, recall that each of the electrons in the above set is in the $1s$ atomic orbital.

2.2.2.2.1 Direct exchange

Now, working in the neutral states subspace, that is called the "*Heitler-London approximation*" [45], let us denote the $1s$ atomic orbital wave function of the ith electron localized on the jth proton by $\phi_j(\vec{r}_i)$, and the spin wave function of the ith electron by $\chi_{\uparrow i}$ and $\chi_{\downarrow i}$. Since the total wave function of the system must be antisymmetric under the exchange of electrons due to Pauli exclusion principle, the allowed states that we can construct with the neutral states are

[3] The first excitation to $2s$ state costs approximately 10.2 eV, which is approximately 398 k_BT at 298 K room temperature.

$$\begin{aligned}
\psi_1 &= \frac{1}{\sqrt{2(1-I^2)}}\Big[\phi_1(\vec{r}_1)\phi_2(\vec{r}_2)-\phi_2(\vec{r}_1)\phi_1(\vec{r}_2)\Big]\chi_{\uparrow 1}\chi_{\uparrow 2}\ , \\
\psi_2 &= \frac{1}{\sqrt{4(1-I^2)}}\Big[\phi_1(\vec{r}_1)\phi_2(\vec{r}_2)-\phi_2(\vec{r}_1)\phi_1(\vec{r}_2)\Big]\Big[\chi_{\uparrow 1}\chi_{\downarrow 2}+\chi_{\downarrow 1}\chi_{\uparrow 2}\Big]\ , \\
\psi_3 &= \frac{1}{\sqrt{2(1-I^2)}}\Big[\phi_1(\vec{r}_1)\phi_2(\vec{r}_2)-\phi_2(\vec{r}_1)\phi_1(\vec{r}_2)\Big]\chi_{\downarrow 1}\chi_{\downarrow 2}\ , \\
\psi_4 &= \frac{1}{\sqrt{4(1-I^2)}}\Big[\phi_1(\vec{r}_1)\phi_2(\vec{r}_2)+\phi_2(\vec{r}_1)\phi_1(\vec{r}_2)\Big]\Big[\chi_{\uparrow 1}\chi_{\downarrow 2}-\chi_{\downarrow 1}\chi_{\uparrow 2}\Big]\ , \qquad (2.23)
\end{aligned}$$

where the first three states are the total spin-1 triplet states with S^z-eigenvalues of 1, 0, and -1, while the last state is the total spin-0 $S^z = 0$ singlet state. With the overlap integral defined as

$$I \equiv \int d\vec{r}_i\ \phi_1^*(\vec{r}_i)\phi_2(\vec{r}_i)\ , \qquad (2.24)$$

these four states are all eigenstates of the H_2 Hamiltonian with energy eigenvalues

$$\begin{aligned}
E_1 = E_2 = E_3 = 2E_{1s} + \frac{C-X}{1-I^2} &\equiv E_t\ , \\
E_4 = 2E_{1s} + \frac{C+X}{1+I^2} &\equiv E_s\ , \qquad (2.25)
\end{aligned}$$

where C and X are Coulomb and exchange integrals respectively, given by [44]

$$\begin{aligned}
C \equiv & \int d\vec{r}_1 \int d\vec{r}_2\ |\phi_1(\vec{r}_1)|^2 \frac{e^2}{|\vec{r}_1-\vec{r}_2|}|\phi_2(\vec{r}_2)|^2 \\
& - \int d\vec{r}_1\ |\phi_1(\vec{r}_1)|^2 \frac{e^2}{|\vec{r}_1-\vec{R}_2|} - \int d\vec{r}_2\ |\phi_2(\vec{r}_2)|^2 \frac{e^2}{|\vec{r}_2-\vec{R}_1|}\ , \\
X \equiv & \int d\vec{r}_1 \int d\vec{r}_2\ \phi_1^*(\vec{r}_1)\phi_2^*(\vec{r}_2)\frac{e^2}{|\vec{r}_1-\vec{r}_2|}\phi_2(\vec{r}_1)\phi_1(\vec{r}_2) \\
& - I\int d\vec{r}_1\ \phi_1^*(\vec{r}_1)\frac{e^2}{|\vec{r}_1-\vec{R}_2|}\phi_2^*(\vec{r}_1) - I\int d\vec{r}_2\ \phi_2^*(\vec{r}_2)\frac{e^2}{|\vec{r}_2-\vec{R}_1|}\phi_1^*(\vec{r}_2). \qquad (2.26)
\end{aligned}$$

Accordingly, the singlet-triplet splitting can be calculated as

$$J \equiv E_t - E_s = 2\frac{I^2C - X}{1-I^4}\ . \qquad (2.27)$$

Within the neutral wave functions subspace, using the splitting above, we can relate the Hamiltonian operator with spin operators, noting that the act of the

operator $(\vec{S}_1 + \vec{S}_2)^2$ will yield eigenvalues of 2 and 0 for triplet and singlet states respectively. In a more convenient way, we choose the operator $2\vec{S}_1 \cdot \vec{S}_2 + \frac{1}{2}$, which equals $(\vec{S}_1 + \vec{S}_2)^2 - 1$, and have eigenvalues of $+1$ for a triplet and -1 for a singlet state. Thus, we can conclude that

$$\mathscr{H} = \frac{E_t + E_s}{2} - \frac{E_t - E_s}{2}\left(2\vec{S}_1 \cdot \vec{S}_2 + \frac{1}{2}\right) = J\vec{S}_1 \cdot \vec{S}_2 + constant\ . \tag{2.28}$$

Here, J is named as "*exchange coupling*" and serves as a spin-spin interaction potential. However, one should note that it is purely an effect of Coulomb interaction between electrons and the Pauli exclusion principle, and there is no primary interaction between spins actually.

Hence, we obtained the principle form of what is called "*exchange Hamiltonians*". It was Heisenberg and Dirac who first recognized the exchange mechanism in 1926 [46, 47] and the Hamiltonian

$$\mathscr{H} = \sum_{ij}\left[J_{ij}\vec{S}_i \cdot \vec{S}_j\right] \tag{2.29}$$

is called Heisenberg-Dirac Hamiltonian. In principle, three-body (and higher order) Coulomb interactions also result in exchange mechanisms, however they involve much more complicated derivations from the first-principles, and yet in condensed matter studies the two-body form of the Hamiltonian above is capable of capturing the essential magnetic phenomenon, since we already have a parameter (J) to fit with the experimental results. Even the nearest-neighbor Heisenberg model gives a phase transition from a paramagnet to an (anti)ferromagnet at a critical (Néel) Curie temperature. The sign of the exchange coupling, J, defined in Eq.(2.27) determines whether the material is antiferromagnetic ($J > 0$) or ferromagnetic ($J < 0$) below the critical temperature. The exchange coupling changes sign at $I = \sqrt{\frac{X}{C}}$, with $0 < I < \sqrt{\frac{X}{C}}$ corresponding to the ferromagnetic case and $\sqrt{\frac{X}{C}} < I < 1$ to the antiferromagnetic case.

The Heitler–London approximation for the H_2 molecule exchange coupling, as derived above, have certain inadequacies for large and small interatomic distances. For the large interatomic distances, the overlap integral, I, tends to vanish and the

exchange coupling becomes strongly ferromagnetic, however, it is known that the H_2 molecule has a singlet, thus antiferromagnetic, ground state for all interatomic distances [44]. The result can be improved by taking the higher lying states into account, that in turn, leads to more complicated derivations. Hence, we see that calculating the exchange effects is highly nontrivial even for the simplest systems. This also illustrates the inadequacy of the density functinal theory, that relies on calculating a general form of exchange couplings.

2.2.2.2.2 Kinetic exchange

For the small interatomic distances of H_2, the problem with the Heitler–London scheme can be lifted simply by considering the previously neglected ionized states, namely $|\,\Updownarrow\,\bigcirc\rangle$ and $|\bigcirc\,\Updownarrow\rangle$. Hence, we define

$$\begin{aligned}\psi_{\Updownarrow\bigcirc} &\equiv \frac{1}{\sqrt{2}}\phi_1(\vec{r}_1)\phi_1(\vec{r}_2)\Big[\chi_{\uparrow 1}\chi_{\downarrow 2}-\chi_{\downarrow 1}\chi_{\uparrow 2}\Big]\ ,\\ \psi_{\bigcirc\Updownarrow} &\equiv \frac{1}{\sqrt{2}}\phi_2(\vec{r}_1)\phi_2(\vec{r}_2)\Big[\chi_{\uparrow 1}\chi_{\downarrow 2}-\chi_{\downarrow 1}\chi_{\uparrow 2}\Big]\ .\end{aligned} \tag{2.30}$$

But now, in the Hamiltonian, we have an on-site Coulomb integral that can be expressed as

$$U \equiv \int d\vec{r}_1 \int d\vec{r}_2\ |\phi_i(\vec{r}_1)|^2 \frac{e^2}{|\vec{r}_1-\vec{r}_2|}|\phi_i(\vec{r}_2)|^2\ , \tag{2.31}$$

which is larger than the Coulomb integral, C, given in Eq.(2.26), since the electrons both share the same $1s$ atomic orbital now. The interaction U is named as "*on-site Coulomb repulsion*" or as "*Hubbard U*" for the reasons that will become clear in the further sections. Having both electrons on the same atomic site costs us a Coulombic energy of U, however, since we lifted the restriction of localization on separate sites, that will contribute as a kinetic energy gain in return. The "*tight-binding hopping integral*", that mixes the ionized and neutral states, is given by

$$-t \equiv -\int d\vec{r}_i\ \phi_1^*(\vec{r}_i)\frac{e^2}{|\vec{r}_i-\vec{R}_j|}\phi_2(\vec{r}_i)\ , \tag{2.32}$$

and serves as the kinetic energy associated with the nearest-neighbor single-electron hopping processes of $|\uparrow\downarrow\rangle \rightleftharpoons |\,\Updownarrow\,\bigcirc\rangle$, $|\uparrow\downarrow\rangle \rightleftharpoons |\bigcirc\,\Updownarrow\rangle$, $|\downarrow\uparrow\rangle \rightleftharpoons |\,\Updownarrow\,\bigcirc\rangle$, and

$|\downarrow\uparrow\rangle \rightleftharpoons |\bigcirc\, \Updownarrow\rangle$. Note that the triplet ferromagnetic states with $|\uparrow\uparrow\rangle$ and $|\downarrow\downarrow\rangle$ are not affected by the consideration of the ionized states, since no two electrons can occupy the same quantum level due to Pauli exclusion principle. Furthermore, the triplet state ψ_2 also does not mix with the doubly occupied states due to symmetry. As a result, the mixture of the ionized states extend the triplet-singlet splitting approximately (assuming $C \ll U$ and $X \ll U$) by an additional amount of $J_{kinetic} \approx 4t^2/U$, and further stabilizes the antiferromagnetic state. This energy shift in the order of $\mathcal{O}(t^2/U)$ in favor of antiferromagnetism can also be found by second order perturbation theory in the *atomic limit* of $t/U \to 0$ [48, 49, 50, 51, 52, 53, 54, 55, 56, 57, 58].

This additional exchange interaction associated with the hopping of electrons between nearest-neighboring sites is called "*kinetic exchange*", and is again purely an effect of electron correlations and the fermionic nature of electrons.

2.2.3 Epilogue

In the following sections, we will make use of the tight-binding hopping integral, t, and the on-site Coulomb repulsion, U, in order to construct a model Hamiltonian in the tight-binding scheme for the theoretical investigation of the phenomena that were mentioned briefly in the beginning of this section and some of which will be reviewed in more detail in experimental aspects through the next section.

2.3 Mott–Hubbard transition

2.3.1 Prologue

As we stated above, the independent-electron approximation fails to predict some electron correlation effects, and in this section we will emphasize on these electron correlation effects both from experimental and theoretical points of view succesively. In condensed matter physics, we are interested in the crystaline systems mostly; and in this thesis, we omit the consideration of noncrystaline systems entirely. That is why the "independent-electron approximation" is synonymous to the "band theory of solids" for our investigation[4]. Besides, what we mean by the term "*electron correlation effects*" is the phenomena that cannot be predicted by the simple band theory.

The early achievement of the band theory was that, it classified almost all solid materials as metals or insulators, which was right after its introduction. However, it was also for the same type of materials, that the theory lacked the true prediction. That is to say, the band theory of solids erroneously predicted a metallic behavior for a class of insulators. Later on, more types of wrong prediction were discovered. Categorically, for these materials, the electron correlations are strong, and the misleading due to band theoretical approach is caused by the ignorance of the effects of strong electron correlations. Thus, we name this class of materials as "*strongly correlated electron systems*".

2.3.2 Strongly correlated electron systems

Typical examples of strongly correlated electron systems contain compounds of heavy-fermion systems (rare earth metals and actinides), *e.g.*, $CeCu_2Si_2$, UBe_{13}, UPt_3, $NpBe_{13}$, U_2Zn_{17}, UCd_{11}, $NpSn_3$, $CeAl_3$, YbCuAl, *etc.*, and compounds of transition metal elements (usually oxides), *e.g.*, Ni, La_2CuO_4, V_2O_3, NiS_2Se, $BaVS_3$, Fe_3O_4, FeSi, Ti_2O_3, $LaCoO_3$, *etc.* [59, 60]. These materials share a common chemical property, that is the partially filled d- and/or f-shells. The correlations between d- or f-electrons are particularly strong, for the atomic orbital wave func-

[4]This approach is also commonly referred as "*Bloch–Wilson band theory*".

tions of these electrons do not extend from the nuclei as far as the atomic orbitals of s- and p-electrons do, and in turn, d- and f-electrons feel much higher Coulomb repulsion on average.

The s- and p-orbitals can be considered as Bloch functions in most cases. However, for systems with small hopping- and overlap-integrals between nearest-neighboring atoms (narrow-band systems), the d- and f-orbitals must be described by localized Wannier states. The localization of these electrons extend due to spatial contraction of the d- and f-atomic orbitals. Moreover, for heavy-fermion systems, the s- and p-orbital contractions must also be considered, since a heavier nucleus creates increased Coulomb attraction. Direct relativistic effects also imply the contraction of s- and p-orbitals. This, in turn, creates a shielding for the d- and f-shells, and extends their localization [40].

The above argument is supported with another point of view [61]: The hopping integrals for Wannier localized wave functions determine the quantum mechanical average kinetic energy of the electrons, and in turn, the band width, W, of the electronic structure. The mean time, τ, spent by an electron on an atomic orbital can be related to the band width by a mere application of Heisenberg energy-time uncertainty principle [62], namely $\Delta E \Delta t \gtrsim \hbar$, where the uncertainties in energy, ΔE, and time, Δt, can be taken as W and τ respectively, yielding the inverse proportionality between τ and W,

$$\tau \sim \frac{\hbar}{W} \ . \tag{2.33}$$

Thus, for narrow-band systems of partially filled d- or f- orbitals, the smaller value of W yields a larger τ, and hence, electrons spending more time on the same atomic orbital. As a direct consequence of a large τ, the Coulomb intearction between d- and/or f-electrons on the same atomic site become significantly weighted, and the system turn out to show a strongly correlated electron behavior.

One cannot expect to describe such systems by neglecting these strong correlations between d- and/or f-electrons, and that is why the mean-field type approximations (Hartree–Fock and density functional theories) fail to predict the physical properties of the real experimental strongly correlated electron systems.

2.3.3 Experimental systems

2.3.3.1 Metals versus insulators

What is the experimental description of a metal and an insulator? How can one measure the metallic behavior? The essential physical observable is the (DC electrical) resistivity, ρ, measured in Ohm meter (Ω·m) in SI units and defined by[5]

$$\rho \equiv \frac{|\vec{E}|}{|\vec{J}|} \ , \tag{2.34}$$

where $\vec{E}$ and $\vec{J}$ are the electric field and the current density vectors respectively. A better serving measure is the reciprocal of the resistivity, namely conductivity, given by

$$\sigma \equiv \frac{1}{\rho} \ , \tag{2.35}$$

measured in Siemens per meter (S·m^{-1}) in SI units. We should note that, it is not the conductivity itself that determines the metallic nature of a material, but it is the rate of change in conductivity with respect to temperature.

For an insulator there is a finite gap between the valence and the conduction bands, and since electrons can be excited into the conduction band by thermal excitation, the conductivity of an insulator can be increased by raising the temperature. This is reflected as a positive derivative of conductivity with respect to temperature, and hence, $\frac{d\sigma}{dT} > 0$ for insulators. On the contrary, in metals, as the temperature is raised, the electron scattering mechanisms cause a decrease in conductivity, that can be expressed as $\frac{d\sigma}{dT} < 0$ for metals.

According to independent-electron approximation of band theoretical treatment, for an insulator, the gap between the valence and the conduction band asserts an even number of electrons per unit cell, since in order to obtain a completely filled valence band, one needs to fill each quantum mechanical energy level by two electrons with spins up and down. Note that the opposite reasoning may not work, *i.e.*, an even number of electrons per unit cell does not necessarily imply

[5] Anisotropy effects, which can be included by the consideration of a resistivity tensor, are omitted.

a completely filled valence band, but may also lead to a partially filled conduction band with an even number of electrons in it. However, one can still categorize any material with an odd number of electrons per unit cell as a metal according to band theory, since the unpaired electron must yield to a partially filled band.

2.3.3.2 Mott–Hubbard insulators

A decade after the introduction of the band theory, de Boer and Verwey were the first to draw attention to a number of transition metal oxides, *e.g.*, NiO, ZnO, Cu_2O, Mn_3O_4, Fe_2O_3, *etc.*, that were expected to show metallic behavior according to band theory, being in fact very poor conductors [63]. Yet for some materials, *e.g.*, CoO, the expected metallic behavior, on the very contrary, reveals extreme insulator case at ambient conditions. As we discussed in the previous subsection, strong correlation effects must be on stage, for these compounds all possess partially filled d-shell electron bands. Mott and Peierls, in the same year, were the first to indicate the significance of the neglected electron correlations [64].

Let us discuss a historical example of the kind discussed above, *i.e.*, the transition metal monoxide CoO. This material has a slightly distorted rock salt (NaCl) structure that has one Co and one O per unit cell (*cf.* Fig. 2.3 below). The transition metal, cobalt, has the electron configuration $[Ar]4s^2 3d^7$, while oxygen manifests $[He]2s^2 2p^4$ configuration. The already paired electrons of the inner shells

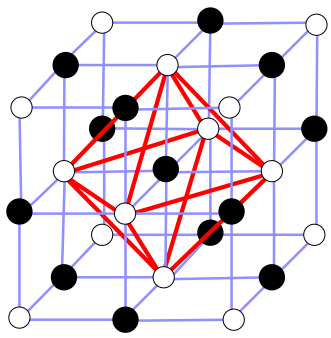

Figure 2.3: The rock salt structure of CoO with black and white spheres denoting Co and O occupation. The unit cell, which contains one of each Co and O atoms, is given with the red octahedron.

may be omitted, and thus, the total number of electrons on the outer shells of the atoms in a unit cell, being $9+6 = 15$, is an odd number, which yields a metallic behavior within the band theoretical approach. However, this prediction contradicts with experiments, since CoO is one of the most robust insulators [37, 44, 65, 66].

The band theory prediction mentioned above may be improved by consideration of different orbitals for different spins, which will eventually yield an antiferromagnetic insulating ground state as was the case with the H_2 molecule that we mentioned before. But this consideration will give a phase transition at a critical temperature from the antiferromagnetic insulating phase to a paramagnetic metallic phase, which also contradicts with experiments, since CoO in the paramagnetic phase is still a strong insulator [44]. The insulators of the kind we described here are called "*Mott–Hubbard insulators*", after Mott's and Hubbard's introductions of theoretical explanations for the metal-insulator transition in such strongly correlated systems.

The condensed matter community treated the Mott–Hubbard insulators as a marginal subject for a long period. However, among with other significant phenomena, the discovery of high-T_c superconductor cuprates in 1986 [67] and the rediscovery of colossal magnetoresistant manganites in early 1990s [68, 69] provoked the attention on Mott–Hubbard insulators once again, for these exceptional compounds were nothing but doped Mott–Hubard insulators [37]. Since then, the phase transitions between the metallic and the Mott–Hubbard insulating phases became a central problem for many condensed matter physicists. Next, we will discuss the nature of this metal-insulator transition, also named as "*Mott–Hubbard transition*".

2.3.3.3 The Mott–Hubbard transition

The band theoretical approach faced a more significant failure when the Mott–Hubbard transition was discovered. The metallic behavior predicted by the band theory is insensitive to a change either in temperature or in lattice spacing, *i.e.*, the material is a metal if it has an odd number of electrons per unit cell, regardless of how large the lattice spacing is, for the correlations between atomic orbitals are neglected. However, even a simple *Gedanken* experiment may reveal the inconsis-

tency: As one increases the interatomic distance, the hopping-integral vanishes, that is to say, electrons need more kinetic energy in order to become delocalized from the atomic orbitals. And yet, in the large interatomic distance limit, it is plausible to regard all electrons localized on single atoms, thus, the system turns out to be an array of individual isolated atoms that do not interact with each other, and the material becomes an insulator.

One of the most crucial experimental examples of such a transition is seen in pure and doped vanadium sesquioxide, V_2O_3 [70], which led condensed matter physicists to appreciate the strong correlation effects. V_2O_3 still serves as a benchmark material for the test of new theories. As can be observed from Fig. 2.4 below, the pure V_2O_3 is an insulator with $\frac{d\sigma}{dT} > 0$ in the low temperature regime. Density functional theory with basic local density approximation, however, predicts a metallic state for V_2O_3 [71]. What is more crucial in Fig. 2.4 is that, upon increasing the temperature, the resistivity experiences a seminal drop of approximately six orders of magnitude and the material undergoes a metal-insulator transition at around a temperature of 150 K. This is a typical example of a Mott–Hubbard metal-insulator transition.

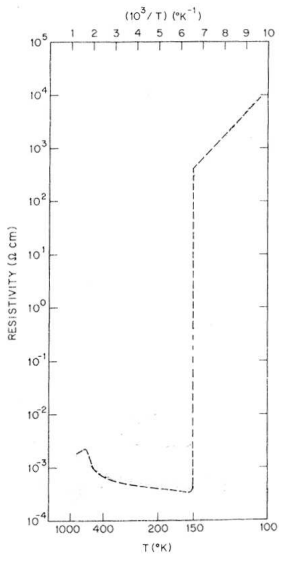

Figure 2.4: The temperature dependence of the resistivity (in the direction perpendicular to the c-axis of the lattice) of pure V_2O_3. Note the huge jump of approximately six orders of magnitude in the vicinity of 150 K (after [70]).

Before we begin to discuss the theoretical details of this phase transition, let us also present the pressure-temperature phase diagram for doped V_2O_3, given in Fig. 2.5 below. The internal pressure of the material V_2O_3 can be tuned precisely by doping Ti or Cr atoms that substitute the V atoms in the crystal. The decrease in pressure implies a phase transition from the high-temperature paramagnetic metallic phase into a high-temperature low-pressure insulating phase. This insulating phase is, however, different from the low-temperature insulating phase, which is accompanied by an antiferromagnetic long-range order, while the low-pressure high-temperature insulating phase is paramagnetic. The first-order phase transition between the metallic phase and the paramagnetic insulating phase terminates at a critical point at around $T_c \approx 400$ K, and one can smoothly pass from the metallic to the insulating phase above this T_c. We also note that the antiferromagnetic low-temperature insulator is fairly robust and insensitive to pressure, and the long-range antiferromagnetic order is only destroyed at high values of pressure.

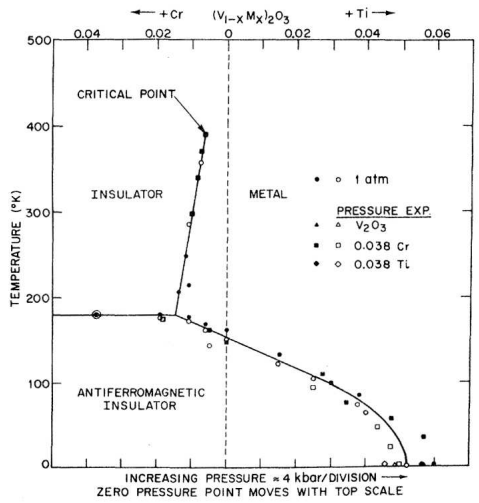

Figure 2.5: The experimental pressure-temperature phase diagram for the doped V_2O_3 (after [70]). The V atoms are substituted by either Ti or Cr atoms by controlled doping, which in turn, tunes the internal pressure. The jump in Fig. 2.4 for the pure case corresponds to the phase transition along the dashed line of $x = 0$.

Now, having seen how the pure band theoretical approach fails to explain the physical nature of experimental systems for which the electron correlation effects are strong, we need a better theoretical treatment of such systems. Mott and Hubbard introduced the required theoretical tools, and the next subsections are devoted to the understanding of these approaches to the strongly correlated electron systems.

2.3.4 Mott–Hubbard theory

When de Boer and Verwey presented their strange experimental results, namely the NiO being an insulator, at a conference in 1937, it was Peierls who, for the first time, pointed out the significance of the correlation effects during the discussion session [64, 72]. Later, in 1949, Mott provided a more detailed picture of the metal-insulator transition in concern [72, 73, 74, 75, 76]. Today, the theoretical understanding of the Mott–Hubbard transition, induced by strong electron correlations, is based on the Hubbard model, which was introduced in 1963 by Hubbard [77, 78, 79]. Before discussing the celebrated Mott–Hubbard theory in further detail, we should digress into the subject of screening.

2.3.4.1 Screened Coulomb interaction

The Coulomb attraction between a valence electron and its ion for the isolated atomic case is given by

$$V(r) = -\frac{Ze^2}{r} \ . \tag{2.36}$$

Here, r is the radial distance between the electron and the ion core, which includes Z protons inside. As opposed to the isolated atomic case, in a crystal enviroment, since the ion will also attract other freely moving delocalized conduction electrons, the Coulomb interaction between the electron and its ion will be largely screened by these free electrons. Bohm and Pines figured out that the form of the screened potential can be expressed as [80, 81, 82]

$$V(r) = -\frac{Ze^2}{r}\mathrm{e}^{-r/\lambda} \ , \tag{2.37}$$

where $-\frac{Ze^2}{r}$ is the bare Coulomb attraction for the isolated atomic case, while the constant λ in the exponential reflects the screening effect in the crystal enviroment, and called the "*screening radius*", whose value can be derived via Thomas–Fermi approximation [36, 72, 83].

The Fermi energy of a free electron is given by (see, *e.g.*, [32])

$$E_F = \frac{\hbar^2}{2m}\left(3\pi^2 n_f\right)^{2/3} \ , \tag{2.38}$$

where m is the electron mass and n_f is the free electron density in the absence of an ion within the free electron gas. Introducing an ion into this free electron gas changes the electron density around the ion of course, and the Poisson equation

$$\vec{\nabla}^2 V(r) = -4\pi e^2 \left[n(r) - n_f\right] \tag{2.39}$$

will define the electron density $n(r)$ around the ion that creates the Coulomb potential $V(r)$. The Fermi energy relation is also modified into

$$E_F + V(r) = \frac{\hbar^2}{2m}\left[3\pi^2 n(r)\right]^{2/3} \ , \tag{2.40}$$

from which the density can be obtained as

$$\begin{aligned} n(r) &= \frac{1}{3\pi^2}\left(\frac{2m}{\hbar^2}\right)^{3/2}\left[E_F + V(r)\right]^{3/2} \\ &= \frac{1}{3\pi^2}\left(\frac{2m}{\hbar^2}E_F\right)^{3/2}\left[1 + \frac{V(r)}{E_F}\right]^{3/2} \\ &= n_f\left[1 + \frac{V(r)}{E_F}\right]^{3/2} \ , \end{aligned} \tag{2.41}$$

where we used Eq.(2.38) in the last line. Since $V(r) \ll E_F$ [36], we can expand the term in the brackets in Taylor series and with a first order expansion we obtain

$$n(r) \approx n_f\left[1 + \frac{3}{2}\frac{V(r)}{E_F}\right] \ . \tag{2.42}$$

Substituting $n(r)$ in Eq.(2.39) with the expression given above in Eq.(2.42) yields

$$\vec{\nabla}^2 V(r) = \frac{1}{\lambda^2} V(r) \ , \tag{2.43}$$

where λ is defined as

$$\begin{aligned} \lambda &\equiv \sqrt{\frac{E_F}{6\pi e^2 n_f}} \\ &= \frac{\hbar}{2e}\left(\frac{\pi}{3m^3 n_f}\right)^{1/6} . \end{aligned} \tag{2.44}$$

by the use of Eq.(2.38). Now, Eq.(2.43) can be reduced to a second order ordinary differential equation in radial distance r as

$$\frac{1}{r^2}\frac{d}{dr}\left[r^2\frac{d}{dr}V(r)\right] = \frac{1}{\lambda^2}V(r) \ , \tag{2.45}$$

due to the spherical symmetry. One can assure that the screened Coulomb interaction given in Eq.(2.37) is an immediate solution to Eq.(2.45), and hence, the screening radius is given by Eq.(2.44).

In Fig. 2.6 below, we present a comparison between the bare and screened Coulomb interactions. The effect of screening can be easily observed as a fair

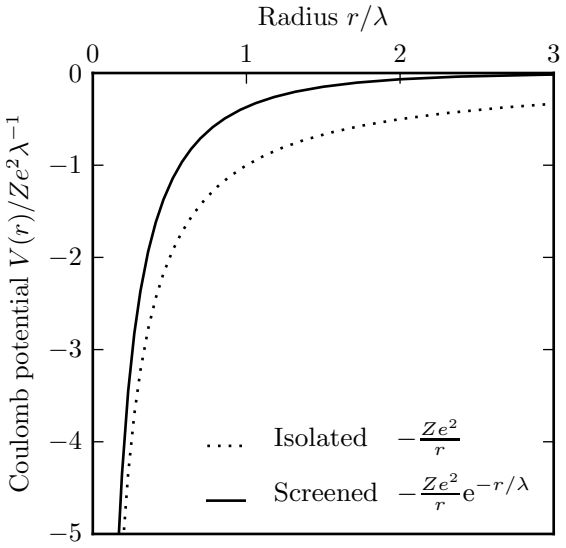

Figure 2.6: The bare Coulomb potential in the isolated atomic case (dotted curve) and the screened Coulomb potential in the crystalline case (full curve) for a localized electron. Radius and potential axes are scaled accordingly with λ and Ze^2/λ.

decrease in the electrostatic interaction between a localized electron and its ion core. We should also note that a typical value for the screening radius is in general well below the interatomic distance. For example, in the case of a Cu crystal, which has a lattice spacing $a \approx 0.255$ nm, Fermi energy $E_F \approx 7$ eV, and electron density $n_f \approx 8.5 \times 10^{28}$ m^{-3}, the screening radius is approximately $\lambda \approx 0.055$ nm, that is almost one-fifth of the interatomic spacing, and in fact, very close to the Bohr radius. The screening radius we derived here using the Thomas–Fermi approximation [83] is often named as "*Thomas–Fermi screening parameter*".

2.3.4.2 Mott theory of metal-insulator transition

Originally, Mott discussed a crystalline array of hydrogen-like monovalent atoms with lattice spacing a, that could be varied. For the small interatomic distances, like in the case of Na, the crystal will be a metal due to band theory, and it is obvious to the commonsense that in the large a limit, the crystal must be an insulator, since it will be reduced to an array of isolated atoms. This was actually the case for NiO, which is insulating according to the experiments of de Boer and Verwey. Thus, there must be a metal-insulator transition value a_{MIT} in between the two conducting behaviors.

This transition value can be obtained by considering the attractive screened Coulomb potential between the valence electron and the ion, separated by a radial distance r, given by Eq.(2.37). If the screened Coulomb potential is strong enough, the electrons will be trapped by ions. In this case, even if an electron leaps over this potential barrier, it will find no another atom nearby to hop, since there is also a strong Coulomb repulsion between the electrons on the same atomic site, and hence, the material will be in the insulating phase. However, the screened Coulomb potential can be tuned by changing the electron density n [*cf.* Eq.(2.44)], which is equivalent to varying the lattice spacing. Reducing the interatomic distance, a, leads to the increase in the electron density, n, that in turn, decreases the screening potential, λ, which in the end, reduces the screened Coulomb potential. We can assert that

$$n \sim a^{-3} \,, \tag{2.46}$$

since n is the number of electrons per unit volume. For the screening parameter, from Eq.(2.44), we can conclude that

$$\lambda \sim n^{-1/6} \ . \tag{2.47}$$

Thus, substituting Eq.(2.46) into Eq.(2.47) yields

$$\lambda \sim \sqrt{a} \ . \tag{2.48}$$

Using this relation in the screened Coulomb potential given by Eq.(2.37), we can derive how this trapping potential decreases with decreasing lattice spacing:

$$V(r) \sim \mathrm{e}^{-1/\sqrt{a}} \ . \tag{2.49}$$

Below in Fig. 2.7, we present this decrease graphically for the $r = 1$ case, while the situation is the same for any r value, the trapping potential decreses as $\mathrm{e}^{-1/\sqrt{a}}$ as we decrese the lattice spacing a. It is clear from the above argument of Mott that at a transition value of $a = a_{MIT}$, the trapping potential will be weak enough for electrons to become delocalized all together at once, which will result in a correlation-induced first-order metal-insulator transition. Since the

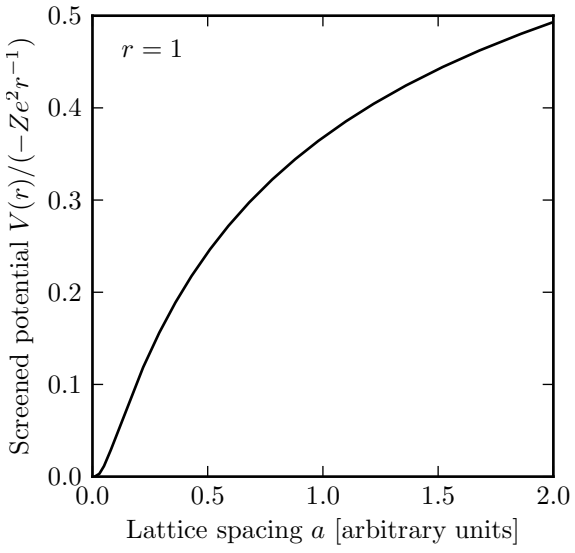

Figure 2.7: The screened Coulomb potential at $r = 1$ as a function of lattice spacing, a. The potential decreases as $\mathrm{e}^{-1/\sqrt{a}}$ with decreasing a.

lattice spacing and the electron density are interrelated, one can tune the electron density, n, instead of the lattice spacing a, to obtain this transition. We can accordingly recognize, by using Eq.(2.47) in Eq.(2.37), that

$$V(r) \sim \mathrm{e}^{-n^{1/6}} \ , \tag{2.50}$$

which provides the functional form of the decrease in trapping potential at radius r as the density is increased.

After careful calculations, Mott concluded that the metal-insulator transiton occurs at the transition value of $n = n_{MIT}$ given approximately by

$$n_{MIT} \approx \left(\frac{0.2}{a_0^*}\right)^3 \ , \tag{2.51}$$

where a_0^* is the effective Bohr radius for the material in concern [72, 73, 74, 75, 76]. This criterion for a metal-insulator transition was flourishingly applied to doped semiconductors after its introduction. Yet a better theoretical insight is provided within the Hubbard model, which will be discussed next.

2.3.4.3 The Hubbard model for metal-insulator transition

In order to illustrate the situation in a clearer fashion, let us consider the monovalent Na crystal in particular. In Fig. 2.8 below, a schematic picture for the atomic orbital bands is given. They all contribute to the electronic band structure of the Na crystal. The tight-binding approach yields decreasing atomic orbital band widths, with increasing lattice spacing, due to the decrease in hopping and overlap integrals [36, 37, 44]. For the Na crystal the $1s$, $2s$, and $2p$ atomic orbitals are completely filled with paired electrons, while the $3s$ band is half filled, thus the crystal shows metallic behavior. Although the band widths become narrover with increasing lattice constant, according to band theoretical approach the half filling of the $3s$ band is insensitive to the variation in a, as seen from Fig. 2.8 below. However, a large enough lattice spacing must yield very small hopping and overlap integrals, and thus an insulating phase.

Mott's argument, discussed in the previous subsection, can also be interpreted within this band picture. As the band width of the system decreases, the strong

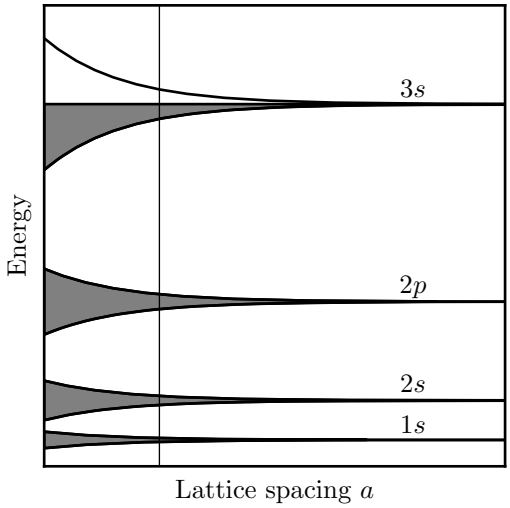

Figure 2.8: Schematic representation of the band widths in a Na crystal. The tight-binding approximation gives decreasing atomic orbital widths with increasing lattice spacing a. The thin vertical line represents the equilibrium lattice spacing in ambient conditions, while the shaded regions denote the filled atomic orbitals. Note that the $3s$ band is always half filled no matter what value a assumes (after [44]).

on-site Coulomb repulsion between the electrons on the same atomic site will cause all electrons to avoid each other and localize on different atoms. In this case, the condition for a metal-insulator transition, given in Eq.(2.51), can be expressed as [74]

$$W_{MIT} = 2zt \ , \tag{2.52}$$

where W_{MIT} is the band width value at the transition, z is the lattice coordination number, and t is the tight-binding hopping integral.

For the Na crystal lattice structure to be electrically conducting, the valence electrons must have the ability to hop between neighboring atoms, which will eventually yield "*charge fluctuations*". This charge fluctuating procedure can be represented as a reaction involving two neighboring atoms of a Na crystal:

$$\mathrm{Na} + \mathrm{Na} \longrightarrow \mathrm{Na}^{+} + \mathrm{Na}^{-} \ , \tag{2.53}$$

where the first and second atoms on each side of the reaction refer to two neighboring atomic sites. On the left-hand side, both atoms have one $3s$ electron each, while on the right-hand-side, a $3s$ electron is transferred from one atom (leaving it as a Na^{+} cation) to the other (promoting it to a Na^{-} cation), hence, a charge fluctuation is formed. But, in order to accomplish this reaction, the transferred electron must overcome the on-site Coulomb repulsion, U, that arises due to two electrons occupying the same atomic orbital. On-site Coulomb repulsion (or Hubbard U) was introduced in the previous section with Eq. (2.31) for the H_2 molecule. For the case of a Na crystal, the Hubbard U is given by

$$U = \int d\vec{r}_1 \int d\vec{r}_2 \ |\psi_{3s}(\vec{r}_1)|^2 \frac{e^2}{|\vec{r}_1 - \vec{r}_2|} |\psi_{3s}(\vec{r}_2)|^2 \ , \tag{2.54}$$

where $\vec{r}_1$ and $\vec{r}_2$ are the position vectors for the two electrons that are on the same atomic site. Thus, with the proper choice of zero-energy level as the energy of a Na atom with one valence electron, we can write the reaction above in terms of energy. On the left-hand side, both atomic sites have the same zero-energy each, while on the right-hand-side, the first atom has the energy of $-E_{3s}$ (since an electron with energy E_{3s} is lost) and the second atom has the energy of $E_{3s} + U$ (one extra $3s$ electron and the on-site Coulomb repulsion). Hence the difference of $[(-E_{3s}) + (E_{3s} + U)] - [(0) + (0)] = U$ must be compensated. This on-site Coulomb repulsion between the electrons sharing the same atomic orbital is the driving force for a metal-insulator transition.

In the case of isolated atoms, the Hubbard U is given by,

$$U = I - A \ , \tag{2.55}$$

where I is the ionization energy and A is the electron affinity of the atom [76]. The typical range of U is $1 - 10$ eV, but it is higher for insulators. In example, the electron affinities of copper (a metal) and carbon (an insulator) are close: $A_{Cu} \approx 1.23$ eV for copper and $A_C \approx 1.26$ eV for carbon. However, the ionization

energies are $I_{Cu} \approx 7.72$ eV and $I_C \approx 11.3$ eV. Hence, $U_{Cu} \approx 6.49$ eV is much smaller (about 35%) than $U_C \approx 10.0$ eV.

Thus, the reaction of Eq.(2.53) needs an amount of energy U, and this on-site Coulomb repulsion resists against the formation of charge fluctuations. But now, within this picture, how come is the Na crystal conducting, if the electrons are to sit one-by-one on each atomic site? One should thank to the kinetic energy contribution associated with the delocalization of electrons in the charge transfer process. Due to the kinetic exchange mechanism, once we lift the restriction of localization, electrons gain a kinetic energy, which was given in the tight-binding hopping integral form in Eq.(2.32) of the previous section for the case of an H_2 molecule. In the Na crystal case, this kinetic energy gain per hopping is given by

$$-t = -\int d\vec{r}\, \psi^*_{3s}(\vec{r}) \frac{e^2}{|\vec{r}-\vec{R}|} \psi_{3s}(\vec{r}) \ , \tag{2.56}$$

where $\vec{r}$ and $\vec{R}$ are position vectors for the electron and the nucleus respectively.

A connection to the Mott's view of variable lattice spacing should be given here. In the isolated atomic case, the crystal is obviously insulating. As the lattice spacing is decreased, the on-site Coulomb repulsion is suppressed due to the screening effect, and yet, the tight-binding hopping integral is enhanced as a result of closer nuclei. These two effects of decreasing the lattice spacing, or equivalently increasing the density, are always mutual. This yields a transition point where the kinetic energy overcomes the on-site Coulomb repulsion, and the crystal becomes metallic. This means that the transition is a result of the competition between the on-site Coulomb repulsion, U, and the tight-binding hopping integral, t. Such a metal-insulator transition induced by strong electron correlations is called Mott-Hubbard transition, after Hubbard's proposal of a lattice Hamiltonian that reflects the competing interactions of t and U [77, 78, 79]:

$$\mathscr{H} = -t \sum_{\langle ij \rangle} \sum_{\sigma} \left(c^\dagger_{i\sigma} c_{j\sigma} + c^\dagger_{j\sigma} c_{i\sigma} \right) + U \sum_i n_{i\uparrow} n_{i\downarrow} \ . \tag{2.57}$$

The "*Hubbard model*" we introduce above is in the second quantization formalism of quantum mechanics. Before a detailed analysis, first we need an insight on second quantization, that will be the subject of the next chapter.

2.3.5 Epilogue

Now we have seen how the strong electron correlation efects become significant, in particular, inducing antiferromagnetic insulating state and the Mott–Hubbard transition between metallic and insulating states. There exist numerous other phenomena related to the strongly correlated fermion systems in nature of condensed matter, *e.g.*, superconductivity, colossal magnetoresistance, Anderson localization, Wigner crystallization, *etc.*, as well as elementary particle physics, and yet, cosmology, *e.g.*, neutron stars, that lie outside the scope of this thesis.

It should be noted that although there are much more to argue about the Mott–Hubbard theory, like the difference between the Mott–Hubbard insulator and the charge transfer insulator, for the sake of our purposes, it will be enough to discuss only one more subject, that is the second quantization, which will benefit us the better understanding of the operators appearing in the Hubbard Hamiltonian, and that will be the subject of the next chapter.

Chapter 3

SECOND QUANTIZATION

3.1 Historical background

The aim of this chapter is to introduce second quantization. We will briefly derive the quantum field theoretical second quantization representation from the first quantization principles of the quantum mechanics. In basic quantum mechanics we deal with particles, while in the context of quantum field theory, we switch to dealing with fields. In many physical problems, it is reasonable to work with a field instead of working with many-particles. The field theoretical approach, while preserving all the symmetries/antisymmetries of the many-particles, establishes the particle-wave duality of the quantum nature in an eloborate theoretical ground.

Formulated in 1925-1926 by Heisenberg [84], Dirac [85] and Schrödinger [86, 87, 88, 89, 90], the essential subject of quantum mechanics is the motion of particles in space and time. Initially, it did not include the quantization of the electromagnetic field, and that is why the name "quantum mechanics". This formalism, either in matrix or in wave mechanics, is the "first quantization" representation of the quantum nature. However, in a very short time, in 1927, Dirac invented the "second quantization" representation and made the first attempt in quantum field theory [91]. Also in 1927, based on the second quantization formalism of the quantum field theory, he established the foundations in quantum electrodynamics [92]. In the very next year, in 1928, the theory of quantum electrodynamics (and the quantum field theory in general) was further developed by Jordan and Wigner, who suggested a transformation that yielded the representation of particles as quantized fields by second quantization [93].

It should not be misunderstood from the name that one takes two steps of quantization in order to reach the quantum field theory. In fact, there is a single quantization step in switching from classical to quantum theory of nature, but it is the difference of representations that we label as "first" and "second". The reader should not be worried at this point, since we will not dive into the deep ocean of quantum field theory of condensed matter physics, but just derive the second quantization formalism with a pragmatical instinct (that will usually follow the notation of [38]), although, any interested one may be referred to the advanced textbooks on the subject [33, 38, 94, 95, 96, 97, 98].

3.2 First quantization

3.2.1 Prologue

We will omit the details on the first quantization formalism of single-particle systems, since the subject is taught on undergraduate level today, yet the present author may argue that a necessity to discuss the matter during secondary school education has arisen already. However, in order to start from a point, we will give the time-independent one-particle Hamiltonian,

$$\mathscr{H} = -\frac{\hbar^2}{2m}\vec{\nabla}^2 + V(\vec{r}) \ , \tag{3.1}$$

and the accompanying time-independent Schrödinger equation,

$$\mathscr{H}|\phi_\alpha\rangle = E_\alpha|\phi_\alpha\rangle \ , \tag{3.2}$$

where α denotes an either discrete or continuous quantum number, as in the case of single particle in free space problem, or in general, a set of quantum numbers, as in the case of hydrogen atom problem, and where the ket, $|\phi_\alpha\rangle = |\phi_\alpha(\vec{r}\ )\rangle$, is the corresponding quantum state of the αth quantum level, forming up an orthonormal basis set of $\{|\phi_\alpha\rangle\}$. In the wave function formalism, the quantum state is represented as

$$\phi_\alpha(\vec{r}\,) \equiv \langle\vec{r}\,|\phi_\alpha(\vec{r}\,)\rangle \tag{3.3}$$

in the position space, while one needs a simple three-dimensional Fourier transform in order to switch to the momentum space.

3.2.2 Many-particle case

3.2.2.1 Indistinguishability

Indistinguishability of identical particles is a key concept in quantum many-particle physics. The N-particle wave function is given as

$$\psi_\alpha(\vec{r}_1, \ldots, \vec{r}_i, \ldots, \vec{r}_j, \ldots, \vec{r}_N) \ . \tag{3.4}$$

Now, let us define a permutation operator, P_{ij}, that exchanges the labels of the ith and jth particles:

$$\begin{aligned} P_{ij}\psi_\alpha(\vec{r}_1,\ldots,\vec{r}_i,\ldots,\vec{r}_j,\ldots,\vec{r}_N) &\equiv \psi_\alpha(\vec{r}_1,\ldots,\vec{r}_j,\ldots,\vec{r}_i,\ldots,\vec{r}_N) \\ &\equiv \lambda_P\psi_\alpha(\vec{r}_1,\ldots,\vec{r}_i,\ldots,\vec{r}_j,\ldots,\vec{r}_N)\ . \end{aligned} \quad (3.5)$$

Note the interchanged labels of i and j in the first line. Here, λ_P is defined as the eigenvalue of the operator P_{ij}. We could have defined so due to the commutation between P_{ij} and $\mathscr{H}$, that results in mutual eigenstates ψ_α. Using the fact that acting P_{ij} on an N-particle wave function twice must yield the same wave function, we can write

$$\begin{aligned} \psi_\alpha(\vec{r}_1,\ldots,\vec{r}_i,\ldots,\vec{r}_j,\ldots,\vec{r}_N) &= P_{ij}^2\psi_\alpha(\vec{r}_1,\ldots,\vec{r}_i,\ldots,\vec{r}_j,\ldots,\vec{r}_N) \\ &= P_{ij}\lambda_P\psi_\alpha(\vec{r}_1,\ldots,\vec{r}_i,\ldots,\vec{r}_j,\ldots,\vec{r}_N) \\ &= \lambda_P^2\psi_\alpha(\vec{r}_1,\ldots,\vec{r}_i,\ldots,\vec{r}_j,\ldots,\vec{r}_N) \end{aligned} \quad (3.6)$$

and hence,

$$\lambda_P^2 = 1 \quad \Rightarrow \quad \lambda_P = \pm 1\ . \quad (3.7)$$

This conclusion sets up two different and opposite types of quantum mechanical particles. The ones with $\lambda_P = +1$ are called bosons, while others with $\lambda_P = -1$ are fermions, and they assume different symmetries. Bosonic wave functions must be symmetric and fermionic wave functions must be antisymmetric under particle exchange, since

$$\psi_\alpha(\vec{r}_1,\ldots,\vec{r}_i,\ldots,\vec{r}_j,\ldots,\vec{r}_N) = \begin{cases} +\psi_\alpha(\vec{r}_1,\ldots,\vec{r}_j,\ldots,\vec{r}_i,\ldots,\vec{r}_N) & \text{, for bosons} \\ -\psi_\alpha(\vec{r}_1,\ldots,\vec{r}_j,\ldots,\vec{r}_i,\ldots,\vec{r}_N) & \text{, for fermions} \end{cases} . \quad (3.8)$$

We will restrict our further discussion on the fermionic case, for the particles we deal within the scope of this thesis are fermions, or to be more precise, electrons. Finally, we should note that the indistinguishability leads to the Pauli exclusion principle for fermions, and thus, it is experimentally verified in an exact manner.

3.2.2.2 Many-particle states as linear combinations of single-particle states

As we mentioned in the previous subsection, the single-particle states form an orthonormal basis set, $\{|\phi_\alpha\rangle\}$, or in the wave function formalism, $\{\phi_\alpha(\vec{r})\}$. Let us label the particles in an N-particle system with integers $1,\ldots,N$ and define the quantum state of ith particle in the α_ith quantum level as $\phi_{\alpha_i}(\vec{r}_i)$. The wave function of the N-particle system, given by $\psi_\alpha(\vec{r}_1,\ldots,\vec{r}_N)$, can be projected onto the basis state $\phi_{\alpha_1}(\vec{r}_1)$ to give an $(N-1)$-particle function, C, as

$$C_{\alpha_1}(\vec{r}_2,\ldots,\vec{r}_N) \equiv \int d\vec{r}_1 \; \phi^*_{\alpha_1}(\vec{r}_1) \; \psi_\alpha(\vec{r}_1,\ldots,\vec{r}_N) \; . \tag{3.9}$$

Using the orthonormality of the set $\{\phi_{\alpha_i}(\vec{r}_i)\}$, namely $\sum_{\alpha'_1}\int d\vec{r}'_1 \; \phi^*_{\alpha_1}(\vec{r}_1) \; \phi_{\alpha'_1}(\vec{r}'_1) = \delta(\vec{r}'_1-\vec{r}_1)\delta_{\alpha'_1,\alpha_1}$, and the above Eq.(3.9), we can write

$$\psi_\alpha(\vec{r}_1,\vec{r}_2,\ldots,\vec{r}_N) = \sum_{\alpha_1} \phi_{\alpha_1}(\vec{r}_1) \; C_{\alpha_1}(\vec{r}_2,\ldots,\vec{r}_N) \; . \tag{3.10}$$

Performing the same projection operation of $C_{\alpha_1}(\vec{r}_2,\ldots,\vec{r}_N)$ onto $\phi_{\alpha_2}(\vec{r}_2)$ yields

$$\begin{aligned} C_{\alpha_1,\alpha_2}(\vec{r}_3,\ldots,\vec{r}_N) &\equiv \int d\vec{r}_2 \; \phi^*_{\alpha_2}(\vec{r}_2) \; C_{\alpha_1}(\vec{r}_2,\ldots,\vec{r}_N) \; , \\ \psi_\alpha(\vec{r}_1,\vec{r}_2,\ldots,\vec{r}_N) &= \sum_{\alpha_1,\alpha_2} \phi_{\alpha_1}(\vec{r}_1) \; \phi_{\alpha_2}(\vec{r}_2) \; C_{\alpha_1,\alpha_2}(\vec{r}_3,\ldots,\vec{r}_N) \; . \end{aligned} \tag{3.11}$$

After the Nth such step of projection we end up with

$$\psi_\alpha(\vec{r}_1,\vec{r}_2,\ldots,\vec{r}_N) = \sum_{\alpha_1,\ldots,\alpha_N} C_{\alpha_1,\alpha_2,\ldots,\alpha_N} \; \phi_{\alpha_1}(\vec{r}_1) \; \phi_{\alpha_2}(\vec{r}_2) \; \cdots \; \phi_{\alpha_N}(\vec{r}_N) \; , \tag{3.12}$$

where $C_{\alpha_1,\alpha_2,\ldots,\alpha_N}$ is not a function of position vectors anymore, but just a complex number. Hence, we can express the N-particle wave function as a linear combination of single-particle wave functions. Note that we have actually exploited this property in order to develop the tight-binding approximation (also referred as liner combination of atomic orbitals method) described in the previous chapter.

One may think that the set $\{\prod_i \phi_{\alpha_i}(\vec{r}_i)\}$ could be used as a basis set to describe the N-particle wave function. However, this statement is merely wrong, since one cannot choose any set of linear coefficients $\{C_{\alpha_1,\alpha_2,\ldots,\alpha_N}\}$, and the reason lies in the

indistinguishability. The N-particle wave function must be either symmetric (for bosons) or antisymmetric (for fermions) under the particle interchange operation. But our efforts up to this point are not completely nonsense, and we can still use the product of single-particle wave functions as a basis set with proper coefficients. In case of an N-fermion system, this is achieved via the Slater determinant defined as

$$S_- \prod_i \phi_{\alpha_i}(\vec{r}_i) \equiv \frac{1}{\sqrt{N!}} \begin{vmatrix} \phi_{\alpha_1}(\vec{r}_1) & \phi_{\alpha_1}(\vec{r}_2) & \cdots & \phi_{\alpha_1}(\vec{r}_N) \\ \phi_{\alpha_2}(\vec{r}_1) & \phi_{\alpha_2}(\vec{r}_2) & \cdots & \phi_{\alpha_2}(\vec{r}_N) \\ \vdots & \vdots & \ddots & \vdots \\ \phi_{\alpha_N}(\vec{r}_1) & \phi_{\alpha_N}(\vec{r}_2) & \cdots & \phi_{\alpha_N}(\vec{r}_N) \end{vmatrix} . \tag{3.13}$$

Now, we can use these properly antisymmetrized states, $\{S_- \prod_i \phi_{\alpha_i}(\vec{r}_i)\}$, as a basis set, and express the N-fermion wave function as linear superpositions of them.

3.2.2.3 Representation of operators

3.2.2.3.1 One-particle operator: kinetic energy

Let us denote the kinetic energy operator (a one-particle operator) conjugate to the ith particle with

$$T_i \equiv -\frac{\hbar^2}{2m}\vec{\nabla}_i^2 , \tag{3.14}$$

which yields a total kinetic energy operator of

$$T = \sum_i T_i \tag{3.15}$$

for an N-particle system, since the kinetic energy of the whole system simply equals the sum of kinetic energies of individual particles. We can represent the operator T_i in the $\{|\phi_{\alpha_i}\rangle\}$ basis as

$$T_i = \sum_{\alpha_a,\alpha_b} \left[\int d\vec{r}_j \; \phi^*_{\alpha_a}(\vec{r}_j) \; T_j \; \phi_{\alpha_b}(\vec{r}_j) \right] |\phi_{\alpha_a}(\vec{r}_i)\rangle\langle\phi_{\alpha_b}(\vec{r}_i)| . \tag{3.16}$$

Here, the operator T_j under the integral, as defined in Eq.(3.14), takes the Laplacian of the wave function $\phi_{\alpha_b}(\vec{r}_j)$ and multiplies it by $-\frac{\hbar^2}{2m}$. Defining the integral

in brackets in the above equation as $T_{\alpha_a\alpha_b}$ yields the action of the total kinetic energy operator on a simple product state as

$$\begin{aligned} T\ & |\phi_{\alpha_1}(\vec{r}_1)\rangle|\phi_{\alpha_2}(\vec{r}_2)\rangle\cdots|\phi_{\alpha_i}(\vec{r}_i)\rangle\cdots|\phi_{\alpha_N}(\vec{r}_N)\rangle \\ &= \sum_i \sum_{\alpha_a,\alpha_b} T_{\alpha_a\alpha_b}|\phi_{\alpha_a}(\vec{r}_i)\rangle\langle\phi_{\alpha_b}(\vec{r}_i)|\cdot|\phi_{\alpha_1}(\vec{r}_1)\rangle|\phi_{\alpha_2}(\vec{r}_2)\rangle\cdots|\phi_{\alpha_i}(\vec{r}_i)\rangle\cdots|\phi_{\alpha_N}(\vec{r}_N)\rangle \\ &= \sum_i \sum_{\alpha_a,\alpha_b} T_{\alpha_a\alpha_b}\delta_{\alpha_b,\alpha_i}|\phi_{\alpha_1}(\vec{r}_1)\rangle|\phi_{\alpha_2}(\vec{r}_2)\rangle\cdots|\phi_{\alpha_a}(\vec{r}_i)\rangle\cdots|\phi_{\alpha_N}(\vec{r}_N)\rangle \\ &= \sum_i \sum_{\alpha_a} T_{\alpha_a\alpha_i}|\phi_{\alpha_1}(\vec{r}_1)\rangle|\phi_{\alpha_2}(\vec{r}_2)\rangle\cdots|\phi_{\alpha_a}(\vec{r}_i)\rangle\cdots|\phi_{\alpha_N}(\vec{r}_N)\rangle\ , \end{aligned} \tag{3.17}$$

where the Kronecker delta in the third line is due to the projection $\langle\phi_{\alpha_b}(\vec{r}_i)|\phi_{\alpha_i}(\vec{r}_i)\rangle$. Thus, we can express the act of the kinetic energy operator as the total act of changing the quantum level of all the ith particles from α_i to all levels α_a, with transition amplitudes $T_{\alpha_a\alpha_i}$ (*cf.* Fig. 3.1). It is therefore straightforward to extend this result to the properly antisymmetrized basis states given by the Slater determinant formalism.

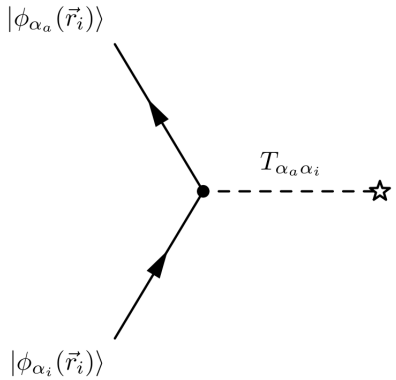

Figure 3.1: A schematic representation of the action of a single term in the kinetic energy operator, that changes the quantum level of the ith particle form α_i to α_a. The total action is found by summing over i and α_a.

3.2.2.3.2 Two-particle operator: Coulomb interaction

Likewise the one-particle operator case, we can define the Coulomb interaction operator (a two-particle operator) for the interaction between ith and jth particles

in the form,

$$V_{ij} \equiv \frac{e^2}{|\vec{r}_i - \vec{r}_j|} \ , \tag{3.18}$$

which yields a total Coulomb interaction operator of

$$V = \sum_{i<j} V_{ij} \tag{3.19}$$

Again in the $\{|\phi_{\alpha_i}\rangle\}$ base representation, this will yield

$$V_{ij} = \sum_{\substack{\alpha_a,\alpha_b \\ \alpha_c,\alpha_d}} V_{\alpha_a\alpha_b,\alpha_c\alpha_d} |\phi_{\alpha_a}(\vec{r}_i)\rangle |\phi_{\alpha_b}(\vec{r}_j)\rangle \langle\phi_{\alpha_c}(\vec{r}_i)| \langle\phi_{\alpha_d}(\vec{r}_j)| \ , \tag{3.20}$$

in which $V_{\alpha_a\alpha_b,\alpha_c\alpha_d}$ is defined as

$$V_{\alpha_a\alpha_b,\alpha_c\alpha_d} \equiv \int d\vec{r}_k \ d\vec{r}_\ell \ \phi^*_{\alpha_a}(\vec{r}_k) \ \phi^*_{\alpha_b}(\vec{r}_\ell) \ V_{k\ell} \ \phi_{\alpha_c}(\vec{r}_k) \ \phi_{\alpha_d}(\vec{r}_\ell) \ , \tag{3.21}$$

where $V_{k\ell}$ acting on $\phi_{\alpha_c}(\vec{r}_k)$ just multiplies the wave function with $\frac{e^2}{|\vec{r}_k - \vec{r}_\ell|}$. Thus, the total Coulomb interaction operator acts on the N-particle simple product states as

$$\begin{aligned}
V \ & |\phi_{\alpha_1}(\vec{r}_1)\rangle \cdots |\phi_{\alpha_i}(\vec{r}_i)\rangle \cdots |\phi_{\alpha_j}(\vec{r}_j)\rangle \cdots |\phi_{\alpha_N}(\vec{r}_N)\rangle \\
&= \sum_{i<j} \sum_{\substack{\alpha_a,\alpha_b \\ \alpha_c,\alpha_d}} V_{\alpha_a\alpha_b,\alpha_c\alpha_d} |\phi_{\alpha_a}(\vec{r}_i)\rangle |\phi_{\alpha_b}(\vec{r}_j)\rangle \langle\phi_{\alpha_c}(\vec{r}_i)| \langle\phi_{\alpha_d}(\vec{r}_j)| \cdot \\
&\qquad\qquad |\phi_{\alpha_1}(\vec{r}_1)\rangle \cdots |\phi_{\alpha_i}(\vec{r}_i)\rangle \cdots |\phi_{\alpha_j}(\vec{r}_j)\rangle \cdots |\phi_{\alpha_N}(\vec{r}_N)\rangle \\
&= \sum_{i<j} \sum_{\substack{\alpha_a,\alpha_b \\ \alpha_c,\alpha_d}} V_{\alpha_a\alpha_b,\alpha_c\alpha_d} \delta_{\alpha_c,\alpha_i} \delta_{\alpha_d,\alpha_j} |\phi_{\alpha_1}(\vec{r}_1)\rangle \cdots |\phi_{\alpha_a}(\vec{r}_i)\rangle \cdots |\phi_{\alpha_b}(\vec{r}_j)\rangle \cdots |\phi_{\alpha_N}(\vec{r}_N)\rangle \\
&= \sum_{i<j} \sum_{\alpha_a,\alpha_b} V_{\alpha_a\alpha_b,\alpha_i\alpha_j} |\phi_{\alpha_1}(\vec{r}_1)\rangle \cdots |\phi_{\alpha_a}(\vec{r}_i)\rangle \cdots |\phi_{\alpha_b}(\vec{r}_j)\rangle \cdots |\phi_{\alpha_N}(\vec{r}_N)\rangle \ ,
\end{aligned} \tag{3.22}$$

where a single term of the sum changes the quantum levels of the ith and jth particles form α_i and α_j to α_a and α_b with a transition amplitude of $V_{\alpha_a\alpha_b,\alpha_i\alpha_j}$ (*cf.* Fig. 3.2). The total action of the Coulomb interaction operator is reached with summations over all pairs (i,j), and all α_a and α_b.

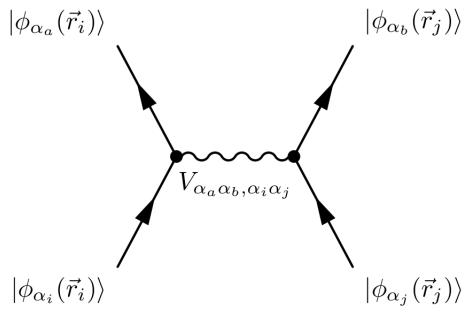

Figure 3.2: A schematic representation of the action of a single term in the Coulomb interaction operator, that changes the quantum levels of the ith and jth particles form α_i and α_j to α_a and α_b. The total action is found by summing over all pairs (i, j), and α_a and α_b.

3.2.3 Epilogue

Hence, we are now at a point to solve a quantum many-electron problem, once we define a kinetic energy operator for single electrons and a Coulomb interaction operator for pairs of electrons. Then, what makes the second quantization a necessity, if all it brings on the table is just a change of representation? In fact, we will benefit a lot, once we switch to a new representation, namely "*occupation number representation*", for which the details will be discussed in the next section.

3.3 Second quantization

3.3.1 Prologue

In order to figure out how much we can appreciate a new formalism based on the occupation number representation, let us first argue about the inadequacies of the first quantization formalism, that is established on the basis states set constructed by the states given in Eq.(3.13).

First of all, it is cumbersome to work with the states of the basis set, given by Slater determinants of what is given in Eq.(3.13). Even in the simplest case of calculating the overlap between two wave functions, one has to deal with $(N!)^2$ different products of single-particle states. Since we are mathematically working in the limit $N \to \infty$, this method will be so far from being practical.

Secondly, the first quantization formalism needs more improvement for accounting the variable particle number. It does not allow us to work in the grand canonical formulation of statistical mechanics, where a condition of constant-N is released, letting N to fluctuate. In the second quantization formalism of many-particle systems, these difficulties are removed in an eloborate theoretical fashion.

3.3.2 Occupation number representation and Fock space

In order to achieve a simpler formulation than the first quantization formalism of many-particle systems, we first realize that it is in fact an unnecessary bookkeeping of every wave function of all individual particles. The only thing that matters is to know how many particles occupy each state. Thus, the very first thing to define is the occupation number operator, $\hat{n}_\alpha$, that has the eigenstates $|n_\alpha\rangle$ with eigenvalues n_α, thus,

$$\hat{n}_\alpha |n_\alpha\rangle = n_\alpha |n_\alpha\rangle \ , \tag{3.23}$$

where n_α is the number of particles on the quantum level α. This immediately requires an identity for the total number of particles, namely

$$N = \sum_\alpha n_\alpha \ . \tag{3.24}$$

We should also note that any quantum level can be either empty or filled by one fermion due to Pauli exclusion principle, which is the result of the antisymmetry of fermionic wave functions upon exchange of particles. This requirement led to the complicated Slater determinant formalism in the first quantization picture, however, as we shall see, it will be implicitly satisfied in the occupation number representation of the second quantization formalism.

The occupation number states for each possible quantum level, $\{|n_\alpha\rangle\}$, leads to a new representation for the N-particle system. We can represent any state of the whole system by giving the number of particles at each state. This means the set of all possible states in the form

$$|n_1, n_2, \ldots\rangle \tag{3.25}$$

together with the identity given in Eq.(3.24) can be used as a basis set for the system of N-particles. It is worth noting that, how we order the quantum states (as $1, 2, \ldots$) is essential, especially for the fermionic case, and we will discuss this ordering issue later. For now, let us state that, any wave function of the N-particle system, $|\psi\rangle$, can be written in the form of a linear superposition of the occupation number states, *i.e.*,

$$|\psi\rangle = {\sum_{n_1,n_2,\ldots}}' c_{n_1,n_2,\ldots}|n_1, n_2, \ldots\rangle \ , \tag{3.26}$$

where the prime on the sum indicates that it is a restricted one with the condition $\sum_\alpha n_\alpha = N$.

Let us denote the space spanned by N-particle occupation number states in the form of Eq.(3.25) as $\mathcal{F}^N$. The Hilbert space spanned by the occupation number states of undetermined total particle number is called a "*Fock space*", and thus, we define it by

$$\mathcal{F} = \bigoplus_{N=0}^{\infty} \mathcal{F}^N \ . \tag{3.27}$$

Notice the zero-particle state is also included in the Fock space, and this is of essential importance. The space $\mathcal{F}^0$ is called the "*vacuum space*" and its only element is the "*vacuum state*", denoted by $|0\rangle$.

If we claim that this new second quantization representation is equivaent to the first quantization representation given in previous section, we need to establish the connection between these two formalisms.

3.3.3 Creation–annihilation operators and CAR algebra

The definition of the occupation number representation and the Fock space was the first step in our efforts to simplify the formalism, however, we are not done yet. We need creation and annihilation operators in order to complete the equivalance of the first and second quantization formalisms. As we stated earlier, we will omit the bosonic case, and choose to work with fermions only.

Let us define the (fermionic) "*creation operator*", $c_\alpha^\dagger$, whose act is to increase the occupation number n_α by 1:

$$c_\alpha^\dagger \left|n_1, n_2, \ldots, n_\alpha, \ldots\right\rangle \equiv \zeta_{n_\alpha}^{+} \left|n_1, n_2, \ldots, n_\alpha + 1, \ldots\right\rangle , \tag{3.28}$$

where $\zeta_{n_\alpha}^{+}$ is a normalization constant to be determined soon. It is obvious that the only nonzero elements of the creation operator matrix are the ones in the form $\langle n_1, \ldots, n_\alpha + 1 \ldots | c_\alpha^\dagger | n_1, \ldots, n_\alpha, \ldots\rangle$. Thus, from the complex conjugation, it follows that the only nonzero matrix elements of the operator $c_\alpha \equiv \left(c_\alpha^\dagger\right)^\dagger$ are $\langle n_1, \ldots, n_\alpha + 1 \ldots | c_\alpha^\dagger | n_1, \ldots, n_\alpha, \ldots\rangle^* = \langle n_1, \ldots, n_\alpha \ldots | c_\alpha | n_1, \ldots, n_\alpha + 1, \ldots\rangle$. Hence, we name the operator c_α as the "*annihilation operator*", since it decreases the occupation number $n_\alpha + 1$ by 1 to n_α, thus, we can write

$$c_\alpha \left|n_1, n_2, \ldots, n_\alpha, \ldots\right\rangle \equiv \zeta_{n_\alpha}^{-} \left|n_1, n_2, \ldots, n_\alpha - 1, \ldots\right\rangle \tag{3.29}$$

in a manner similar to creation operator.

The fermionic states must be antisymmetric with respect to an interchange between two fermions, thus, it must be satisfied that

$$\left|\ldots, n_\alpha = 1, \ldots, n_\gamma = 1, \ldots\right\rangle = -\left|\ldots, n_\gamma = 1, \ldots, n_\alpha = 1, \ldots\right\rangle , \tag{3.30}$$

and this requirement means that the ordering of the quantum levels matters. Furthermore, this antisymmetry leads to the fact that $c_\alpha^\dagger$ and $c_\gamma^\dagger$ must anticommute. In order to see this, let us rewrite Eq.(3.30) as

$$|\ldots, n_\alpha = 1, \ldots, n_\gamma = 1, \ldots\rangle = c_\alpha^\dagger c_\gamma^\dagger |\ldots, n_\alpha = 0, \ldots, n_\gamma = 0, \ldots\rangle$$
$$= -|\ldots, n_\gamma = 1, \ldots, n_\alpha = 1, \ldots\rangle = -c_\gamma^\dagger c_\alpha^\dagger |\ldots, n_\gamma = 0, \ldots, n_\alpha = 0, \ldots\rangle \,, \quad (3.31)$$

which yields $c_\alpha^\dagger c_\gamma^\dagger = -c_\gamma^\dagger c_\alpha^\dagger$, hence $\{c_\alpha^\dagger, c_\gamma^\dagger\} = 0$, whose Hermitian adjoint yields the fact that c_α and c_γ also anticommute: $\{c_\alpha, c_\gamma\} = 0$. In order to obtain one last anticommutation relation to complete the algebra, we need the normalization factors appearing in the definitions of creation and annihilation operators, *i.e.*, Eqs.(3.28) and (3.29).

We cannot add another fermion into an already filled quantum level, and similarly an already empty level cannot be further emptied. These facts yield

$$c_\alpha^\dagger |\ldots, n_\alpha = 1, \ldots\rangle = 0 \,, \quad (3.32)$$
$$c_\alpha |\ldots, n_\alpha = 0, \ldots\rangle = 0 \,, \quad (3.33)$$

which means we must demand $\zeta_1^+ = 0$ and $\zeta_0^- = 0$. For the two remaining normalization constants, we have the option to choose

$$c_\alpha^\dagger |\ldots, n_\alpha = 0, \ldots\rangle = |\ldots, n_\alpha = 1, \ldots\rangle \,, \quad (3.34)$$

hence, $\zeta_0^+ = 1$. This choice yields $\zeta_1^- = 1$, since by complex conjugation, it follows that $\langle \ldots, n_\alpha = 1 \ldots | c_\alpha^\dagger | \ldots, n_\alpha = 0, \ldots\rangle^* = \langle \ldots, n_\alpha = 0 \ldots | c_\alpha | \ldots, n_\alpha = 1, \ldots\rangle$.

Now, let us demonstrate the issue for the anticommutators between c_α and $c_\gamma^\dagger$. If we choose $\gamma = \alpha$, we clearly see that $c_\alpha c_\alpha^\dagger |\ldots, n_\alpha = 0, \ldots\rangle = |\ldots, n_\alpha = 0, \ldots\rangle$, but $c_\alpha^\dagger c_\alpha |\ldots, n_\alpha = 0, \ldots\rangle = 0$, which yields

$$\{c_\alpha, c_\alpha^\dagger\} |\ldots, n_\alpha = 0, \ldots\rangle = |\ldots, n_\alpha = 0, \ldots\rangle \,. \quad (3.35)$$

Similarly, $c_\alpha^\dagger c_\alpha |\ldots, n_\alpha = 1, \ldots\rangle = |\ldots, n_\alpha = 1, \ldots\rangle$ and $c_\alpha c_\alpha^\dagger |\ldots, n_\alpha = 1, \ldots\rangle = 0$ yield

$$\{c_\alpha, c_\alpha^\dagger\} |\ldots, n_\alpha = 1, \ldots\rangle = |\ldots, n_\alpha = 1, \ldots\rangle \quad (3.36)$$

From Eqs.(3.35) and (3.36) we conclude that $\{c_\alpha, c_\alpha^\dagger\} = 1$. Similar arguments yield $\{c_\alpha, c_\gamma^\dagger\} = 0$ for the case $\gamma \neq \alpha$.

In order to summarize, the operator algebra for the fermionic creation and annihilation operators is given by

$$\begin{aligned} \{c_\alpha^\dagger, c_\gamma^\dagger\} &= 0 \ , \\ \{c_\alpha, c_\gamma\} &= 0 \ , \\ \{c_\alpha, c_\gamma^\dagger\} &= \delta_{\alpha,\gamma} \ , \end{aligned} \tag{3.37}$$

and called "*CAR algebra*", for it is based on *C*anonical *A*nticommutation *R*elations. The situation is very similar for bosons, for which a CCR (canonical commutation relations) algebra can be constructed for bosonic creation and annihilation operators, $b_\alpha^\dagger$ and b_α.

3.3.4 Equivalence to first quantization

Let us remind that we have not constructed the required link between the first and second quantization representations. For this establishment, we first need to show that the occupation number operator $\hat{n}_\alpha$ can be written in terms of creation and annihilation operators.

First of all, we notice that

$$\begin{aligned} (c_\alpha^\dagger)^2 &= 0 \ , \\ (c_\alpha)^2 &= 0 \end{aligned} \tag{3.38}$$

as a result of the CAR algebra, which in fact results from the antisymmetrized fermionic states. Note that the Pauli exclusion principle, that restricts the maximum occupation number to 1, is strictly interconnected to the CAR algebra, and the antisymmetry. Thus, the requirement of antisymmetric wave functions is implicitly satisfied within the CAR algebra, *i.e.*, we do not need to explicitly antisymmetrize the states given with the occupation number representation. We had to implement this antisymmetry requirement by Slater determinant formal-

ism in the first quantization representation. The unnecessary bookkeeping of wave functions, that leads to cumbersome computations, is nevermore the issue.

Another immediate consequence of the CAR algebra given by Eq.(3.37) is that it results in the commutation relations

$$\begin{aligned} \left[c_\alpha^\dagger c_\alpha, c_\alpha\right] &= -c_\alpha \ , \\ \left[c_\alpha^\dagger c_\alpha, c_\alpha^\dagger\right] &= c_\alpha^\dagger \ , \end{aligned} \tag{3.39}$$

which means that, $c_\alpha^\dagger$ (c_α) increases (decreases) the eigenvalues of the operator $c_\alpha^\dagger c_\alpha$ by 1. Here comes the intution of whether we can write the occupation number operator as $c_\alpha^\dagger c_\alpha$. We can also write

$$(c_\alpha^\dagger c_\alpha)^2 = c_\alpha^\dagger c_\alpha c_\alpha^\dagger c_\alpha = c_\alpha^\dagger (c_\alpha c_\alpha^\dagger) c_\alpha = c_\alpha^\dagger (1 - c_\alpha^\dagger c_\alpha) c_\alpha = c_\alpha^\dagger c_\alpha \ , \tag{3.40}$$

where we used Eq.(3.38) in the last step, and Eq.(3.37) in the previous one. This equation may also be written as

$$c_\alpha^\dagger c_\alpha (c_\alpha^\dagger c_\alpha - 1) = 0 \ , \tag{3.41}$$

which means that the operator $c_\alpha^\dagger c_\alpha$ has eigenvalues of 0 and 1, and hence, it is noting but the occupation number operator, $\hat{n}_\alpha$. Therefore, in order to summarize, we have

$$c_\alpha^\dagger c_\alpha |n_\alpha\rangle = n_\alpha |n_\alpha\rangle \quad \text{with} \quad n_\alpha = 0, 1$$

and

$$c_\alpha^\dagger |0\rangle = |1\rangle \ , \ c_\alpha^\dagger |1\rangle = 0 \ , \ c_\alpha |0\rangle = 0 \ , \ c_\alpha |1\rangle = |0\rangle \ . \tag{3.42}$$

This implies the connection between the Slater determinant states of the first quantization and the occupation number states of the second quantization:

$$S_- |\phi_{\alpha_1}(\vec{r}_1)\rangle |\phi_{\alpha_2}(\vec{r}_2)\rangle \cdots |\phi_{\alpha_N}(\vec{r}_N)\rangle = c_{\alpha_1}^\dagger c_{\alpha_2}^\dagger \cdots c_{\alpha_N}^\dagger |0\rangle \ , \tag{3.43}$$

where totally antisymmetric N-fermions are represented on both sides via first and second quantization formalisms, therefore, the equivalence of both representations is established.

3.3.5 Normal order

Since any two creation operators, $c_\alpha^\dagger$ and $c_\gamma^\dagger$, do not commute with each other, the order of the creation operators appearing in the right-hand side of Eq.(3.43) matters. This is equivalent to the significance of the ordering of quantum levels as mentioned before. For our main concern in this thesis only includes the electrons that can occupy the valence orbitals of the atoms arranged in a periodic array of positions, we can construct a very simple and basic ordering for the creation operators. For simplicity, let us assume a one-dimensional periodic array of N atoms, for which we can label the valence orbitals (quantum levels) as $\alpha = 1, 2, \ldots N$, starting from the atom at one end of the chain. Through out this section we will omit the consideration of the spin degree of freedom, and simply assume that each atom can be either empty or full in valence electrons. It is obvious that the situation can be fairly extended to the three-dimensional case with the consideration of spin. Thus, the creation operators, that create electrons at the atomic orbitals, can be easily ordered for the crystalline case, however, another ordering issue arises when we consider creation and annihilation operators together, since they also do not commute with each other.

We must choose a conventional order for the products of creation and annihilation operators. For example, if we are to convert a state to another one (both in the occupation number representation), we may well need to consider the product of operators in the form, *e.g.*, $c_\alpha^\dagger c_\gamma c_\eta^\dagger c_\gamma^\dagger c_\varrho$. In such cases we choose the convention of "*normal order*", also referred as "*Wick order*". A product of creation and annihilation operators is normal ordered if all the creation operators are to the left of all the annihilation operators. Assuming an operator C in the form of a product of creation and annihilation operators, $:C:$ denotes the normal ordered operator. The normal ordering process is performed by considering the CAR algebra given in Eq.(3.37).

The situation is pretty simple for a single quantum level α. The operator $c_\alpha^\dagger c_\alpha$ is already normal ordered and we denote it by $:c_\alpha^\dagger c_\alpha: = c_\alpha^\dagger c_\alpha$, however, the operator $c_\alpha c_\alpha^\dagger$ is not normal ordered, in fact it is *antinormal ordered*, and it follows $:c_\alpha c_\alpha^\dagger: = -c_\alpha^\dagger c_\alpha$, where we introduced a minus sign due to a single interchange

in the order of the operators, following the CAR algebra. Any other product of operators that contains more than two operators of the same quantum level is simply zero due to Eq.(3.38). In example, $:c_\alpha^\dagger c_\alpha c_\alpha^\dagger: = -c_\alpha^\dagger c_\alpha^\dagger c_\alpha = 0$.

Let us consider the ordered multiple quantum levels of $\alpha = 1, 2, 3, \dots$, and begin with products of two operators. The simplest case is again $:c_1^\dagger c_2: = c_1^\dagger c_2$, since the operator is already normal ordered. Next we should give $:c_1 c_2^\dagger: = -c_2^\dagger c_1$, because of the single interchange in the order of operators. For products of more than two operators, the situation follows the simple rules of CAR algebra. In example, we write $:c_1 c_2^\dagger c_1^\dagger: = c_2^\dagger c_1^\dagger c_1 = -c_1^\dagger c_2^\dagger c_1$, where in the first step we made two interchanges betweeen the operators (hence the positive sign), and in the second step we further ordered the creation operators with respect to energy labels, that yielded the negative sign.

Here, one may question the need for normal ordering. In order to emphasise the necessity of choosing a convention for ordering, we will illustrate the point with the following example. Every state in the occupation number representation must be constructed from the vacuum state, $|0\rangle$, by the acts of several creation operators, in order to form the equivalence between the first and the second quantization formalisms. Thus, we write a state as

$$|n_1, n_2, n_3\rangle = (c_1^\dagger)^{n_1} (c_2^\dagger)^{n_2} (c_3^\dagger)^{n_3} |0\rangle \ , \tag{3.44}$$

where we restricted the situation for three quantum levels, or three crystal sites, for the sake of simplicity. As a further simplification, let us assume $n_1 = n_2 = n_3 = 1$ above. It is obvious that the order of creation operators appearing in the above equation is of paramount significance, since for example, $c_1^\dagger c_3^\dagger c_2^\dagger \neq c_3^\dagger c_1^\dagger c_2^\dagger$ within the CAR algebra. We can overcome this issue with a proper choice of ordering in the quantum levels, as we did when we labeled the atomic orbitals of the lattice in the beginning of this subsection. The next problem with ordering arises when we consider an act of, for example, c_2 onto such a state given above, *i.e.*, $c_2|1,1,1\rangle = c_2 c_1^\dagger c_2^\dagger c_3^\dagger |0\rangle$. Here again, since $c_2 c_1^\dagger c_3^\dagger c_2^\dagger \neq c_3^\dagger c_2 c_1^\dagger c_2^\dagger$, we need another choice of ordering. The normal ordering provides a convention for this issue, and it is in fact the commonly accepted one.

3.3.6 Operators in second quantization representation

We have seen that the occupation number operator can be written in terms of creation and annihilation operators as $\hat{n}_\alpha = c_\alpha^\dagger c_\alpha$. This is in fact a reflection of a more general rule, *i.e.*, we can write any operator in terms of creation and annihilation operators, utilizing the link between first and second quantization representations given by Eq.(3.43). Since the two most important operators for our concern are the kinetic energy and the Coulomb interaction operators, we will express those in the second quantization formalism in this substection.

Let us recall that the kinetic energy operator, T, was represented in first quantization formalism as given in Eq.(3.17), where we left the antisymmetrization process, that can be implemented easily by multiplying Eq.(3.17) with S_- on the left. Note that, since S_- commutes with T, this antisymmetrization operation is a trivial one. Remembering that the total kinetic energy operator can be written as $T = \sum_i T_i$, for now, let us concentrate on the kinetic energy of the ith particle, given by Eq.(3.16), that reads

$$T_i = \sum_{\alpha_a,\alpha_b} T_{\alpha_a\alpha_b} |\phi_{\alpha_a}(\vec{r}_i)\rangle\langle\phi_{\alpha_b}(\vec{r}_i)| \ . \tag{3.45}$$

Acting this operator on an antisymmetrized arbitrary state yields

$$\begin{aligned} T_i\Big[S_-|\phi_{\alpha_1}(\vec{r}_1)\rangle\cdots|\phi_{\alpha_i}(\vec{r}_i)\rangle\cdots|\phi_{\alpha_N}(\vec{r}_N)\rangle\Big] \\ = \sum_{\alpha_a,\alpha_b} T_{\alpha_a\alpha_b}\delta_{\alpha_b,\alpha_i}\Big[S_-|\phi_{\alpha_1}(\vec{r}_1)\rangle\cdots|\phi_{\alpha_a}(\vec{r}_i)\rangle\cdots|\phi_{\alpha_N}(\vec{r}_N)\rangle\Big] \ , \end{aligned} \tag{3.46}$$

for which we can use the link between first and second quantization representations given with Eq.(3.43) now to write

$$T_i\Big[c_{\alpha_1}^\dagger\cdots c_{\alpha_i}^\dagger\cdots c_{\alpha_N}^\dagger|0\rangle\Big] = \sum_{\alpha_a,\alpha_b} T_{\alpha_a\alpha_b}\delta_{\alpha_b,\alpha_i}\Big[c_{\alpha_1}^\dagger\cdots c_{\alpha_a}^\dagger\cdots c_{\alpha_N}^\dagger|0\rangle\Big] \ , \tag{3.47}$$

Here, $c_{\alpha_a}^\dagger$ resides on the α_ith quantum level (or the α_ith lattice site) on the right-hand side. Note that, since we are working in the fermionic case, the $c_{\alpha_i}^\dagger$ cannot appear more than once on the left-hand side, due to the Pauli exclusion principle

expressed in Eq.(3.38). Thus, the operator $c^\dagger_{\alpha_i}$ may either appear once or may not appear on the left-hand side. If it does not appear, the above equation will readily lead to $0 = 0$, while if it does appear, we have to transform the state on the right-hand side into the original one, that T_i acts on, in order to find the effect of an action of T_i. Therefore, we have to insert $c^\dagger_{\alpha_i}$ instead of $c^\dagger_{\alpha_a}$ on the right-hand side. In order to accomplish this, first we note that for any α,

$$c_\alpha c^\dagger_\alpha|0\rangle = c_\alpha|0,\ldots 0, n_\alpha = 1, 0, \ldots, 0\rangle = |0\rangle \ , \tag{3.48}$$

which lets us to write

$$c^\dagger_{\alpha_a}|0\rangle = c^\dagger_{\alpha_a}\left(c_{\alpha_i}c^\dagger_{\alpha_i}\right)|0\rangle = \left(c^\dagger_{\alpha_a}c_{\alpha_i}\right)c^\dagger_{\alpha_i}|0\rangle \ . \tag{3.49}$$

Thus, we can write $\left(c^\dagger_{\alpha_a}c_{\alpha_i}\right)c^\dagger_{\alpha_i}$ instead of $c^\dagger_{\alpha_a}$ in the right-hand side of Eq.(3.47), that will read

$$T_i\Big[c^\dagger_{\alpha_1}\cdots c^\dagger_{\alpha_i}\cdots c^\dagger_{\alpha_N}|0\rangle\Big] = \sum_{\alpha_a,\alpha_b} T_{\alpha_a\alpha_b}\delta_{\alpha_b,\alpha_i}\Big[c^\dagger_{\alpha_1}\cdots\left(c^\dagger_{\alpha_a}c_{\alpha_i}\right)c^\dagger_{\alpha_i}\cdots c^\dagger_{\alpha_N}|0\rangle\Big] \ . \tag{3.50}$$

Now, we can take the operators in the paranthesis to the very left, outside the brackets. Every interchange of one of the operators in $\left(c^\dagger_{\alpha_a}c_{\alpha_i}\right)$ with a creation operator to the left will lead a minus sign, however, since we are doing this job twice, in the end, the procedure will always end up with a plus sign. Therefore, we can write

$$\begin{aligned} T_i\Big[c^\dagger_{\alpha_1}\cdots c^\dagger_{\alpha_i}\cdots c^\dagger_{\alpha_N}|0\rangle\Big] &= \sum_{\alpha_a,\alpha_b} T_{\alpha_a\alpha_b}\left(c^\dagger_{\alpha_a}c_{\alpha_i}\right)\delta_{\alpha_b,\alpha_i}\Big[c^\dagger_{\alpha_1}\cdots c^\dagger_{\alpha_i}\cdots c^\dagger_{\alpha_N}|0\rangle\Big] \\ &= \sum_{\alpha_a} T_{\alpha_a\alpha_i}\left(c^\dagger_{\alpha_a}c_{\alpha_i}\right)\Big[c^\dagger_{\alpha_1}\cdots c^\dagger_{\alpha_i}\cdots c^\dagger_{\alpha_N}|0\rangle\Big] \ , \end{aligned} \tag{3.51}$$

which, in fact, can be written as an operator identity,

$$T_i = \sum_{\alpha_a} T_{\alpha_a\alpha_i}c^\dagger_{\alpha_a}c_{\alpha_i} \ . \tag{3.52}$$

Note that, T_i acting on a state with $\alpha_i = 0$ will destroy the state as expected. Finally, using $T = \sum_i T_i$, for the total kinetic energy operator, we conclude

$$T = \sum_{\alpha_i,\alpha_j} T_{\alpha_i\alpha_j} c^\dagger_{\alpha_i} c_{\alpha_j} \ . \tag{3.53}$$

Hence, we can justly generalize the result above to an arbitrary one-particle operator by accordingly defining the integral $T_{\alpha_i\alpha_j}$. Furthermore, we can also generalize the situation to any m-particle operators, that yields the result that, any operator can be represented by linear superpositions of products of creation and annihilation operators with linear coefficients in the form of properly defined integrals, that are actually the matrix elements of the operator in the first quantization representation. One of these operators, a two-particle operator, namely the Coulomb interaction operator, is particularly interesting for our purposes. One can follow a similar procedure to the one described above in order to obtain

$$V = \sum_{\substack{\alpha_i<\alpha_j \\ \alpha_k,\alpha_\ell}} V_{\alpha_i\alpha_j,\alpha_k\alpha_\ell} c^\dagger_{\alpha_i} c^\dagger_{\alpha_j} c_{\alpha_\ell} c_{\alpha_k} \ . \tag{3.54}$$

3.3.7 Epilogue

It is worth noting once again that all the required antisymmetry properties are hidden in the creation and annihilation operators that obey the CAR algebra. The transition matrix amplitudes that appear in Eqs.(3.53) and (3.54) are just numbers, which do not demand any kind of symmetry to satisfy. Thus, as we promised, the antisymmetrization procedure is greatly reduced, and all we need to do is determining a protocol of ordering, and that requires no complicated algebra.

Therefore, we can construct a quantum mechanical Hamiltonian in the second quantization picture for the strongly correlated electron systems, that we mentioned in the previous chapter. Recalling that for such systems, the physical behavior, particularly the metal-insulator transition, is induced by the competing kinetic energy and on-site Coulomb repulsion, we propose a Hamiltonian in the form

$$\mathscr{H} = T + V \ , \tag{3.55}$$

where T and V are in the form given above in Eqs.(3.53) and (3.54) respectively.

Now that we are armed with all the required tools of second quantization, we hope to understand the Hubbard model in theoretical details, however, we need one more step ahead, that is a discussion on tight-binding approximation.

3.4 Tight-binding approach and Hubbard model revisited

3.4.1 Prologue

The previous chapter was finalized with our discussion on the Mott–Hubbard metal-insulator transition, presentation of the Mott theory, and introduction of the Hubbard model, given by the quantum mechanical Hamiltonian in the second quantization formalism in Eq.(2.57). Now, we can readily understand what it is all about, with some further definitions, *i.e.*, definition of the second quantization creation and annihilation operators in the case of electrons with spin-up and -down on atomic orbitals within a periodic lattice. This is, in fact, equivalent to characterization of the quantum levels, denoted by $\{\alpha\}$ in previous sections, and we will use the tight-binding approximation to accomplish this task.

3.4.2 Creation and annihilation operators

We have briefly intoduced the tight-binding approximation in the previous chapter. Here, we will discuss the subject in more details and obtain the second quantization operators in the tight-binding scheme, by mainly following the formulation of [98].

The tight-binding approach begins with an assumption of electron wave functions being mainly localized at lattice sites, or in other words, *tightly bound* to atomic nuclei. This actually arises due to a large lattice spacing, but not large enough to consider the atoms as completely isolated, rather assuming the overlap integrals are small.

Firstly, within this approximate scheme, it is convenient to benefit from the symmetry properties of the underlying periodic lattice, and represent the Hamiltonian operators in a basis set of the so called "*Wannier states*", given by

$$|\phi_{i\alpha}(\vec{r})\rangle \equiv \frac{1}{\sqrt{N}} \sum_{\vec{k}}^{BZ} \mathrm{e}^{-\mathrm{i}\vec{k}\cdot\vec{R}_i} |\phi_{\vec{k}\alpha}(\vec{r})\rangle \ , \tag{3.56}$$

where the sum runs over all momenta, $\vec{k}$, in the first Brillouin zone of the reciprocal lattice, R_i denotes the position of the ith lattice site, and $|\phi_{\vec{k}\alpha}(\vec{r})\rangle$ are the Bloch wave functions defined according to the Bloch theorem as $|\phi_{\vec{k}\alpha}(\vec{r}+\vec{R}_j)\rangle = \mathrm{e}^{\mathrm{i}\vec{k}\cdot\vec{R}_j}|\phi_{\vec{k}\alpha}(\vec{r})\rangle$ (*cf.* Theorem 1). The Bloch wave functions can be obtained by the inverse Fourier transform of $|\phi_{i\alpha}(\vec{r})\rangle$ in accord with the above equation.

Secondly, we realize that the set of Wannier states, $\{|\phi_{i\alpha}(\vec{r})\rangle\}$, form a complete orthonormal basis set and can be used to represent the operators of the second quantization formalism. This leads us to write

$$c_\alpha^\dagger(\vec{r}) = \sum_i \phi_{i\alpha}^*(\vec{r})\, c_{i\alpha}^\dagger \ . \tag{3.57}$$

Therefore, this establishes a link between the real space and the Wannier space representations. One may be confused with the dependence of $c_\alpha^\dagger(\vec{r})$ on the position, $\vec{r}$, but actually, that is a dependence which we have omitted writing explicitly up to this point, for the sake of simplicity. It can be clearly seen from Eq.(3.43) that the dependence of creation operator on position is a necessity in fact. By using the orthonormality of the Wannier functions, we can write the creation operator in the Wannier base as

$$c_{i\alpha}^\dagger = \int d\vec{r}\, \phi_{i\alpha}(\vec{r})\, c_\alpha^\dagger(\vec{r}) \ , \tag{3.58}$$

and by Hermitian conjugation we have

$$\begin{aligned} c_\alpha(\vec{r}\,) &= \sum_i \phi_{i\alpha}(\vec{r})\, c_{i\alpha} \ , \\ c_{i\alpha} &= \int d\vec{r}\, \phi_{i\alpha}(\vec{r})^*\, c_\alpha(\vec{r}) \ . \end{aligned} \tag{3.59}$$

Just like the transformation between Bloch and Wannier states, we can also define creation and annihilation operators in the momentum space as

$$\begin{aligned} c_{\vec{k}\alpha}^\dagger &= \frac{1}{\sqrt{N}} \sum_i \mathrm{e}^{\mathrm{i}\vec{k}\cdot\vec{R}_i} c_{i\alpha}^\dagger \ , \\ c_{\vec{k}\alpha} &= \frac{1}{\sqrt{N}} \sum_i \mathrm{e}^{-\mathrm{i}\vec{k}\cdot\vec{R}_i} c_{i\alpha} \ . \end{aligned} \tag{3.60}$$

3.4.3 Kinetic energy

Using the creation and annihilation operators given above in the tight-binding scheme, a simplification comes with the fact that the Bloch electrons have the kinetic energy $\epsilon_{\vec{k}} = \frac{\hbar^2|\vec{k}|^2}{2m}$, and we can diagonalize the kinetic energy operator in the

Bloch states representation. Besides, we assume that the kinetic energy operator does not change the quantum level α of the electron, which is a fair assumption, especially for the charge transfer (hopping) process we defined in previous chapter. In the hopping process, the quantum level, labeled by α, describes the spin quantum number, σ, of the electron, which is preserved in the process. We denote the possible values of the spin quantum number by $\sigma =\uparrow$ and $\sigma =\downarrow$. Therefore, for the kinetic energy operator, we write

$$\begin{aligned} T &= \sum_{\vec{k}}^{BZ}\sum_{\sigma} \epsilon_{\vec{k}}\, c^{\dagger}_{\vec{k}\sigma} c_{\vec{k}\sigma} \\ &= \frac{1}{N}\sum_{ij}\sum_{\vec{k}}^{BZ}\sum_{\sigma} \mathrm{e}^{\mathrm{i}\vec{k}\cdot(\vec{R}_i-\vec{R}_j)}\epsilon_{\vec{k}}\, c^{\dagger}_{i\sigma} c_{j\sigma} \qquad (3.61) \\ &\equiv \sum_{ij}\sum_{\sigma} t_{ij} c^{\dagger}_{i\sigma} c_{j\sigma}\ , \qquad (3.62) \end{aligned}$$

where we defined the t_{ij} in the last line as

$$t_{ij} \equiv \frac{1}{N}\sum_{\vec{k}}^{BZ} \frac{\hbar^2|\vec{k}|^2}{2m} \mathrm{e}^{\mathrm{i}\vec{k}\cdot(\vec{R}_i-\vec{R}_j)}\ . \qquad (3.63)$$

Thus, t_{ij} is the hopping matrix element associated with a Bloch electron hopping from site i to j. It vanishes exponentially with the increasing distance between the two sites. It actually reflects the atomic orbital overlap strength. Considering the atomic orbital wave functions instead of Bloch states leads us to a more realistic picture. Then, we can use the tight-binding hopping integral, $-t$, that results from the kinetic exchange mechanism and defined in Eq.(2.56), in place of the t_{ij}. In fact, as we stated in the beginning of this section, tight-binding approximation assumes strongly localized electrons, thus, one cannot expect a long range hopping contribute considerably within this approach. Hence, restricting ourselves justly to the nearest-neighbor hopping only, we can write the kinetic energy operator as

$$T = -t\sum_{\langle ij\rangle}\sum_{\sigma}\left(c^{\dagger}_{i\sigma}c_{j\sigma} + c^{\dagger}_{j\sigma}c_{i\sigma}\right)\ , \qquad (3.64)$$

where $\langle ij\rangle$ denotes that the sum is over nearest-neighbors. The addition of the second term in the sum is to ensure Hermiticity. We remember this operator from

the first chapter where we introduced the Hubbard model. The kinetic energy operator given above is in fact the first term in the Hubbard model [*cf.* Eq.(2.57)].

3.4.4 On-site Coulomb repulsion

Using the same arguments as in the previous subsection and the general form of the Coulomb interaction operator given in the second quantization formalism of Eq.(3.54), we briefly arrive

$$V = \sum_{i,j,k,\ell} \sum_{\sigma\sigma'} U_{ijk\ell} c^{\dagger}_{i\sigma} c^{\dagger}_{j\sigma'} c_{k\sigma} c_{\ell\sigma'} \ , \tag{3.65}$$

where $U_{ijk\ell}$ is defined as

$$U_{ijk\ell} \equiv \int d\vec{r} \int d\vec{r}\,' \, \phi^{*}_{i}(\vec{r}\,) \, \phi^{*}_{j}(\vec{r}\,') \, \frac{e^2}{|\vec{r} - \vec{r}\,'|} \, \phi_k(\vec{r}\,) \, \phi_\ell(\vec{r}\,') \ . \tag{3.66}$$

Now, if we limit our consideration on the on-site Coulomb repulsions between the electrons on the same atomic orbital and neglect any other possible Coulomb interactions we can write

$$V = \sum_{i} U_{iiii} \sum_{\sigma\sigma'} c^{\dagger}_{i\sigma} c^{\dagger}_{i\sigma'} c_{i\sigma} c_{i\sigma'} \ , \tag{3.67}$$

where we immediately realize that the U_{iiii} must be constant due to the spatial uniformity of the lattice, and in fact, this constant is nothing but the Hubbard U, defined in Eq.(2.54). Furthermore, we can assert that

$$\sum_{\sigma\sigma'} c^{\dagger}_{i\sigma} c^{\dagger}_{i\sigma'} c_{i\sigma} c_{i\sigma'} = 2 \hat{n}_{i\uparrow} \hat{n}_{i\downarrow}, \tag{3.68}$$

due to the Pauli exclusion principle. Inserting the constant factor 2 inside the Hubbard U we obtain

$$V = U \sum_{i} \hat{n}_{i\uparrow} \hat{n}_{i\downarrow} \ , \tag{3.69}$$

which is the second term of the Hubbard model of Eq.(2.57).

3.4.5 Epilogue

Let us now analyze what each term in the Hubbard Hamiltonian is for. The full Hamiltonian is given by

$$\mathscr{H} = -t \sum_{\langle ij \rangle} \sum_{\sigma} \left(c^{\dagger}_{i\sigma} c_{j\sigma} + c^{\dagger}_{j\sigma} c_{i\sigma} \right) + U \sum_{i} n_{i\uparrow} n_{i\downarrow} \, . \tag{3.70}$$

The first term is the kinetic energy contribution. It annihilates a spin-σ electron at a lattice site j and creates it at a nearest-neighboring lattice site i (and *vice versa*). Due to Pauli exclusion principle, given in Eq.(3.38), if there is no spin-σ electron at the jth lattice site or if there is already a spin-σ electron at the ith lattice site, the kinetic energy operator will immediately destroy the state it acts on, and that will yield zero gain to the energy, otherwise the energy of the system is lowered by t. The second term is the on-site Coulomb repulsion. The operator $n_{i\uparrow} n_{i\downarrow}$ leads to a nonvanishing state if and only if the lattice site i contains both a spin-$\uparrow$ and a spin-$\downarrow$ electron, in which case, there will be a energy cost of U.

Thus, Hubbard model implements the competition between the on-site Coulomb repulsion and the tight-binding hopping integral. In the limit of a small t/U, which is associated with a large lattice spacing, the electrons will usually localize on the atomic orbitals with a marginal contribution to conductivity, since the energy cost of finding two electrons on a single lattice site will overwhelm the energy gain due to hopping. As the lattice spacing decreases, the tight-binding hopping integral increases and this will eventually yield electrons to overcome the Coulomb repulsion penalty by delocalizing from atomic orbitals, becoming itinerant, and contributing to the conductivity. Hence, one expects a transition between the two regimes.

Let us note that in spite of the long history of the Hubbard model, we still lack rigorous results, in particular for $d > 1$ dimensions. In the next chapter, we will introduce the "*renormalization-group theory*", which provides the utmost efficient theoretical tools to investigate statistical physics of many-body sytems, and in particular to analyze phase transitions. Afterwards, we will introduce a simpler quantum electronic model, that is derived from the Hubbard Hamiltonian, namely the "*spinless Falicov-Kimball model*", which captures the essential physics of transition metal-oxides in particular.

Chapter 4

RENORMALIZATION-GROUP (RG) THEORY

4.1 Partition function

The main motivation of statistical mechanics is to derive the macroscopic behavior of a system from the microscopic interactions between the constituents which form up that system. For one of the simplest cases, namely the ideal gas, these microscopic interactions are the ones between the gas molecules and the reservoir walls that occur during any collision. The thermodynamics of this system, *i.e.*, the ideal gas law of $PV = Nk_BT$, is obtained by accounting these molecule–wall collision interactions.

The name of the field "*statistical mechanics*" is attributed for its probabilistic approach. Each possible microscopic state of a system, α, is associated with a probability proportional to the exponential of that state's energy, E_α, scaled by thermal energy, k_BT:

$$prob_\alpha \propto \mathrm{e}^{-E_\alpha/k_BT} \ , \tag{4.1}$$

where k_B is the Boltzmann constant ($k_B = 1.3806503 \times 10^{-23}$ m^2 kg s^{-2} K^{-1}) and T is the temperature in Kelvins. This exponential function is known as "*Boltzmann weight*" or "*Boltzmann factor*" and in order to properly normalize this propability function, we must divide the right-hand side by the summation of Boltzmann weights over all possible microstates:

$$prob_\alpha = \frac{\mathrm{e}^{-E_\alpha/k_BT}}{\sum_\alpha \mathrm{e}^{-E_\alpha/k_BT}} \ . \tag{4.2}$$

This normalization factor, the summation in the denominator, is a key element of statistical mechanics. This infinite summation over all possible degrees of freedom establishes the link between the microscopic definition and the macroscopic behavior of a system. This summation, called the "*partition function*", basicly spans the whole phase space and adds up the Boltzmann weights of every point:

$$Z = \sum_\alpha \mathrm{e}^{-E_\alpha/k_BT} \ . \tag{4.3}$$

The whole set of macroscopic properties of the system defined by the microscopic interactions can be obtained by several operations on partition function.

Thus, the main aim of statistical mechanics is writing up a microscopic definition of a system that would be able to capture the macroscopic behavior and calculating the partition function associated with that microscopic definition. However, calculating the result of an infinite summation (or integration) is not always trivial. The celebrated renormalization-group (RG) theory established by K. G. Wilson in 1971 [99] opens up a genuine viewpoint in calculating the macroscopic behavior from the microscopic definition. The main idea of RG theory is to eliminate a portion of the degrees of freedom by summing over those and obtaining a new ("*renormalized*") partition function in the same form as the original ("*unrenormalized*") one. This ensures an identical partition function with new renormalized interaction strengths. In this way, the problem is reduced to finding these renormalized interactions in terms of the unrenormalized ones, which can be solved easily and exactly, especially for 1-dimensional classical systems. Approximation techniques come into play in order to deal with higher dimensions or with non-classical quantum systems.

4.2 RG theory for 1-dimensional classical systems

As an examplar system, let us apply the RG theory onto the spin-$\frac{1}{2}$ Ising model, which is a well-known classical model defined by the dimensionless Hamiltonian

$$-\beta\mathscr{H} = \sum_{\langle ij\rangle}\big[Js_is_j + G\big] \equiv \sum_{\langle ij\rangle}\big[-\beta\mathscr{H}_{i,j}\big]\ , \tag{4.4}$$

where $\beta = 1/k_BT$ is the inverse thermal energy, $\langle ij\rangle$ denotes summation over nearest-neighbor pairs of sites and s_i, for every site i, can take values $\pm\frac{1}{2}$. The additive constant G is generated by the RG transformation and is used in the calculation of thermodynamic functions. Its inclusion into the Hamiltonian does not affect the physics defined by the model, since its only effect is to shift the zero of the dimensionless energy levels by NG, that is a constant. We define $-\beta\mathscr{H}_{i,j} \equiv Js_is_j + G$ as the Hamiltonian involving the bond between sites i and j.

Note that, the Ising model Hamiltonian is, in fact, a classical approximation to the Heisenberg–Dirac Hamiltonian (referred commonly as "*Heisenberg model*") introduced in Eq.(2.29). If one assumes that the exchange coupling is nonzero only for the spin-z components of the nearest-neighbors, the quantum mechanical Heisenberg model reduces to the classical Ising model given above. Further, note that the inverse temperature, β, is annexed into the exchange coupling, so that the interaction constant J is dimensionless.

The partition function for the system is given by

$$\begin{aligned} Z &= \sum_{\{s\}} \mathrm{e}^{-\beta\mathscr{H}(\{s\})} \\ &= \sum_{s_1}\sum_{s_2}\sum_{s_3}\cdots\sum_{s_i}\sum_{s_j}\sum_{s_k}\cdots\sum_{s_N} \mathrm{e}^{-\beta\mathscr{H}_{1,2}-\beta\mathscr{H}_{2,3}\cdots-\beta\mathscr{H}_{i,j}-\beta\mathscr{H}_{j,k}\cdots-\beta\mathscr{H}_{N,1}}\ , \end{aligned} \tag{4.5}$$

where i, j, k are three successive lattice sites. Performing this infinite series of sums and obtaining Z (and thus obtaining the thermodynamics) may be seen as impossible, however RG transformation opens up the possibility. First of all, we will perform the summation over one variable, *i.e.*, s_j . The only part of the exponentiated Hamiltonian including s_j is $\exp[-\beta\mathscr{H}_{ij} - \beta\mathscr{H}_{jk}]$, and the rest is constant with respect to s_j . Therefore, performing the sum over s_j yields

$$\begin{aligned}
\sum_{s_j=\pm 1/2} \mathrm{e}^{-\beta\mathscr{H}_{i,j}-\beta\mathscr{H}_{j,k}} &= \sum_{s_j=\pm 1/2} \mathrm{e}^{Js_is_j+G+Js_js_k+G} \\
&= \sum_{s_j=\pm 1/2} \mathrm{e}^{Js_j(s_i+s_k)+2G} \\
&= \mathrm{e}^{2G}\left[\mathrm{e}^{\frac{J}{2}(s_i+s_k)} + \mathrm{e}^{-\frac{J}{2}(s_i+s_k)}\right] \\
&\equiv \mathrm{e}^{J's_is_k+G'} \\
&= \mathrm{e}^{-\beta'\mathscr{H}'_{j,k}} \ , \qquad (4.6)
\end{aligned}$$

where we have redefined the result of the sum as a transformed dimensionless Hamiltonian. Here, and for the rest of this dissertation, the primes are used for the renormalized system. From the third and fourth lines of Eq.(4.6), one can derive the renormalized interaction constants with respect to unrenormalized ones. First we must consider that the definition must hold for all possible s_i and s_k values.

$$s_i = +\tfrac{1}{2} \ , \quad s_k = +\tfrac{1}{2} \ : \quad \mathrm{e}^{2G}\left[\mathrm{e}^{\frac{J}{2}} + \mathrm{e}^{-\frac{J}{2}}\right] = \mathrm{e}^{G'+\frac{J'}{4}} \ , \qquad (4.7)$$

$$s_i = -\tfrac{1}{2} \ , \quad s_k = +\tfrac{1}{2} \ : \quad 2\mathrm{e}^{2G} = \mathrm{e}^{G'-\frac{J'}{4}} \ , \qquad (4.8)$$

$$s_i = -\tfrac{1}{2} \ , \quad s_k = -\tfrac{1}{2} \ : \quad \mathrm{e}^{2G}\left[\mathrm{e}^{-\frac{J}{2}} + \mathrm{e}^{\frac{J}{2}}\right] = \mathrm{e}^{G'+\frac{J'}{4}} \ , \qquad (4.9)$$

$$s_i = +\tfrac{1}{2} \ , \quad s_k = -\tfrac{1}{2} \ : \quad 2\mathrm{e}^{2G} = \mathrm{e}^{G'-\frac{J'}{4}} \ . \qquad (4.10)$$

Now we see that Eqs.(4.7, 4.8) are identical to Eqs.(4.9, 4.10). Thus, we have a set of two equations and two unknowns, *i.e.*, G' and J', to solve. Multiplication and division of these equations [either Eqs.(4.7, 4.8) or Eqs.(4.9, 4.10)] respectively gives the equations set of

$$\begin{aligned}
4\mathrm{e}^{4G}\cosh\left(\tfrac{J}{2}\right) &= \mathrm{e}^{2G'} \ , \\
2\cosh\left(\tfrac{J}{2}\right) &= \mathrm{e}^{\frac{J'}{2}} \ , \qquad (4.11)
\end{aligned}$$

which can be easily solved by taking logarithms to find

$$\begin{aligned}
G' &= 2G + \tfrac{1}{2}\ln\left[4\cosh\left(\tfrac{J}{2}\right)\right] \ , \\
J' &= 2\ln\left[2\cosh\left(\tfrac{J}{2}\right)\right] \ . \qquad (4.12)
\end{aligned}$$

After applying the same procedure for every even lattice site, the partition function from Eq.(4.5) takes the renormalized form

$$Z = \sum_{s_1}\sum_{s_3}\cdots\sum_{s_i}\sum_{s_k}\sum_{s_{N-1}} \mathrm{e}^{-\beta'\mathscr{H}'_{1,3}\cdots-\beta'\mathscr{H}'_{i,k}-\beta'\mathscr{H}'_{N-1,1}} \equiv Z' \ . \tag{4.13}$$

In the thermodynamic limit of $N \to \infty$, this form of the partition function is identical with the unrenormalized one, although we have eliminated half of the degrees of freedom. One can fairly exploit this identity in order to derive the thermodynamics as will be seen in a section below, when we discuss the calculation of densities.

What we actually did here is that, we rescaled the system by a factor of 2 by integrating over half of the spins, and redefined the interactions in this new system in order to make the new Hamiltonian in the same form as the original one, thus keep the partition function invariant. This choice of the rescaling is arbitrary. We would have chosen the rescaling factor as 3 as well. In general this "*rescaling factor*" is denoted by b (*cf.* Fig. 4.1).

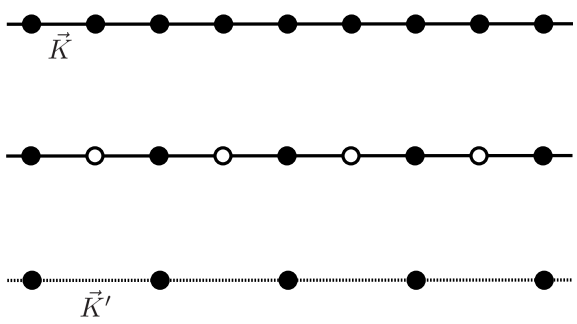

Figure 4.1: Rescaling of a 1-dimensional sytem under RG transformation. Every other degree of freedom (denoted by open circles) is traced out in the partition function and the system is rescaled with a factor of $b = 2$. The nearest neighboring spins interact with $\vec{K} = [G, J]^T$ (denoted by full lines) in the original system and with $\vec{K}' = [G', J']^T$ (denoted by dotted lines) in the renormalized rescaled system. This procedure preserves the partition function while decreasing the number of degrees of freedom — to be integrated over — by a factor of $b = 2$. The choice of the rescaling factor, b, is arbitrary. One could have equivalently solve the problem with any b.

The solutions for the renormalized interactions in terms of the unrenormalized ones given above in Eq.(4.12) are called "*recursion relations*" in general. One can start with a renormalized system and obtain a second renormalized one with interactions G'' and J''. This procedure can continue *ad infinitum*, but the form of the recursion relations is invariant at each step. Thus, for the second renormalization, the recursion relations read

$$\begin{aligned} G'' &= 2G' + \tfrac{1}{2}\ln\left[4\cosh\left(\tfrac{J'}{2}\right)\right] , \\ J'' &= 2\ln\left[2\cosh\left(\tfrac{J'}{2}\right)\right] , \end{aligned} \tag{4.14}$$

where G' and J' are already given in Eq.(4.12) in terms of G and J. In general, for the nth renormalization step we write

$$\begin{aligned} G^{(n)} &= 2G^{(n-1)} + \tfrac{1}{2}\ln\left[4\cosh\left(\tfrac{1}{2}J^{(n-1)}\right)\right] , \\ J^{(n)} &= 2\ln\left[2\cosh\left(\tfrac{1}{2}J^{(n-1)}\right)\right] . \end{aligned} \tag{4.15}$$

Here, let us discuss the significance of the interaction constant G. In fact, we added the G term into the ordinary Ising Hamiltonian, given by Eq.(4.4), in order to be able to solve the problem. Unless we added this G term, we would have two independent equations but only one unknown to solve, which is mathematically impossible to yield a result. However, the only effect of the addition of a constant term for every bond is to shift the dimensionless energy spectrum of the system by a constant (number of bonds times G), which in the end, do not alter the thermodynamics of the system. This constant addition to the Hamiltonian is necessary for all systems, even for the simplest ones like the spin-$\frac{1}{2}$ Ising model we consider here. This interaction constant G is called "*additive constant*" or "*captive variable*" and is important particularly in calculating the Helmholtz free energy of the system.

The addition of the captive variable can be better regarded as follows: The RG transformation is indeed a mapping in the Hamiltonan interactions space, that is one-dimensional in the case of the original Ising model, with J being the only

interaction parameter. However, the RG transformation maps a point in this J-space onto a point in a higher-dimensional interactions space, *i.e.*, (G, J)-space. Thus, in order to ensure the RG transformation to be a closed one, we must redifine the Hamiltonian with a captive variable.

In cases of more complicated system Hamiltonians, *e.g.*, quantum systems, addition of many other dimensions may be necessary. The number of independent equations for recursion relations determines the necessary number of variables to solve, thus the dimensionality of the Hamiltonian interactions space (thermodynamic field space) in which the RG transformation is closed.

Lastly, we should mention that the two of the properties of the recursion relations above are quite general for all RG transformations: Firstly, the partial derivative $\partial_G G' = 2$. In general,

$$\partial_G G' = b^d \ , \tag{4.16}$$

where b is the rescaling factor and d is the dimensionality of the lattice. (The case we considered above implements $b = 2$ in $d = 1$, hence $b^d = 2$.) The relation $\partial_G G' = b^d$ holds for every system, since G is just an additive constant acting uniformly on all bonds, *i.e.*, it does not involve any microscopic state of the system, unlike the J-term, which comes with the multiplication of nearest-neighbor degrees of freedom for example. Secondly, the partial derivative $\partial_G J' = 0$. In general all recursion relations other than the one for G' are independent of G. Thus,

$$\partial_G K' = 0 \quad \text{for} \quad K \neq G \ , \tag{4.17}$$

which reflects the fact that the addition of a captive variable does not affect the physics of the modelled system in general. The derivatives of renormalized interaction variables with respect to unrenormalized ones form the "*recursion matrix*" which has a key role in calculating thermodynamic densities as will be discussed in a following section.

4.3 RG theory for 1-dimensional quantum systems

Performing the sum over a single degree of freedom in Eq.(4.6) and entering the result back into the partition function of Eq.(4.5) is impossible in quantum sytems, since the degrees of freedom are not represented by simple numbers anymore, but by operators that usually do not commute with each other over neighboring lattice sites. In fact, it is this non-commutativity of the operators that makes the difference between classical and quantum systems.

For a model system to be non-trivial, some interaction must be present between different constituents that form up the system including the external fields. As an example, let us consider the spin-$\frac{1}{2}$ quantum Heisenberg model, one of the simplest yet non-trivial quantum models, resulting from the direct exchange mechanism and defined by the dimensionless Hamiltonian operator [*cf.* Eq.(2.29)],

$$\begin{aligned} -\widehat{\beta\mathscr{H}} &= \sum_{\langle ij\rangle}\Big[J\widehat{s_i}\cdot\widehat{s_j}+G\widehat{I}\Big] \\ &= \sum_{\langle ij\rangle}\Big[J\big(\widehat{s_i^x}\widehat{s_j^x}+\widehat{s_i^y}\widehat{s_j^y}+\widehat{s_i^z}\widehat{s_j^z}\big)+G\widehat{I}\Big] \\ &\equiv \sum_{i}\Big[-\widehat{\beta\mathscr{H}}_{i,i+1}\Big]\,, \end{aligned} \tag{4.18}$$

which acts on the spin-configuration-space, $\bigotimes_{i=1}^{N}\mathbb{C}^2$, in which a ket is denoted by $|m_1^z,m_2^z,\cdots,m_N^z\rangle\equiv|\{m_i^z\}\rangle$, with $m_i^z=\pm\frac{1}{2}$ being an eigenvalue of $\widehat{s_i^z}$, unlike the scalar spin values of the classical Ising model. We use the hat notation for the quantum mechanical operators in order to avoid a confusion with the scalar variables. Here, $\widehat{I}$ is the identity operator and $-\widehat{\beta\mathscr{H}}_{i,i+1}$ is the two-site Hamiltonian operator, both acting on a bond configuration ket $|m_i^z,m_{i+1}^z\rangle$, and the operators $\widehat{s_i^u}$ for $u=x,y,z$ are the usual quantum mechanical Pauli spin operators at site i. These Pauli spin operators obey the well-known commutation rules of

$$\Big[\widehat{s_i^u},\widehat{s_j^v}\Big]=2\mathrm{i}\delta_{ij}\epsilon_{uvw}\hat{s}_i^w\,, \tag{4.19}$$

where δ_{ij} is the Kronecker delta and ϵ_{uvw} denotes the usual cyclic Levi-Civita symbol.

The partition function is again given by a trace over the whole configuration space as

$$Z = \sum_{\{m_i^z\}} \langle \{m_i^z\} | \mathrm{e}^{-\beta \widehat{\mathscr{H}}} | \{m_i^z\} \rangle = \sum_{m_1^z} \cdots \sum_{m_i^z} \sum_{m_{i+1}^z} \sum_{m_{i+2}^z} \cdots \sum_{m_N^z} \tag{4.20}$$
$$\langle m_1^z, \cdots, m_N^z | \mathrm{e}^{-\beta \widehat{\mathscr{H}}_{1,2} \cdots - \beta \widehat{\mathscr{H}}_{i,i+1} - \beta \widehat{\mathscr{H}}_{i+1,i+2} \cdots - \beta \widehat{\mathscr{H}}_{N,1}} | m_1^z, \cdots, m_N^z \rangle \ .$$

For a moment, for the sake of simplicity, let us forget about the act of exponentiation on operators and assume that we could write the exponential of a sum of operators as a product of exponentiated operators, as we could do in classical limit. If we are to single out a sum, *e.g.*, over m_{i+1}^z, as we did in the previous subsection, we have to take the exponentiated $-\beta \mathscr{H}_{i,i+1} - \beta \mathscr{H}_{i+1,i+2}$ operator out of the grand sum to the very left. In the very first step of this procedure, we have to switch the position of this operator with the position of the previous one, *i.e.*, the one containing $-\beta \mathscr{H}_{i-1,i}$. This operation involves commutators between the operators $\widehat{s_i^x}$, $\widehat{s_i^y}$ and $\widehat{s_i^z}$, since these operators also appear in the $-\beta \mathscr{H}_{i-1,i}$ term. After this step, we do not need to consider the non-commutativity anymore, since $-\beta \mathscr{H}_{i,i+1} - \beta \mathscr{H}_{i+1,i+2}$ always commutes with $-\beta \mathscr{H}_{j,j+1}$ for $j < i-1$. A similar symmetric operation of moving the concerned operator to the very right also involves commutators at the first step. Thus, in calculating single traces over every other lattice site i we have to consider the non-commutativity of the Pauli spin operators at the neighboring sites. The situation is the same but everted when we are to put the result of the single sum back into its original position in the partition function.

To summarize, for a quantum system, in order to perform an absolutely straightforward RG transformation in a fashion as described in the previous section, we have to ignore the non-commutativity of the operators in the Hamiltonian in two steps:

(i) while singling out a sum over a degree of freedom that is involved in some part of the exponentiated Hamiltonian,

(ii) while putting the result of the single sum (in an exponentiated renormalized Hamiltonian form) back into its original position in the partition function.

The effects of the ignorance of the non-commutativity in the two opposite steps described above may however mutually compensate each other. Indeed, ignoring this non-commutativity in both steps (i) and (ii) yields an approximate method, which was first introduced by Suzuki and Takano for anisotropic XY and Heisenberg systems [100, 101]. For a 1-dimensional quantum system Hamiltonian that can be given by

$$-\beta\mathscr{H} = \sum_i \left[-\beta\mathscr{H}_{i,i+1} \right] , \tag{4.21}$$

the RG procedure, which eliminates half of the degrees of freedom and keeps the partition function unchanged, is done approximately as

$$\begin{aligned} \mathrm{Tr}_{\mathrm{odd}} \mathrm{e}^{-\beta\mathscr{H}} &= \mathrm{Tr}_{\mathrm{odd}} \mathrm{e}^{\sum_i [-\beta\mathscr{H}_{i,i+1}]} \\ &= \mathrm{Tr}_{\mathrm{odd}} \mathrm{e}^{\sum_i^{\mathrm{odd}} [-\beta\mathscr{H}_{i-1,i} - \beta\mathscr{H}_{i,i+1}]} \\ &\simeq \prod_i^{\mathrm{odd}} \mathrm{Tr}_i \mathrm{e}^{[-\beta\mathscr{H}_{i-1,i} - \beta\mathscr{H}_{i,i+1}]} \\ &= \prod_i^{\mathrm{odd}} \mathrm{e}^{-\beta'\mathscr{H}'_{i-1,i+1}} \\ &\simeq \mathrm{e}^{\sum_i^{\mathrm{odd}} -\beta'\mathscr{H}'_{i-1,i+1}} = \mathrm{e}^{-\beta'\mathscr{H}'} . \end{aligned} \tag{4.22}$$

In this more direct mathematical form, the steps (i) and (ii) described above are much clearer. In step (i), which corresponds to the first $\simeq$ in Eq.(4.22), we write an exponential of a sum as a product of exponentials; and in step (ii), corresponding to the second $\simeq$ in Eq.(4.22), we convert a product of exponentials into an exponential of a sum. Thus, at each successive length scale, we ignore the non-commutativity of the operators beyond three consecutive sites, in the two steps indicated by $\simeq$ in the above equation. Since the approximations are applied in opposite directions, one can expect some mutual compensation. Earlier studies [100, 101, 102, 103, 104, 105, 106, 107, 108, 109, 110, 111] have been successful in obtaining finite-temperature behavior on a variety of quantum systems, including both spin and electronic systems. For the approximation of fractal decomposition of exponentiated quantum mechanical operators in general and for the application of this approximation on Monte Carlo simulations, one should be referred to [112].

4.4 Generalization to higher dimensions

Recursion relations of 1-dimensional models, either classical or quantum mechanical, are in the form

$$\overrightarrow{K}' = R_1(\overrightarrow{K}) \ , \tag{4.23}$$

where $\overrightarrow{K}$ and $\overrightarrow{K}'$ are the original and renormalized interaction parameters of the model, *e.g.*, $\overrightarrow{K} = [G, J]^T$ and $\overrightarrow{K}' = [G', J']^T$ for the Ising or the Heisenberg model.

The Migdal–Kadanoff procedure [113, 114] for generalization of the recursion relations in 1-dimension, $R_1(\overrightarrow{K})$, to $R_d(\overrightarrow{K})$ for any $d > 1$ dimensions is described in two forms: (i) bond moving followed by 1-dimenional decimation, and (ii) *vice versa*. The first form is implemented by

$$\overrightarrow{K}' = R_d(\overrightarrow{K}) \simeq R_1(b^{d-1}\overrightarrow{K}) \ , \tag{4.24}$$

and the second form by

$$\overrightarrow{K}' = R_d(\overrightarrow{K}) \simeq b^{d-1} R_1(\overrightarrow{K}) \ . \tag{4.25}$$

The procedure can be best understood graphically. In Fig.4.2 below, we show a presentation of how the approximation described by Eq.(4.24), *i.e.*, bond moving followed by 1-dimensional decimation, proceeds for a hypercubic lattice of $d = 3$ and a rescaling factor of $b = 2$. Starting from the original system of plain simple cubic lattice of top left, at each step the bonds indicated by red are moved accordingly to obtain the next system. This corresponds to deleting the red bonds and, in order to obtain an effectively same system, doubling the strength of the bonds parallel to the deleted ones. Consider that the system size is in fact infinite, and only a portion of it is represented here. Double-strength bonds are indicated by double lines while quadruple-strength bonds are indicated by full green lines for the sake of graphical simplicity. In the last step, the mid-degrees of freedom are traced out in all 3-independent orthogonal directions, yielding the renormalized system rescaled by a factor of $b = 2$. Thus, in the end, the rescaled system must have renormalized interactions shown by dashed green lines of strength $\overrightarrow{K}' \simeq R_1(4\overrightarrow{K})$ which is in accord with Eq.(4.24).

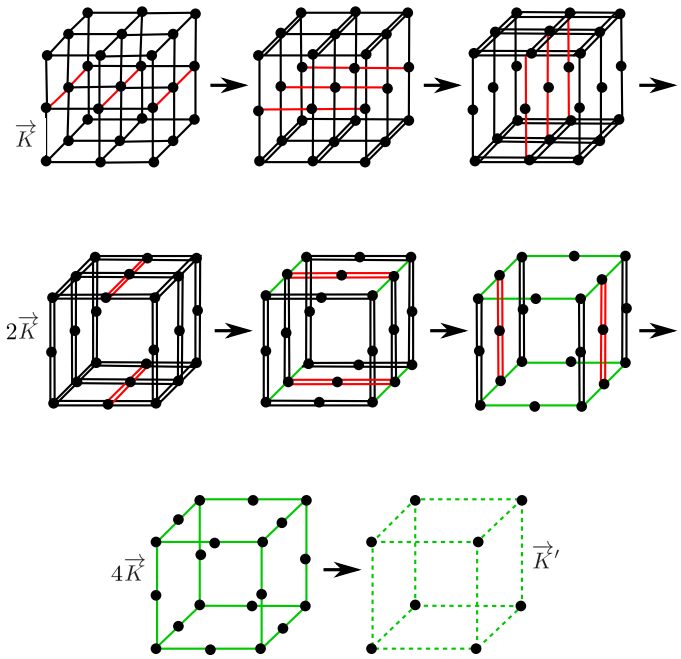

Figure 4.2: A graphical representation of the Migdal–Kadanoff procedure of bond moving followed by 1-dimensional decimation for a simple cubic lattice and a rescaling factor of $b = 2$. Moved bonds at each step are indicated by red lines while double- and quadruple-strength bonds are indicated by double lines and full green lines respectively. Renormalized quadruple-strength bonds are shown by dashed green lines.

Practical implementation of the second form of the Migdal–Kadanoff procedure given by Eq.(4.25) is simpler in computational aspects, hence we choose to use the second form. This second procedure is equivalent to the first one with the only difference being in the order of operations: in the second procedure, 1-dimenional decimation is followed by bond moving.

When we implement one of the formulations, either given by Eq.(4.24) or Eq.(4.25), the dimensionality, d, becomes just a parameter which is not necessarily to be an integer anymore. This means that one can work with any fractal dimensional lattice by using the Migdal–Kadanoff procedure. The best application would be in studying lower-critical dimensions, since one can approach the lower-critical dimension arbitrarily closely from both sides by assigning $d = 1.999$, *etc.*

Lastly, we should mention that the Migdal–Kadanoff technique is exact for d-dimensional hierarchical lattices [115, 116, 117] and a very good approximation for hypercubic lattices.

4.5 Calculation of densities

A non-trivial model Hamiltonian is defined by different interactions that are associated with interaction constants for every different type of interaction. Let us consider a representative Hamiltonian given by

$$-\beta\mathscr{H} \equiv \sum_i [-\beta\mathscr{H}_i] \ , \tag{4.26}$$

where $-\beta\mathscr{H}_i$ is the local Hamiltonian involving only the degrees of freedom at site i. For simplicity, let us consider the case when there exists only one type of degree of freedom associated with each site i that is denoted by s_i. (The situation can be well generalized to the case of more than one degree of freedom per site.) In general, the system involves different types of interactions and the local Hamiltonian is given by

$$-\beta\mathscr{H}_i \equiv \sum_\alpha (K_\alpha p_{i\alpha}) \ , \tag{4.27}$$

where $p_{i\alpha}$ reflects the local α-type interactions for site i. In example, in the case of 1-dimensional Ising model, there are two types of interactions: (i) additive interaction with $K_1 = G$ and $p_{i1} = 1$; and (ii) nearest-neighbor spin-spin interaction with $K_2 = J$ and $p_{i2} = s_i s_{i+1}$. We can introduce several different types of interactions into the model in order to capture the thermodynamic properties of the modelled system, *e.g.*, next-nearest-neighbor interactions, on-site interactions, *etc.* Since we must always consider an additive interaction for RG formulation, p_{i1} is always taken as 1 with $K_1 = G$. For the rest of the interactions ($\alpha > 1$), in general, the local α-type interactions for site i are given by

$$p_{i\alpha} = s_i \prod_{j\in\alpha} s_j \ . \tag{4.28}$$

with s_i denoting the local microscopic degree of freedom at site i, and the product being over the sites interacting with this site.

For every α-type interaction in the Hamiltonian, K_α, we can define a conjugate density as

$$
\begin{aligned}
M_\alpha &\equiv \frac{1}{N}\sum_i \langle p_{i\alpha}\rangle \\
&= \frac{1}{N}\sum_i \left[\frac{1}{Z}\sum_{\{s_j\}}\left(p_{i\alpha}\mathrm{e}^{-\beta\mathscr{H}}\right)\right] \\
&= \frac{1}{N}\frac{1}{Z}\sum_{\{s_j\}}\left[\left(\sum_i p_{i\alpha}\right)\mathrm{e}^{\sum_i\sum_\gamma K_\gamma p_{i\gamma}}\right] \\
&= \frac{1}{Z}\sum_{\{s_j\}}\left[p_{i\alpha}\mathrm{e}^{\sum_i\sum_\gamma K_\gamma p_{i\gamma}}\right] \\
&= \frac{1}{N_\alpha}\frac{\partial \ln Z}{\partial K_\alpha} = M_\alpha \ , \qquad (4.29)
\end{aligned}
$$

where, in writing the fourth line, we used the spatial uniformity of the system, namely the assuption of M_α being the same for each lattice site. Here, N is the total number of sites and N_α is the number of α-type interactions. For N_α, in general, one can write

$$N_\alpha \equiv N q_\alpha \ . \qquad (4.30)$$

Here, the factor N reflects the number of translations in obtaining N_α, while q_α involves other operations, *e.g.*, rotations, reflections, *etc.* In a proper RG transformation operation, the symmetries of the system is conserved with the only change being in the number of degrees of freedom, that is decimated by the relation

$$N' = \frac{N}{b^d} \ , \qquad (4.31)$$

since every length scale is rescaled by a factor of b in all d dimensions. Thus, q_α must stay invariant after an RG transformation, *e.g.*, nearest-neighbor interactions must stay as nearest-neighbor interactions but with neighboring bond length increasing from a to ba, like all other length scales defined for the system.

Just as the interaction constants vector, $\overrightarrow{K}$, of two consecutive points along the RG trajectory are related by the recursion relations, the densities vector, $\overleftarrow{M} = [\{M_\alpha\}]$, are connected by a "*recursion matrix*", $\overleftrightarrow{T}$, which is composed of derivatives of the recursion relations given by

$$T_{\gamma\alpha} = \frac{N_\gamma}{N_\alpha}\frac{\partial K'_\gamma}{\partial K_\alpha} \ . \tag{4.32}$$

We can obtain [118] this connection between $\overleftarrow{M'}$ and $\overleftarrow{M}$ starting by Eq.(4.29):

$$\begin{aligned} M_\alpha &= \frac{1}{N_\alpha}\frac{\partial \ln Z}{\partial K_\alpha} \\ &= \frac{1}{N q_\alpha}\frac{\partial \ln Z}{\partial K_\alpha} \\ &= \frac{1}{b^d N' q_\alpha}\frac{\partial \ln Z}{\partial K_\alpha} \\ &= b^{-d}\frac{N}{N'}\frac{q_\gamma}{q_\alpha}\frac{1}{N' q_\gamma}\frac{\partial \ln Z}{\partial K_\alpha} \\ &= b^{-d}\frac{N_\gamma}{N_\alpha}\left(\frac{1}{N'_\gamma}\frac{\partial \ln Z'}{\partial K'_\gamma}\right)\frac{\partial K'_\gamma}{\partial K_\alpha} \\ &= b^{-d}\ M'_\gamma T_{\gamma\alpha} = M_\alpha \ , \end{aligned} \tag{4.33}$$

where $T_{\gamma\alpha}$ is the recursion matrix element defined in Eq.(4.32) and the parenthetic term equals to M'_γ in accord with the definition of Eq.(4.29). Here, in the fifth line, we used a chain rule to change the derivation operation being with respect to K_α into the one with respect to K'_γ. Also in this step, we used the equivalance of the original and renormalized partition functions, *i.e.*, $Z = Z'$. As mentioned previously [*cf.* Eq.(4.13)], the partition function for the system can be expressed both by the unrenormalized interaction constants as $Z = Z\left(\overrightarrow{K}\right)$ or by the renormalized interaction constants as $Z' = Z\left(\overrightarrow{K'}\right)$ in the thermodynamic limit of $N \to \infty$. By using these two equivalent forms, one can formulate the density recursion relations as

$$M_\alpha = b^{-d}\sum_\gamma M'_\gamma T_{\gamma\alpha} \tag{4.34}$$

or in the simpler vector notation as [118]

$$b^d\overleftarrow{M} = \overleftarrow{M'}\cdot\overleftrightarrow{T} \ . \tag{4.35}$$

In example, for the 1-dimensional Ising Hamiltonian, the interaction constants vector, the density vector, and the recursion matrix are

$$\begin{aligned}
\overrightarrow{K} &= [G, J]^T \ , \\
\overleftarrow{M} &= [1, \langle s_i s_{i+1} \rangle] \ , \\
\overleftrightarrow{T} &= \begin{bmatrix} \partial_G G' = b^d & \partial_J G' \\ \partial_G J' = 0 & \partial_J J' \end{bmatrix} \ .
\end{aligned} \tag{4.36}$$

Note that, since both interactions are defined on nearest-neighboring bonds, $N_G/N_J = N_J/N_G = 1$, allowing us to drop the ratio of interaction numbers terms in the recursion matrix. This is particularly important in practice. Indeed, we defined the additive interaction over the bonds, as opposed to the widely studied version of defining the additive term over the sites, in order to be able to drop the N_γ/N_α terms in $T_{\gamma\alpha}$. We give a generalization of the situation as follows.

For any clasical or quantum mechanical Hamiltonian involving both bond and on-site interactions given by

$$-\beta\mathscr{H} = \overline{K}_{bond} \sum_{\langle ij \rangle} s_{ij} + \mathring{K}_{site} \sum_i s_i \ , \tag{4.37}$$

where s_{ij} and s_i represent bond and site degrees of freedom respectively, we can redefine the Hamiltonian as

$$\begin{aligned}
-\beta\mathscr{H} &\equiv \overline{K}_{bond} \sum_{\langle ij \rangle} s_{ij} \ + \overline{K}_{site} \sum_{\langle ij \rangle} (s_i + s_j) \\
&= \sum_{\langle ij \rangle} \left[\overline{K}_{bond}\, s_{ij} + \overline{K}_{site}\, (s_i + s_j) \right] \\
&\equiv \sum_{\langle ij \rangle} \left[-\beta\mathscr{H}_{i,j} \right] \ .
\end{aligned} \tag{4.38}$$

Here, for a d-dimensional hypercubic lattice, since every site has $2d$ nearest-neighbors, the redefined on-site interaction is related to the original one by

$$\overline{K}_{site} = \frac{\mathring{K}_{site}}{2d} \ . \tag{4.39}$$

With this new definition of the on-site interaction constant, which leads to the new Hamiltonian purely equivalent to the original one, we can drop the N_{site}/N_{bond} and N_{bond}/N_{site} terms in the off-diagonal elements of the recursion matrix. It is

obvious that, in general, for interactions that involve beyond the nearest-neighbor interactions, we can reform a given model Hamiltonian into an appropriate form, for which the interaction number ratios in the recursion matrix can be omitted. Now, let us continue our discussion on calculating the densities.

The space of whose dimensions are assigned to the interaction constants appearing in the Hamiltonian is called the "*Hamiltonian space*" or "*thermodynamic field space*". An RG transformation over a Hamiltonian maps a $\overrightarrow{K}$ point to another $\overrightarrow{K}'$ in the Hamiltonian space. These mappings form "*RG flows*" in the thermodynamic field space; and the relations between the properties of these RG flows and physical behavior of the system will be examined in the next section. For now, in order to complete our discussion on calculation of densities, we will mention about some special points in the Hamiltonian space.

The special points in the thermodynamic field space, where interaction constants stay the same under RG transformations, are called "*fixed points*". These particular points refer to either sinks — that are points of attractions for phase basins — or to critical, first-order or null fixed points that govern the properties of the phase boundaries.

Thus, at a fixed point of the thermodynamic field space, recursion relations for the interaction constants take a very simple form of

$$\overrightarrow{K}' = \overrightarrow{K} \equiv \overrightarrow{K}^* \ , \tag{4.40}$$

and as a result, the conjugate densities vector also posesses the same simple recursion relation at a fixed point, namely[1]

$$\overleftarrow{M}' = \overleftarrow{M} \equiv \overleftarrow{M}^* \ . \tag{4.41}$$

The invariance of interaction constants and densities at a fixed point makes the calculation of densities feasible at these special points. Using the fixed densities vector $\overleftarrow{M}^*$ in the recursion relation of Eq.(4.35) yields [118]

[1]The asterisk introduced here must not be confused with the complex conjugation. Here, we are working with the physically measurable interactions and densities that assume real values, and the asterisk is merely used to indicate fixed points.

$$\overleftarrow{M}^* \cdot \overleftrightarrow{T} = \overleftarrow{M}^* \cdot b^d \ . \tag{4.42}$$

This means that the fixed point densities are simply the components of the left eigenvector of the recursion matrix at the fixed point with left eigenvalue b^d. For a D_H-dimensional Hamiltonian space, the number of left eigenvectors of the recursion matrix is D_H, but at least one of them is associated with the left eigenvalue b^d, and the components of this eigenvector are the physical densities at the fixed point.

For ordinary points, that are not fixed points themselves but lie in the basin of attraction of some sink, Eq.(4.35) is iterated until an attractive fixed point is reached under successive RG transformations in order to obtain the densities at the ordinary point. We can derive the algebraic form of this method in the direction of RG flows. Starting from the original ordinary point, at each successive RG step we can use Eq.(4.35) to obtain

$$\begin{aligned}
\overleftarrow{M}^{(0)} &= b^{-d}\, \overleftarrow{M}^{(1)} \cdot \overleftrightarrow{T}^{(1)} \ , \\
\overleftarrow{M}^{(1)} &= b^{-d}\, \overleftarrow{M}^{(2)} \cdot \overleftrightarrow{T}^{(2)} \ , \\
&\vdots \\
\overleftarrow{M}^{(n-1)} &= b^{-d}\, \overleftarrow{M}^{(n)} \cdot \overleftrightarrow{T}^{(n)} \ ,
\end{aligned} \tag{4.43}$$

where $\overleftarrow{M}^{(i)}$ and $\overleftrightarrow{T}^{(i)}$ denote the densities vector and the recursion matrix at the ith RG transformation step, with $\overleftarrow{M}^{(0)}$ being the densities vector at the original ordinary point and $\overleftarrow{M}^{(n)} \approx \overleftarrow{M}^*$ at the sink, for which the value is known via Eq.(4.42). Now, staring from the last RG step of Eq.(4.43) and inserting the expression for $\overleftarrow{M}^{(i)}$ into the relation for $\overleftarrow{M}^{(i-1)}$ at each step in the opposite direction of the RG flow yields [118]

$$\overleftarrow{M}^{(0)} = b^{-nd} \cdot \overleftarrow{M}^{(n)} \cdot \overleftrightarrow{T}^{(n)} \cdot \overleftrightarrow{T}^{(n-1)} \cdot \ \ldots \ \cdot \overleftrightarrow{T}^{(1)} \ . \tag{4.44}$$

In practice, we use this algebraic form and perform an iteration over the number of successive RG transformations, n. We calculate the matrix product of recursion matrices, $\overleftrightarrow{T}^{(n)} \cdot \overleftrightarrow{T}^{(n-1)} \cdot \ \ldots \ \cdot \overleftrightarrow{T}^{(1)}$, and the densities vector saturate to a point as we increase n, thus the densities at the original point are found.

Densities are the basic thermodynamic functions associated with the model Hamiltonian. More complicated thermodynamic functions such as internal energy, free energy, entropy, enthalpy, specific heat, *etc.* can all be calculated globally at each point of the thermodynamic field space by using densities. As an example, let us once again consider the 1-dimensional Ising model defined by the Hamiltonian of Eq.(4.4). The dimensionless internal energy per bond (or equivalently per site) is given by

$$-\beta U = J\langle s_i s_{i+1}\rangle \ , \tag{4.45}$$

since the nearest-neighbor interaction is the only contribution to the Hamiltonian. We can ignore the additive G contribution per bond, since its only effect is to shift the zero of the energy levels that does not change the thermodynamics. We can as well set $G = 0$ for the original system but allow the points in the Hamiltonian space to flow in (G, J)-plane.

Remember that we added the G term to ensure the Hamiltonian to be closed under RG transformations. This means that even if we start at a point $\overrightarrow{K} = [G = 0, J]^T$, the RG transformation maps this point to $\overrightarrow{K}' = [G' \neq 0, J']^T$. However, we can always restrict the RG analysis for $G = 0$, calculating the thermodynamic properties only on this subspace. This is a conventional method in all RG theory calculations. Especially for more sophisticated quantum particulate systems, for which the dimensions of the thermodynamic field space of closed RG transformations may triple the original dimensions, or may extend even beyond. But the restriction on the number possible microstates that a site can assume also guarantees a minimum dimensions for the Hamiltonian space on which the RG transformations are closed. In example, the set of Eqs.(4.7-4.10) can consist at most 4-independent equations, since a pair (s_i, s_k) can assume one of 4-different configurations, $\{(+\frac{1}{2}, +\frac{1}{2}), (+\frac{1}{2}, -\frac{1}{2}), (-\frac{1}{2}, +\frac{1}{2}), (-\frac{1}{2}, -\frac{1}{2})\}$. Thus, a model Hamiltonian, that consists n-body interactions and spin-$\frac{m}{2}$ degrees of freedom at each site, can be closed under RG transformations in an $(m+1)^n$-dimensional thermodynamic field space.

Calculation of response functions, that are experimentally more feasible to measure, involves derivatives of the basic densities with respect to thermodynamic fields. In general, all thermodynamic fields, *e.g.*, external magnetic field, chemical potential, *etc.*, are explicity defined in the dimensionless Hamiltonian, except the temperature. Conventionally, the model Hamiltonian is defined in a dimensionless style by absorbing the thermal energy k_BT in all RG theory calculations. In example, the Ising model Hamiltoninan of Eq.(4.4) is actually derived from

$$\mathscr{H} = -\sum_{\langle ij \rangle} \left[\widetilde{J} s_i s_j + \widetilde{G} \right] , \tag{4.46}$$

where $\widetilde{G}$ and $\widetilde{J}$ are the interaction constants in energy units. The dimensionless interaction constants are defined as

$$\begin{aligned} J &\equiv \frac{\widetilde{J}}{k_BT} , \\ G &\equiv \frac{\widetilde{G}}{k_BT} . \end{aligned} \tag{4.47}$$

Hence, we can define the temperature for the system as

$$T \equiv \frac{\widetilde{J}}{k_BJ} , \tag{4.48}$$

which is a satisfactory and yet physically expressive temperature definition for RG theory calculations: as the temperature increases the dimensionless nearest-neighbor interactions become weaker, and *vice versa*. However, the definition can be further simplified. Since $\widetilde{J}$ is constant for a particular material in concern and can be taken as unity, in the unit system of $k_B = 1$, the temperature can be defined as

$$T \equiv \frac{1}{J} . \tag{4.49}$$

For the calculation of response functions, let us consider the specific heat per site for the 1-dimensional Ising model, for which the internal energy per site was given with Eq.(4.45). The specific heat per site is the derivative of internal energy per site with respect to temperature. Thus,

$$
\begin{aligned}
C &= \frac{\partial U}{\partial T} \\
&= \frac{\partial}{\partial T}\left(-k_B T J \langle s_i s_{i+1}\rangle\right) \\
&= \frac{\partial J}{\partial T}\frac{\partial}{\partial J}\left(-\widetilde{J}\langle s_i s_{i+1}\rangle\right) \\
&= -\widetilde{J}\frac{\partial}{\partial T}\left(\frac{\widetilde{J}}{k_B T}\right)\frac{\partial\langle s_i s_{i+1}\rangle}{\partial J} \\
&= \frac{\widetilde{J}^2}{k_B T^2}\frac{\partial\langle s_i s_{i+1}\rangle}{\partial J} \\
&= k_B J^2\ \frac{\partial\langle s_i s_{i+1}\rangle}{\partial J} = C\ . \qquad (4.50)
\end{aligned}
$$

We can use this expression in RG calculations in order to calculate the specific heat per site globally at every tempreture.

The derivation of other response functions follow the same routine in genaral, making the RG theory a very powerful tool to obtain global thermodynamics over the whole Hamiltonian space of almost all systems. This is a major advantage of RG theory over many other methods that usually work best for some limits of the thermodynamical field space, or even worse, only at the ground states.

4.6 Calculation of phase diagrams

Each phase in the phase diagram has its own fixed point, which is called phase sink. All points within a phase flow to the sink of that phase under successive RG transformations. Interactions, and more importantly densities, calculated at a sink determine the properties of the corresponding phase. There might be more than one phase sink corresponding to a single phase.

Phase boundaries also have their own fixed points, where the relevant exponent analysis give the order of the phase transition. The largest eigenvalue of recursion matrix is always b^d at a phase boundary fixed point, which corresponds to the additive constant term $\partial_G G'$. The rest of the eigenvalues are b^{y_1}, b^{y_2}, ..., $b^{y_{m-1}}$, where m is the number of interactions (*e.g.*, $m = 2$ in the Ising model) and $y_1 > 0$, the relevant exponent, is the only positive one among the exponents $\{y\}$. We have three cases at a phase boundary fixed point: (*i*) In the case $y_1 = d - 1$ the phase boundary is a null one, indicating that a continuous evolution between the phases it separates occurs while crossing the boundary. A typical example of null boundary is the up-magnetized – down-magnetized phase boundary in Ising model above the critical temperature $T > T_c$ at zero external magnetic field ($H = 0$). Another example is the liquid-gas phase boundary above the critical point for water. In these examples, systems cross from one phase to another continuously without any occurance of phase transition. (*ii*) In the case $y_1 = d$ we have two exponents being equal to d, indicating two-phase coexistance, thus a first-order phase transition. Discontinuous jumps occur in relevant densities while crossing a first-order phase transition boundary. The $T < T_c$, $H = 0$ phase boundary for Ising model is a typical example, where up-magnetized and down-magnetized phases coexist and a jump in magnetization exists. (*iii*) The case $0 < y_1 < d$ corresponds to a second-order phase transition, in which the densities themselves are continuous, but the response functions (derivatives of densities with respect to interactions) are discontinuous or infinite. The transition from ferromagnetic to paramagnetic phase at $T = T_c$ for Ising model is a second-order phase transition, where magnetization continuously vanishes, however specific heat and susceptibility asymptotically diverge to infinity.

Thus, using a renormalization-group theoretical approach mentioned above we can calculate the thermodynamic functions and the phase diagram for a given model Hamiltonian for the whole range of thermodynamic fields, including temperature and external fields. This globally valid set of techniques makes the RG theory the utmost tool in the study of model Hamiltonians.

4.7 Overview

We discussed a great deal of exact and approximate techniques based on renormalization-group theoretical approach. However, our discussion given in this chapter should not be understood as covering all the concepts related to the renormalization-group theory, and the reader should not have the illusion that this is the end of the story. For example, we did not mention even a word about the momentum space renormalization group, which sets a large field of study by itself, or about the "*universality*", that is one of the most fascinating phenomena of the nature that can be fully understood only by renormalization-group theory. In fact, our main aim in this chapter was not to cover the renormalization-group theory in all

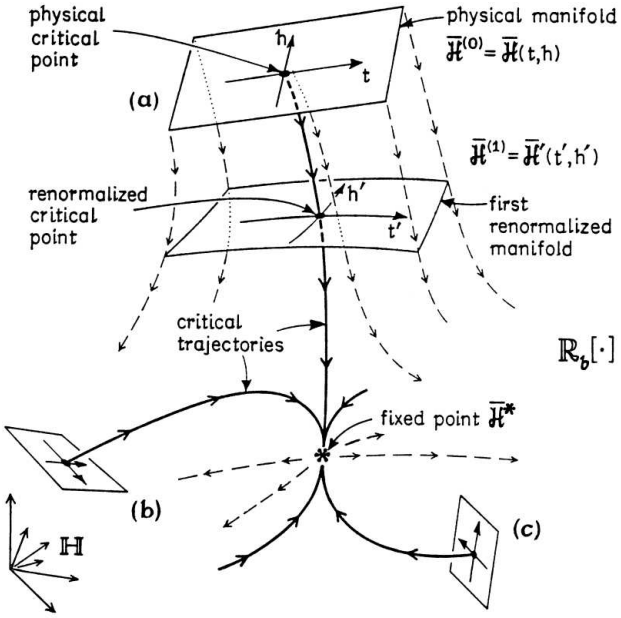

Figure 4.3: A schematic illustration of the RG theory. The physical Hamiltonians (a), (b), and (c), shown by manifolds, lie in a space of Hamiltonians denoted by $\mathbb{H}$ with infinitely many other Hamiltonians. RG flows are shown for a rescaling factor of b. Critical trajectories are shown in bold. The different critical points of physically different systems ending up at the same fixed point denoted by $\overline{\mathscr{H}}^*$ under successive RG transformations is the best theoretical explanation to the universality phenomena, namely diverse physical systems having the same critical exponents (from [122]).

aspects, but rather to introduce the general idea of renormalization-group theory, and the set of tools based on it, to use for the investigation of the phase diagram of a quantum mechanical model Hamiltonian, which is derived from the Hubbard model and will be introduced in the next chapter.

Nonetheless, an interested reader on the subject may be referred to exhaustive books and reviews on renormalization-group theory, *e.g.*, [119, 120, 121] and references therein. We would like to conclude this chapter with a frequently cited figure [122], that depicts the renormalization-group idea in general, given above in Fig. 4.3.

Chapter 5

SPINLESS FALICOV–KIMBALL MODEL

5.1 Introduction

The Fermi-Fermi Falicov–Kimball model (FKM)[1], was first proposed by L. M. Falicov and Kimball [123] to analyze the thermodynamics of semiconductor-metal transitions in SmB_6 and transition-metal oxides [124, 125, 126, 127]. The model incorporates two types of electrons: one type can undergo hopping between sites and the other type cannot hop, thereby being localized at the sites. Thus, in its introduction, FKM described the Coulomb interaction between mobile d band electrons and localized f band electrons. There have been a multitude of subsequent physical interpretations based on this interaction, including that of localized ions attractively interacting with mobile electrons that yields crystalline formation [128, 129]. Yet another physical interpretation of the model is as a binary alloy, in which the localized degree of freedom reflects A or B atom occupation [130, 131]. In this thesis, we employ the original language, with d and f electrons as "*conduction*" and "*localized*" electrons with a repulsive interaction between them.

For no interacting spin degrees of freedom exists in the Hamiltonian, the model is traditionally studied in the spinless case, commonly referred as the spinless FKM (SFKM) and which is in fact a limiting case of the Hubbard model when one type of spin (*e.g.*, spin-$\downarrow$) cannot hop [77, 78, 79]. In spite of the model's simplicity, it is able to describe many physical phenomena in rare-earth and transition metal compounds such as metal transitions, charge-ordering, *etc.* This non-trivial nature of SFKM motivated us to capture the first global phase diagram of the model.

Beyond the introduction of spin degree of freedom for both electrons [132, 133, 134, 135, 136, 137, 138, 139, 140, 141, 142, 143, 144, 145, 146, 147, 148], there also exist many extensions of the original model. The most widely studied extensions include multiband hybridization [149, 150, 151, 152, 153, 154, 155, 156], f-f hopping [157, 158, 159, 160, 161], correlated hopping [162, 163, 164, 165, 166], non-bipartite lattices [167, 168], hard-core bosonic particles [168], magnetic fields [140, 145, 146, 147, 148, 168, 169], next-nearest-neighbor hopping [170], *etc.* Exhaustive reviews are available in Refs. [171, 172, 173, 174].

[1]For the sake of simplicity, in the case of no bosonic particles, the Fermi-Fermi Falicov–Kimball model will be referred simply as Falicov–Kimball model (FKM)

Since its invention, the wider physical application of both the basic FKM and its extended versions have aimed to explain a collection of physical phenomena including valence transitions [133, 139, 140, 141], metal-insulator transitions [133, 142, 143, 144, 175], mixed valence phenomena [176], Raman scattering [177], colossal magnetoresistance [145, 146, 147, 148], electronic ferroelectricity [155, 158, 159, 160], phase separation [133, 161, 162, 178, 179, 180], *etc.*

After the initial works on the FKM [123, 124, 125, 126, 127], literature had to wait 14 years for the celebrated first rigorous results. Two independent studies, by Kennedy and Lieb [128, 129], and by Brandt and Schmidt [181, 182] suggested that, at low temperatures, FKM has long-range order. Various methods have been used in the study of the FKM. In most of these studies, either the $d \to \infty$ infinite-dimensional limit or $d = 1, 2$ low-dimensional cases have been investigated. Studies include limiting cases such as ground-state analysis, or the large interaction limit. RG theory, as described in the previous chapter, offers fully physical and fairly easy techniques to yield global phase diagrams and other thermodynamic properties. We use the general method for arbitrary dimensional quantum systems developed by A. Falicov and Berker [102] to obtain the global phase diagram of the SFKM in $d = 3$.

5.2 The model

5.2.1 Derivation of SFKM Hamiltonian

In this section we will modify the Hubbard model in order to obtain the simpler but yet physically rich enough SFKM, and investigate the symmetries of the model. First of all, let us recall the Hubbard model defined in Eq.(3.70):

$$\mathscr{H} = -\widetilde{t}_0 \sum_{\langle ij \rangle} \sum_{\sigma} \left(c^{\dagger}_{i\sigma} c_{j\sigma} + c^{\dagger}_{j\sigma} c_{i\sigma} \right) - \widetilde{U}_0 \sum_{i} n_{i\uparrow} n_{i\downarrow} \ , \tag{5.1}$$

where we switched our notation from t and U to $\widetilde{t}_0$ and $\widetilde{U}_0$ in order to emphasise that these constants are in units of energy, in accord with our discussion on RG theory.[2] We have omited the tildes previously for the sake of simplicity. Furthermore, as might be already noticed, we changed the sign of the Hubbard U, so that a negative (positive) value of $\widetilde{U}_0$ corresponds to a Coulomb repulsion (attraction). As we mentioned before, the competing interactions of $\widetilde{t}_0$ and $\widetilde{U}_0$ induces a metal-insulator transition.

Now, let us assume that the two types of electrons, *i.e.*, spin-$\uparrow$ and spin-$\downarrow$, do not contribute equivalently to the conductivity. We will simply assume that one type of spins (say spin-$\downarrow$) is always localized on the atomic orbitals, while the other one (spin-$\uparrow$) can hop between nearest-neighboring sites. Accordingly, we can write the Hamiltonian as

$$\mathscr{H} = -\widetilde{t}_0 \sum_{\langle ij \rangle} \left(c^{\dagger}_{i} c_{j} + c^{\dagger}_{j} c_{i} \right) - \widetilde{U}_0 \sum_{i} n_i w_i \ , \tag{5.2}$$

where we dropped the spin indices, which are unnecessary anymore, and thus, the electrons can be called as "*spinless*". Although being spinless, defined particles are still fermions, *i.e.*, the Pauli exclusion principle forbids the occupation of a given site by more than one localized electron or by more than one hopping (conduction) electron. The creation and annihilation operators for the conduction electrons at lattice site i, $c^{\dagger}_i$ and c_i, obey the CAR algebra defined by anticommutation rules of $\{c_i, c_j\} = \{c^{\dagger}_i, c^{\dagger}_j\} = 0$ and $\{c^{\dagger}_i, c_j\} = \delta_{ij}$ [*cf.* Eq.(3.37)]. Here, $n_i = c^{\dagger}_i c_i$ is

[2] The 0-subscripts will be dropped soon in another transformation.

the number operator for conduction electrons, while w_i is the number of localized electrons, both at site i. The operator w_i takes the values 1 or 0, for site i being respectively occupied or unoccupied by a localized electron. Hence, the localized electrons are in fact, classical particles, since they enter the model Hamiltonian only through the classical variable w_i.

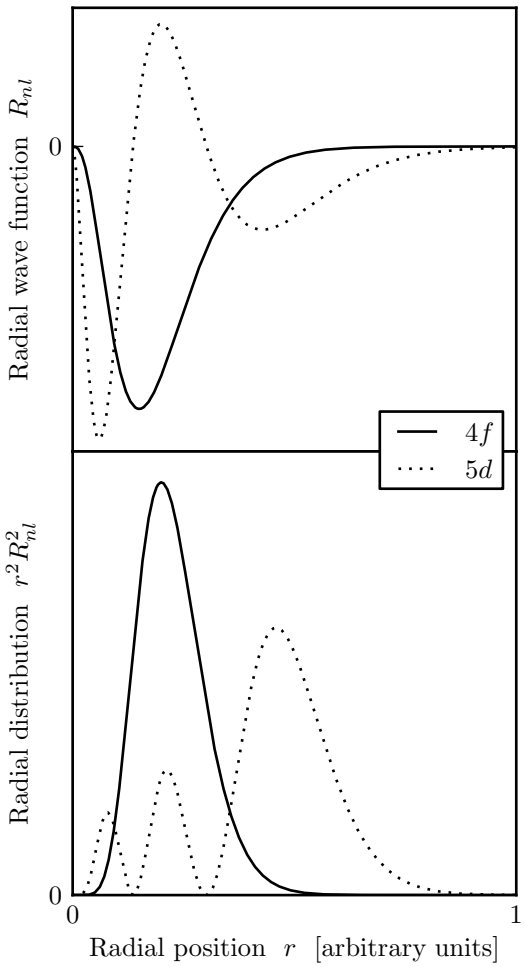

Figure 5.1: Radial wave functions, R_{nl}, (upper panel) and radial probability distribution functions, $r^2R_{nl}^2$, (lower panel) plotted with respect to radial distance from nucleus, r. Curves correspond to hydrogen-like atomic orbitals of $4f$ ($n = 4$, $l = 3$, full line) and $5d$ ($n = 5$, $l = 2$, dotted line). Note the extension for the $5d$ atomic orbital compared to the $4f$ orbital.

The assumption we made above to simplify the Hubbard model is actually based on relevant physically expressive grounds. Although the phenomena described by the SFKM, like charge-ordering, occur generally in complicated compounds of rare-earth and transition-metals, *e.g.*, $La_{1-x}Ca_xMnO_3$ [183, 184, 185, 186, 187, 188, 189], we will give the simple example of a cerium crystal in order to illustrate the point. The lanthanide rare-earth metal Ce has the electron configuration of [Xe]$6s^2 4f\ 5d$, and the unit cell of the face-centered cubic Ce crystal contains two unpaired electrons: a $4f$ electron and a $5d$ electron. Above in Fig. 5.1, we present the radial wave functions and probability distributions for the hydrogen-like $4f$ and $5d$ atomic orbitals. Although the real corresponding atomic orbitals of Ce will be more complicated, from this simplistic picture we can fairly assert that the $4f$ orbital is more localized on the ion than the $5d$ atomic orbital. Thus, it is a fair assumption to treat the $4f$ electrons as localized. Therefore, it is only the $5d$ electrons that can hop between nearest-neighboring sites and contribute to the conductivity of the crystal. Besides, since there will be no interacting spin degrees of freedom, we can justly work within the spinless case.

In the previous chapters, we discussed that the strongly correlated electron systems are drived to a metal-insulator transition by the competing effects of the tight-binding hopping and the on-site Coulomb repulsion. We equivalently derived the same expected phase transition by considering a variable lattice spacing, that in turn, tunes the overlap and tight-binding hopping integrals. Mott formulates this variation in lattice spacing as a change in the electron density, which is more convenient, and gives a transition criterion in terms of charge carrier density [*c.f.* Eq.(2.51)]. Thus, we should include the chemical potential terms into the Hamiltonian given in Eq.(5.2), in order to introduce the control on localized and conduction electron densities, or equivalently on pressure. This leads to the Hamiltonian,

$$\mathscr{H} = -\widetilde{t}_0 \sum_{\langle ij \rangle} \left(c_i^\dagger c_j + c_j^\dagger c_i \right) - \widetilde{U}_0 \sum_i n_i w_i - \widetilde{\mu}_0 \sum_i n_i - \widetilde{\nu}_0 \sum_i w_i \ , \qquad (5.3)$$

or equivalently, to the dimensionless Hamiltonian,

$$-\beta\mathscr{H} = t_0 \sum_{\langle ij \rangle} \left(c_i^\dagger c_j + c_j^\dagger c_i \right) + U_0 \sum_i n_i w_i + \mu_0 \sum_i n_i + \nu_0 \sum_i w_i \ , \qquad (5.4)$$

where $\beta = 1/k_B T$, and the dimensionless interaction constants are defined as $K_0 \equiv \beta \widetilde{K}_0$, in short. Furthermore, in order to carry out an RG transformation easily, we trivially rearrange the above Hamiltonian into a convenient and equivalent form of

$$\begin{aligned} -\beta\mathscr{H} &= \sum_{\langle ij \rangle} \left[t \left(c_i^\dagger c_j + c_j^\dagger c_i \right) + U \left(n_i w_i + n_j w_j \right) + \mu \left(n_i + n_j \right) + \nu \left(w_i + w_j \right) \right] \\ &\equiv \sum_{\langle ij \rangle} \left[-\beta \mathscr{H}_{i,j} \right] \ . \end{aligned} \qquad (5.5)$$

Here, we defined $t \equiv t_0$, $U \equiv U_0/z$, $\mu \equiv \mu_0/z$, and $\nu \equiv \nu_0/z$, where the dividing factor z is the lattice coordination number, and $z = 2d$ for a d-dimensional hypercubic lattice. Our calculation of the global phase diagram will be for a simple cubic lattice, hence, we will assume $z = 6$. The Hamiltonian given above defines the "*spinless Falicov–Kimball model*" (*SFKM*).

5.2.2 Symmetries of SFKM Hamiltonian

The first term of the SFKM Hamiltonian given in Eq.(5.5) is the kinetic energy term, responsible for the quantum nature of the model. The Hamiltonian reduces to a classical model (indeed a trivial one) for $t = 0$, since all other operators, namely n_i and w_i commute with the Hamiltonian. The system being invariant under sign change of t (via a phase change of the local basis states in one sublattice), only positive t values will be considered throughout this thesis.

The second term of the SFKM Hamiltonian is the screened on-site Coulomb interaction between localized and conduction electrons, with positive and negative U values corresponding to attractive and repulsive interactions. We will consider only the repulsive case, since the attractive case can be connected to the repulsive one by the particle-hole symmetry possessed by either type of electrons. Particle-hole symmetries are achieved by the transformations of

$$w_i \to 1 - w_i \qquad (5.6)$$

for the localized electrons and

$$c_i^\dagger \to \kappa_i c_i \quad \text{and} \quad c_i \to \kappa_i c_i^\dagger \tag{5.7}$$

for the conduction electrons, where, for a bipartite lattice, $\kappa_i = 1$ for one sublattice and $\kappa_i = -1$ for the other [130, 174].

The last two terms of the SFKM Hamiltonian are the chemical potential terms with $z\nu$ and $z\mu$ being the dimensionless chemical potential for a localized and conduction electron for a lattice with coordination number z. As a direct consequence of the particle-hole symmetries given above, the physics of the SFKM is invariant under the transformation

$$\nu/U \to 1 - \nu/U \quad \text{and} \quad \mu/U \to 1 - \mu/U \ . \tag{5.8}$$

This leads to the invariance under the density transformation of

$$\langle w_i \rangle \to 1 - \langle w_i \rangle \quad \text{and} \quad \langle n_i \rangle \to 1 - \langle n_i \rangle \ , \tag{5.9}$$

where $\langle w_i \rangle$ and $\langle n_i \rangle$ are the densities corresponding to the operators w_i and n_i respectively. We will omit the hat notation for the operators anymore, since we will not work with the eigenvalues of the operators, but with the expectation values denoted by $\langle a \rangle$ for the corresponding operator a. Therefore, no confusion will arise due to our notation.

The particle-hole symmetries for SFKM are depicted in Fig. 5.2 below. A physical picture of "itinerant electrons hopping in the background of localized electrons" changes into a converse picture of "conduction holes interacting with localized holes" under the particle-hole transformations for both types of particles. However, it is obvious that, all the thermodynamic properties (apart from densities) of the system remain invariant under this particle-hole symmetry transformation.

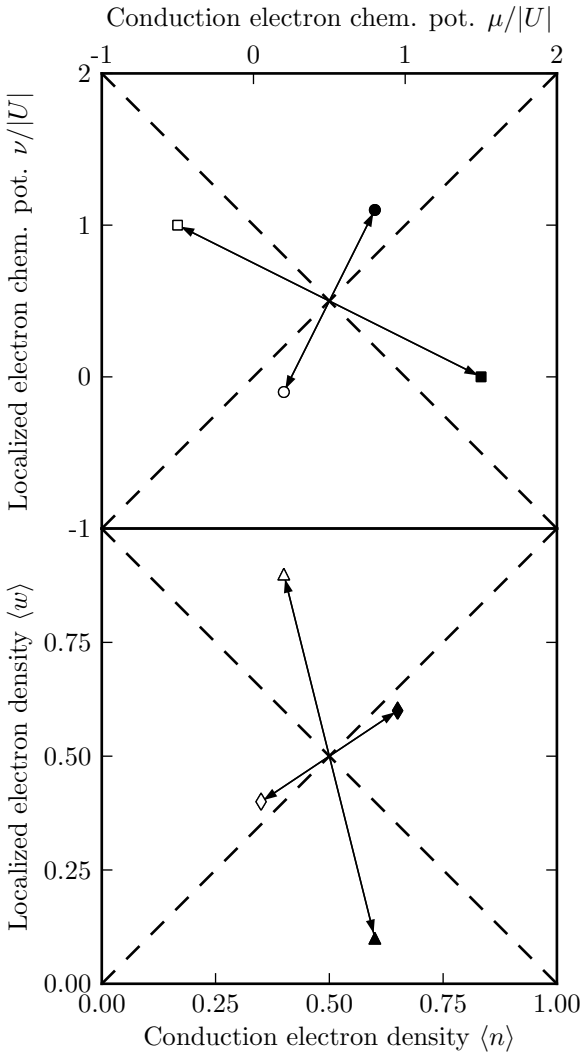

Figure 5.2: Particle-hole symmetries induced in the SFKM in chemical potential space (upper panel) and density space (lower panel). Examplar points connected under particle-hole symmetry transformations of both localized and conduction electrons are shown by various open and full symbols connected by arrows. The particle-hole symmetric point is achieved by two succesive mirror reflection operations through the symmetry axes denoted by dashed lines [*cf.* Eqs.(5.8,5.9)]. Thus, any two adjacent triangles contain all the physical information in both views of grand canonical (upper panel) and of canonical (lower panel) ensembles.

5.3 RG details

This section is devoted to the renormalization-group theoretical details associated with the SFKM problem. We will perform practical applications of the techniques mentioned in the previous chapter, and derive the recursion relations in a closed form to be calculated numerically in the study of the global phase diagram of the SFKM.

5.3.1 Suzuki–Takano method in $d = 1$

The Suzuki–Takano RG transformation given in Eq.(4.22) of the previous chapter is algebraically summarized in [100, 101]

$$\mathrm{e}^{-\beta' \mathscr{H}'_{i,k}} = \mathrm{Tr}_j \, \mathrm{e}^{-\beta \mathscr{H}_{i,j} - \beta \mathscr{H}_{j,k}} \ , \tag{5.10}$$

where i, j, k are three successive sites, and the form of $-\beta \mathscr{H}_{i,j}$ is given in Eq.(5.5) for the SFKM. Here, the operator $-\beta' \mathscr{H}'_{i,k}$ acts on two-site states, while the operator $-\beta \mathscr{H}_{i,j} - \beta \mathscr{H}_{j,k}$ acts on three-site states. Thus, we can rewrite Eq.(5.10) in matrix form as

$$\langle u_i v_k | \mathrm{e}^{-\beta' \mathcal{H}'_{i,k}} | \bar{u}_i \bar{v}_k \rangle = \sum_{s_j} \langle u_i \, s_j \, v_k | \mathrm{e}^{-\beta \mathcal{H}_{i,j} - \beta \mathcal{H}_{j,k}} | \bar{u}_i \, s_j \, \bar{v}_k \rangle \ , \tag{5.11}$$

where state variables u_ℓ, v_ℓ, s_ℓ, $\bar{u}_\ell$, and $\bar{v}_\ell$ can be one of the four possible single-site $|w_\ell \, n_\ell\rangle$ states at each site ℓ, namely one of $|00\rangle$, $|01\rangle$, $|10\rangle$, and $|11\rangle$. Eq.(5.11) indicates that the unrenormalized 64×64 matrix on the right-hand side is contracted into the renormalized 16×16 matrix on the left-hand side. We use two-site basis states, $\{|\phi_p\rangle\}$, and three-site basis states, $\{|\psi_q\rangle\}$, in order to block-diagonalize the matrices in Eq.(5.11). These basis states are the eigenstates of total conduction and localized electron numbers. The set of $\{|\phi_p\rangle\}$ and $\{|\psi_q\rangle\}$ are given in Tables 5.1 and 5.2 respectively.

With these basis states, Eq.(5.11) can be rewritten as

$$\langle \phi_p | \mathrm{e}^{-\beta' \mathscr{H}'_{i,k}} | \phi_{\bar{p}} \rangle = \sum_{\substack{u,v, \\ \bar{u},\bar{v},s}} \sum_{q,\bar{q}} \langle \phi_p | u_i v_k \rangle \langle u_i s_j v_k | \psi_q \rangle \langle \psi_q | \mathrm{e}^{-\beta \mathscr{H}_{i,j} - \beta \mathscr{H}_{j,k}} | \psi_{\bar{q}} \rangle \langle \psi_{\bar{q}} | \bar{u}_i s_j \bar{v}_k \rangle \langle \bar{u}_i \bar{v}_k | \phi_{\bar{p}} \rangle \ . \tag{5.12}$$

w	n	u_2	Two-site basis states
0	0	+	$\|\phi_1\rangle = \|00,00\rangle$
0	1	+	$\|\phi_2\rangle = \frac{1}{\sqrt{2}}\{\|00,01\rangle + \|01,00\rangle\}$
0	1	−	$\|\phi_3\rangle = \frac{1}{\sqrt{2}}\{\|00,01\rangle - \|01,00\rangle\}$
0	2	−	$\|\phi_4\rangle = \|01,01\rangle$
1	0	+	$\|\phi_5\rangle = \|00,10\rangle$
1	1	+	$\|\phi_6\rangle = \frac{1}{\sqrt{2}}\{\|00,11\rangle + \|01,10\rangle\}$
1	1	−	$\|\phi_7\rangle = \frac{1}{\sqrt{2}}\{\|00,11\rangle - \|01,10\rangle\}$
1	2	−	$\|\phi_8\rangle = \|01,11\rangle$
2	0	+	$\|\phi_{13}\rangle = \|10,10\rangle$
2	1	+	$\|\phi_{14}\rangle = \frac{1}{\sqrt{2}}\{\|10,11\rangle + \|11,10\rangle\}$
2	1	−	$\|\phi_{15}\rangle = \frac{1}{\sqrt{2}}\{\|10,11\rangle - \|11,10\rangle\}$
2	2	−	$\|\phi_{16}\rangle = \|11,11\rangle$

Table 5.1: The two-site basis states that appear in Eq.(5.12) in the form $|w_i n_i, w_j n_j\rangle$. The total localized and conduction electron numbers w and n, the eigenvalue u_2 of the operator T_{ij} defined after Eq.(5.13) are indicated. $|\phi_{9-12}\rangle$ are respectively obtained from $|\phi_{5-8}\rangle$ by the act of T_{ij}, while the corresponding Hamiltonian matrix elements are multiplied by the u_2 values of the states.

Once written in the basis states $\{|\phi_p\rangle\}$, the block-diagonal renormalized matrix has 13 independent elements, which means that RG transformation of the Hamiltonian generates 9 more interaction constants apart from t, U, μ, and ν. In this 13-dimensional interaction space, the form of the Hamiltonian stays closed under RG transformations. This Hamiltonian is

$$\begin{aligned} -\beta\mathcal{H}_{i,j} = & \, t\left(c_i^\dagger c_j + c_j^\dagger c_i\right) + U\left(n_i w_i + n_j w_j\right) + \mu\left(n_i + n_j\right) + \nu\left(w_i + w_j\right) \\ & + J n_i n_j + K w_i w_j + L n_i n_j w_i w_j + P\left(n_i w_j + n_j w_i\right) + V_n n_i n_j (w_i + w_j) \\ & + V_w (n_i + n_j) w_i w_j + Q\, T_{i,j} w_i w_j + R\, T_{i,j}(w_i + w_j) + G\ , \end{aligned} \tag{5.13}$$

where $T_{i,j}$ is a local operator that switches the conduction electron states of sites i and j, namely, $T_{i,j}|w_i n_i, w_j n_j\rangle = u_2 |w_i n_j, w_j n_i\rangle$ with $u_2 = 1$ for $n_i + n_j < 2$ and $u_2 = -1$ otherwise. When T_{ik} is applied, further below, to three consecutive sites

w	n	u_3	Three-site basis states	w	n	u_3	Three-site basis states
0	0	+	$\|\psi_1\rangle = \|00,00,00\rangle$	3	0	+	$\|\psi_{57}\rangle = \|10,10,10\rangle$
0	1	+	$\|\psi_2\rangle = \frac{1}{\sqrt{2}}\{\|00,00,01\rangle + \|01,00,00\rangle\}$	3	1	+	$\|\psi_{58}\rangle = \frac{1}{\sqrt{2}}\{\|10,10,11\rangle + \|11,10,10\rangle\}$
0	1	+	$\|\psi_3\rangle = \|00,01,00\rangle$	3	1	+	$\|\psi_{59}\rangle = \|10,11,10\rangle$
0	1	−	$\|\psi_4\rangle = \frac{1}{\sqrt{2}}\{\|00,00,01\rangle - \|01,00,00\rangle\}$	3	1	−	$\|\psi_{60}\rangle = \frac{1}{\sqrt{2}}\{\|10,10,11\rangle - \|11,10,10\rangle\}$
0	2	+	$\|\psi_5\rangle = \frac{1}{\sqrt{2}}\{\|00,01,01\rangle - \|01,01,00\rangle\}$	3	2	+	$\|\psi_{61}\rangle = \frac{1}{\sqrt{2}}\{\|10,11,11\rangle - \|11,11,10\rangle\}$
0	2	−	$\|\psi_6\rangle = \|01,00,01\rangle$	3	2	−	$\|\psi_{62}\rangle = \|11,10,11\rangle$
0	2	−	$\|\psi_7\rangle = \frac{1}{\sqrt{2}}\{\|00,01,01\rangle + \|01,01,00\rangle\}$	3	2	−	$\|\psi_{63}\rangle = \frac{1}{\sqrt{2}}\{\|10,11,11\rangle + \|11,11,10\rangle\}$
0	3	−	$\|\psi_8\rangle = \|01,01,01\rangle$	3	3	−	$\|\psi_{64}\rangle = \|11,11,11\rangle$
1	0	+	$\|\psi_9\rangle = \|00,00,10\rangle$	2	0	+	$\|\psi_{33}\rangle = \|00,10,10\rangle$
1	0	+	$\|\psi_{10}\rangle = \|00,10,00\rangle$	2	0	+	$\|\psi_{34}\rangle = \|10,00,10\rangle$
1	1	+	$\|\psi_{12}\rangle = \frac{1}{\sqrt{2}}\{\|00,00,11\rangle + \|01,00,10\rangle\}$	2	1	+	$\|\psi_{36}\rangle = \frac{1}{\sqrt{2}}\{\|00,10,11\rangle + \|01,10,10\rangle\}$
1	1	+	$\|\psi_{13}\rangle = \frac{1}{\sqrt{2}}\{\|00,10,01\rangle + \|01,10,00\rangle\}$	2	1	+	$\|\psi_{37}\rangle = \frac{1}{\sqrt{2}}\{\|10,00,11\rangle + \|11,00,10\rangle\}$
1	1	+	$\|\psi_{15}\rangle = \|00,01,10\rangle$	2	1	+	$\|\psi_{39}\rangle = \|00,11,10\rangle$
1	1	+	$\|\psi_{16}\rangle = \|00,11,00\rangle$	2	1	+	$\|\psi_{40}\rangle = \|10,01,10\rangle$
1	1	−	$\|\psi_{18}\rangle = \frac{1}{\sqrt{2}}\{\|00,00,11\rangle - \|01,00,10\rangle\}$	2	1	−	$\|\psi_{42}\rangle = \frac{1}{\sqrt{2}}\{\|00,10,11\rangle - \|01,10,10\rangle\}$
1	1	−	$\|\psi_{19}\rangle = \frac{1}{\sqrt{2}}\{\|00,10,01\rangle - \|01,10,00\rangle\}$	2	1	−	$\|\psi_{43}\rangle = \frac{1}{\sqrt{2}}\{\|10,00,11\rangle - \|11,00,10\rangle\}$
1	2	+	$\|\psi_{21}\rangle = \frac{1}{\sqrt{2}}\{\|00,01,11\rangle - \|01,01,10\rangle\}$	2	2	+	$\|\psi_{45}\rangle = \frac{1}{\sqrt{2}}\{\|00,11,11\rangle - \|01,11,10\rangle\}$
1	2	+	$\|\psi_{22}\rangle = \frac{1}{\sqrt{2}}\{\|00,11,01\rangle - \|01,11,00\rangle\}$	2	2	+	$\|\psi_{46}\rangle = \frac{1}{\sqrt{2}}\{\|10,01,11\rangle - \|11,01,10\rangle\}$
1	2	−	$\|\psi_{24}\rangle = \|01,00,11\rangle$	2	2	−	$\|\psi_{48}\rangle = \|01,10,11\rangle$
1	2	−	$\|\psi_{25}\rangle = \|01,10,01\rangle$	2	2	−	$\|\psi_{49}\rangle = \|11,00,11\rangle$
1	2	−	$\|\psi_{27}\rangle = \frac{1}{\sqrt{2}}\{\|00,01,11\rangle + \|01,01,10\rangle\}$	2	2	−	$\|\psi_{51}\rangle = \frac{1}{\sqrt{2}}\{\|00,11,11\rangle + \|01,11,10\rangle\}$
1	2	−	$\|\psi_{28}\rangle = \frac{1}{\sqrt{2}}\{\|00,11,01\rangle + \|01,11,00\rangle\}$	2	2	−	$\|\psi_{52}\rangle = \frac{1}{\sqrt{2}}\{\|10,01,11\rangle + \|11,01,10\rangle\}$
1	3	−	$\|\psi_{30}\rangle = \|01,01,11\rangle$	2	3	−	$\|\psi_{54}\rangle = \|01,11,11\rangle$
1	3	−	$\|\psi_{31}\rangle = \|01,11,01\rangle$	2	3	−	$\|\psi_{55}\rangle = \|11,01,11\rangle$

Table 5.2: The three-site basis states that appear in Eq.(5.12) in the form $|w_i n_i, w_j n_j, w_k n_k\rangle$. The total localized and conduction electron numbers w and n, the eigenvalue u_3 of the operator T_{ik} defined after Eq.(5.13) are indicated. $\{|\psi_{11+3x}\rangle\}$, $x = 0, 1, \ldots, 15$, are respectively obtained from $\{|\psi_{9+3x}\rangle\}$ by the act of T_{ik}, while the corresponding Hamiltonian matrix elements are multiplied by the u_3 values of the states.

i, j, k, $T_{ik}|w_i n_i, w_j n_j, w_k n_k\rangle = u_3|w_i n_k, w_j n_j, w_k n_i\rangle$ with $u_3 = 1$ for $n_i + n_j + n_k < 2$ and $u_3 = -1$ otherwise. These operators are defined according to the normal order and the CAR algebra, discussed in a previous chapter.

The matrix elements of the block-diagonal renormalized 2-site Hamiltonian in the $\{|\phi_p\rangle\}$ basis are given below in Eq.(5.14), where $\langle\phi_p| - \beta' \mathscr{H}'_{i,k}|\phi_p\rangle = \epsilon_p + G'$ for the 12 independent diagonal elements and $\langle\phi_6| - \beta' \mathscr{H}'_{i,k}|\phi_7\rangle = \epsilon_0$ for the only independent off-diagonal element.

$$\epsilon_0 = (U' - P')/2,\ \epsilon_1 = 0,\ \epsilon_2 = t' + \mu',\ \epsilon_3 = -t' + \mu',\ \epsilon_4 = 2\mu' + J',\ \epsilon_5 = \nu' + R',$$
$$\epsilon_6 = t' + U'/2 + \mu' + \nu' + P'/2 + R', \quad \epsilon_7 = -t' + U'/2 + \mu' + \nu' + P'/2 - R',$$
$$\epsilon_8 = U' + 2\mu' + \nu' + J' + P' + V_n' - R', \quad \epsilon_{13} = 2\nu' + K' + Q' + 2R',$$
$$\epsilon_{14} = t' + U' + \mu' + 2\nu' + K' + P' + V_w' + Q' + 2R',$$
$$\epsilon_{15} = -t' + U' + \mu' + 2\nu' + K' + P' + V_w' - Q' - 2R',$$
$$\epsilon_{16} = 2(U' + \mu' + \nu') + J' + K' + L' + 2(P' + V_n' + V_w') - Q' - 2R'. \quad (5.14)$$

$$\varepsilon_1 = 0, \quad \varepsilon_2 = \varepsilon_3 = \varepsilon_4 = \varepsilon_6/2 = \mu, \quad \varepsilon_5 = \varepsilon_7 = 2\mu + J, \quad \varepsilon_8 = 3\mu + 2J,$$
$$\varepsilon_9 = \varepsilon_{34}/2 = \nu + R, \quad \varepsilon_{10} = \nu + 2R, \quad \varepsilon_{12} = \varepsilon_{18} = U/2 + \mu + \nu + R/2,$$
$$\varepsilon_{13} = \varepsilon_{19} = \mu + \nu + P + R, \quad \varepsilon_{15} = \mu + \nu + P, \quad \varepsilon_{16} = \varepsilon_{49}/2 = U + \mu + \nu,$$
$$\varepsilon_{21} = U/2 + 2\mu + \nu/2 + J + P + (V_n - R)/2, \quad \varepsilon_{22} = \varepsilon_{28} = U + 2\mu + \nu + J + P + V_n - R,$$
$$\varepsilon_{24} = U + 2\mu + \nu, \quad \varepsilon_{25} = 2\mu + \nu + 2P, \quad \varepsilon_{27} = U/2 + 2\mu + \nu + J + P + (V_n - R)/2,$$
$$\varepsilon_{30} = U + 3\mu + \nu + 2J + P + V_n - R, \quad \varepsilon_{31} = U + 3\mu + \nu + 2(J + P + V_n - R),$$
$$\varepsilon_{33} = 2\nu + K + Q + 3R, \quad \varepsilon_{36} = \varepsilon_{42} = U/2 + \mu + 2\nu + K + P + (V_w + Q + 3R)/2,$$
$$\varepsilon_{37} = \varepsilon_{43} = U + \mu + 2\nu + R, \quad \varepsilon_{39} = U + \mu + 2\nu + K + P + V_w, \quad \varepsilon_{40} = \mu + 2(\nu + P),$$
$$\varepsilon_{45} = \varepsilon_{51} = 3U/2 + 2(\mu + \nu) + J + K + L/2 + 2P + 3(V_n + V_w)/2 - (Q + 3R)/2,$$
$$\varepsilon_{46} = \varepsilon_{52} = U + 2(\mu + \nu) + J + 2P + V_n - R, \quad \varepsilon_{48} = U + 2(\mu + \nu) + K + 2P + V_w,$$
$$\varepsilon_{54} = 2U + 3\mu + 2(\nu + J) + K + L + 3(P + V_n) + 2V_w - Q - 3R,$$
$$\varepsilon_{55} = 2U + 3\mu + 2(\nu + J + P + V_n - R), \quad \varepsilon_{57} = 3\nu + 2(K + Q) + 4R,$$
$$\varepsilon_{58} = \varepsilon_{60} = U + \mu + 3\nu + 2K + P + V_w + Q + 2R, \quad \varepsilon_{59} = U + \mu + 3\nu + 2(K + P + V_w),$$
$$\varepsilon_{61} = \varepsilon_{63} = 2(U + \mu) + 3\nu + J + 2K + L + 3P + 2V_n + 3V_w - Q - 2R,$$
$$\varepsilon_{62} = 2(U + \mu) + 3\nu + 2(K + P + V_w),$$
$$\varepsilon_{64} = 3(U + \mu + \nu) + 2(J + K + L) + 4(P + V_n + V_w - Q - R), \quad \varepsilon_{2,3} = \varepsilon_{6,7} = \sqrt{2}t,$$
$$\varepsilon_{12,15} = \varepsilon_{24,27} = (2t + R)/\sqrt{2}, \quad \varepsilon_{12,18} = (U - R)/2,$$
$$\varepsilon_{13,16} = \varepsilon_{25,28} = \varepsilon_{37,40} = \varepsilon_{49,52} = \sqrt{2}(t + R), \quad \varepsilon_{15,18} = -\varepsilon_{21,24} = R/\sqrt{2},$$
$$\varepsilon_{21,27} = (U + V_n - R)/2, \quad \varepsilon_{36,39} = \varepsilon_{48,51} = (2t + Q + 3R)/\sqrt{2},$$
$$\varepsilon_{39,42} = -\varepsilon_{45,48} = (Q + R)/\sqrt{2}, \quad \varepsilon_{45,51} = (U + L + V_n + V_w - Q - R)/2,$$
$$\varepsilon_{58,59} = \varepsilon_{62,63} = \sqrt{2}(t + Q + 2R). \quad (5.15)$$

The matrix elements of the block-diagonal unrenormalized 3-site Hamiltonian in the $\{|\psi_q\rangle\}$ basis are given above in Eq.(5.15), where $\langle\psi_q| - \beta\mathscr{H}_{i,j} - \beta\mathscr{H}_{j,k}|\psi_q\rangle = \varepsilon_q + 2G$ for the diagonal elements and $\langle\psi_q| - \beta\mathscr{H}_{i,j} - \beta\mathscr{H}_{j,k}|\psi_{\bar{q}}\rangle = \varepsilon_{q,\bar{q}}$ for the off-diagonal elements. Here, the matrix elements for the states connected by the exchange of the outer conduction electrons are obtained by multiplication with the eigenvalues u_3 of T_{ik}. The matrix elements $\eta_{q,\bar{q}}$ that enter the recursion relations via Eq.(5.17) below are obtained by exponentiating the block-diagonal Hamiltonian given here.

To extract the RG recursion relations, we consider the matrix elements $\gamma_{p,\bar{p}} \equiv \langle\phi_p|e^{-\beta'\mathcal{H}'_{i,k}}|\phi_{\bar{p}}\rangle$. With $\gamma_{9,9} = \gamma_{5,5}$, $\gamma_{10,10} = \gamma_{6,6}$, $\gamma_{11,11} = \gamma_{7,7}$, and $\gamma_{12,12} = \gamma_{8,8}$, 12 out of 16 diagonal elements are independent, and with $\gamma_{10,11} = \gamma_{11,10} = -\gamma_{7,6} = -\gamma_{6,7}$, only one of the 4 off-diagonal elements is independent, summing up to 13 independent matrix elements. Thus we obtain the renormalized interaction constants in terms of $\{\gamma\}$, defining $\gamma_p \equiv \gamma_{p,p}$ for the diagonal elements and $\gamma_0 \equiv \gamma_{6,7}$ for the only independent off-diagonal element:

$$
\begin{aligned}
t' &= \frac{1}{2}\ln\frac{\gamma_2}{\gamma_3}\ , \quad U' = \ln\frac{\gamma_1\gamma_6\gamma_0}{\gamma_2\gamma_5}\ , \quad \mu' = \frac{1}{2}\ln\frac{\gamma_2\gamma_3}{\gamma_1^2}\ , \quad \nu' = \frac{1}{2}\ln\frac{\gamma_2\gamma_5^2\gamma_7}{\gamma_1^2\gamma_3\gamma_6}\ , \\
J' &= \ln\frac{\gamma_1\gamma_4}{\gamma_2\gamma_3}\ , \quad K' = \frac{1}{2}\ln\frac{\gamma_1^2\gamma_3\gamma_6^2\gamma_{13}^2\gamma_{15}}{\gamma_2\gamma_5^4\gamma_7^2\gamma_{14}}\ , \quad L' = \ln\frac{\gamma_1\gamma_4\gamma_6^2\gamma_7^2\gamma_{13}\gamma_{16}}{\gamma_2\gamma_3\gamma_5^2\gamma_8^2\gamma_{14}\gamma_{15}}\ , \\
P' &= \ln\frac{\gamma_1\gamma_6}{\gamma_2\gamma_5\gamma_0}\ , \quad V'_n = \ln\frac{\gamma_2\gamma_3\gamma_5\gamma_8}{\gamma_1\gamma_4\gamma_6\gamma_7}\ , \quad V'_w = \ln\frac{\gamma_2\gamma_5^2\gamma_{14}}{\gamma_1\gamma_6^2\gamma_{13}}\ , \\
Q' &= \frac{1}{2}\ln\frac{\gamma_2\gamma_7^2\gamma_{14}}{\gamma_3\gamma_6^2\gamma_{15}}\ , \quad R' = \frac{1}{2}\ln\frac{\gamma_3\gamma_6}{\gamma_2\gamma_7}\ , \quad G' = \ln\gamma_1\ . \qquad (5.16)
\end{aligned}
$$

The matrix elements $\{\gamma\}$ of the exponentiated renormalized Hamiltonian are connected to the matrix elements, $\eta_{q,\bar{q}} \equiv \langle\psi_q|\mathrm{e}^{-\beta\mathscr{H}_{i,j}-\beta\mathscr{H}_{j,k}}|\psi_{\bar{q}}\rangle$, of the exponentiated unrenormalized Hamiltonian by Eq.(5.12). The matrix elements $\eta_{q,\bar{q}}$ can be obtained in terms of the unrenormalized interactions via exponentiating the unrenormalized Hamiltonian matrix whose elements are given in Eq.(5.15) above. Hence, the connection between $\{\gamma\}$ and $\{\eta\}$, that sets up the recursion relations between renormalized and unrenormalized interaction constants, reads

$$\begin{aligned}
\gamma_0 &= \eta_{12,18} + \eta_{21,27} + \eta_{36,42} + \eta_{45,51} \ , \\
\gamma_1 &= \eta_1 + \eta_3 + \eta_{10} + \eta_{16} \ , \\
\gamma_2 &= \eta_3 + \eta_7 + \eta_{13} + \eta_{28} \ , \\
\gamma_3 &= \eta_4 + \eta_5 + \eta_{19} + \eta_{22} \ , \\
\gamma_4 &= \eta_6 + \eta_8 + \eta_{25} + \eta_{31} \ , \\
\gamma_5 &= \eta_9 + \eta_{15} + \eta_{33} + \eta_{39} \ , \\
\gamma_6 &= \eta_{12} + \eta_{27} + \eta_{36} + \eta_{51} \ , \\
\gamma_7 &= \eta_{18} + \eta_{21} + \eta_{42} + \eta_{45} \ , \\
\gamma_8 &= \eta_{24} + \eta_{30} + \eta_{48} + \eta_{54} \ , \\
\gamma_{13} &= \eta_{34} + \eta_{40} + \eta_{57} + \eta_{59} \ , \\
\gamma_{14} &= \eta_{37} + \eta_{52} + \eta_{58} + \eta_{63} \ , \\
\gamma_{15} &= \eta_{43} + \eta_{46} + \eta_{60} + \eta_{61} \ , \\
\gamma_{16} &= \eta_{49} + \eta_{55} + \eta_{62} + \eta_{64} \ . \qquad (5.17)
\end{aligned}$$

5.3.2 Migdal–Kadanoff RG transformation in $d > 1$

Eqs.(5.15–5.17), constitute the RG recursion relations for $d = 1$, in the form $\vec{K}' = R(\vec{K})$, where $\vec{K} = (t, U, \mu, \nu, J, K, L, P, V_n, V_w, Q, R, G)$. In order to generalize to a higher dimension $d > 1$, we use the Migdal-Kadanoff procedure [113, 114],

$$\vec{K}' = b^{d-1} R(\vec{K}) \ , \qquad (5.18)$$

where $b = 2$ is the rescaling factor and R is the RG transformation in $d = 1$ for the interaction constants vector $\vec{K}$. This procedure is exact for d-dimensional hierarchical lattices [115, 116, 117] and a very good approximation for hypercubic lattices for obtaining complex phase diagrams.

Thus, the procedure described above, namely Eqs.(5.15–5.18) yields the recursion relations that will be determined numerically at each RG transformation step. Now, we use this procedure to obtain the global phase diagram of the SFKM, for which the results are presented in the next section.

We will follow the general rules described in the previous chapter. Each phase in the phase diagram has its own stable fixed point(s), which is called a phase sink (Table 5.3). All points within a phase flow to the sink(s) of that phase under successive RG transformations. Phase boundaries also have their own unstable fixed points (Table 5.4), where the relevant exponent analysis gives the order of the phase transition. Thus, the repartition of the RG flows determine the phase diagram in thermodynamic-field space. Matrix multiplications, along the renormalization-group trajectory, with the derivative matrix of the recursion relations relate the expectation values at the starting point of the trajectory to the expectations values at the phase sink [*cf.* Eq.(4.44)]. The latter are determined (Table 5.3) by the left eigenvector, with eigenvalue b^d, of the recursion matrix at the sink [*cf.* Eq.(4.42)], where $b = 2$ is the length-rescaling factor of the RG transformation. When the expectation values are thus calculated for the points of the phase boundary, the phase diagram in density space is determined [118].

5.4 Global phase diagram

The global phase diagram of SFKM is calculated, as described above, for the whole range of the interactions (t, U, μ, ν). The global phase diagram is thus 4-

Phase	The interaction constants K_α at the phase sinks											
sink	t	U	μ	ν	J	K	L	P	V_n	V_w	Q	R
$\delta_{\rm dd}$	0	0	$-\infty$	$-\infty$	0	0	0	0	0	0	0	0
$\delta_{\rm dD}$	0	∞	∞	$-\infty$	0	0	0	0	0	0	0	0
$\delta_{\rm Dd}$	0	∞	$-\infty$	∞	0	0	0	0	0	0	0	0
$\delta_{\rm DD}$	0	0	∞	∞	0	0	0	0	0	0	0	0
$\mathrm{CO_{dd}}$	∞	∞	$-\infty$	$-\infty$	∞	$-\infty$	∞	$-\infty$	$-\infty$	∞	∞	$-\infty$
$\mathrm{CO_{dD}}$	∞	∞	∞	$-\infty$	∞	$-\infty$	∞	∞	$-\infty$	∞	∞	∞
$\mathrm{CO_{Dd}}$	∞	∞	$-\infty$	∞	~ 50	$-\infty$	∞	$-\infty$	~ -20	∞	∞	$-\infty$
$\mathrm{CO_{DD}}$	∞	∞	∞	∞	~ 140	$-\infty$	∞	∞	~ -40	∞	∞	∞

Phase	The runaway coefficients K'_α/K_α at the phase sinks											
sink	t'/t	U'/U	μ'/μ	ν'/ν	J'/J	K'/K	L'/L	P'/P	V'_n/V_n	V'_w/V_w	Q'/Q	R'/R
$\delta_{\rm dd}$, $\delta_{\rm DD}$	–	–	4	4	–	–	–	–	–	–	–	–
$\delta_{\rm dD}$, $\delta_{\rm Dd}$	–	4	4	4	–	–	–	–	–	–	–	–
$\mathrm{CO_{dd}}$, $\mathrm{CO_{dD}}$	2	2	2	4	4/3	2	4/3	2	4/3	2	2	2
$\mathrm{CO_{Dd}}$, $\mathrm{CO_{DD}}$	2	2	2	4	1	2	4/3	2	1	2	2	2

Phase	The expectation values M_α at the phase sinks												Character
sink	$\langle\hat{t}\rangle$	$\langle\hat{U}\rangle$	$\langle\hat{\mu}\rangle$	$\langle\hat{\nu}\rangle$	$\langle\hat{J}\rangle$	$\langle\hat{K}\rangle$	$\langle\hat{L}\rangle$	$\langle\hat{P}\rangle$	$\langle\hat{V_n}\rangle$	$\langle\hat{V_w}\rangle$	$\langle\hat{Q}\rangle$	$\langle\hat{R}\rangle$	
$\delta_{\rm dd}$	0	0	0	0	0	0	0	0	0	0	0	0	dilute - dilute
$\delta_{\rm dD}$	0	0	2	0	1	0	0	0	0	0	0	0	dilute - dense
$\delta_{\rm Dd}$	0	0	0	2	0	1	0	0	0	0	1	2	dense - dilute
$\delta_{\rm DD}$	0	2	2	2	1	1	1	2	2	2	-1	-2	dense - dense
$\mathrm{CO_{dd}}$	$-a$	0	a	0	0	0	0	0	0	0	0	0	dilute - CO dilute
$\mathrm{CO_{dD}}$	$-a$	0	b	0	c	0	0	0	0	0	0	0	dilute - CO dense
$\mathrm{CO_{Dd}}$	$-a$	a	a	2	0	1	0	a	0	a	1	2	dense - CO dilute
$\mathrm{CO_{DD}}$	$-a$	b	b	2	c	1	c	b	$2c$	b	d	$2d$	dense - CO dense

Table 5.3: Interaction constants K_α, runaway coefficients K'_α/K_α, and expectation values $M_\alpha = \langle\hat{K_\alpha}\rangle$, at the phase sinks. Here, $\hat{K}_\alpha$ are used as abbreviations for the conjugate operators for interaction constants K_α, *e.g.*, $\langle\hat{t}\rangle = \langle c_i^\dagger c_j + c_j^\dagger c_i\rangle$, $\langle\hat{U}\rangle = \langle n_i w_i + n_j w_j\rangle$, *etc.* The non-zero hopping expectation value is $-a = -0.629050$ (Other abbreviations used are $b = 2-a$, $c = 1-a$, $d = -1+2a$). In the subscripts in the first columns and at each side of the hyphen in the last column of the last table, the left and right entries refer to the localized and conduction electrons, respectively, as dilute (d) or dense (D), while CO refers to charge-ordered.

dimensional, and $1/t$ is taken as the temperature variable. We present constant-U-constant-$t/|U|$ cross sections of the global phase diagram in terms of the localized and conduction electron chemical potentials, $\nu/|U|$ and $\mu/|U|$, and densities, $\langle w_i \rangle$ and $\langle n_i \rangle$. Our presentation will be in five subsections: The first subsection gives the $t = 0$ classical submodel, while the next three subsections are devoted to small, intermediate, and large values of $|U|$. We will present the general evolution of the phase diagram with increasing t in a final subsection. But, before we present the global phase diagram, here we would like to provide the properties of the phase sinks and phase boundaries in Tables 5.3 and 5.4 respectively.

Phase boundary	Boundary type	Interaction constants K_α at the boundary fixed points											
		t	U	μ	ν	J	K	L	P	V_n	V_w	Q	R
CO_{dD}/CO_{Dd}	1st order	∞	$-\infty$	∞	$-\infty$	∞	∞	∞	$-\infty$	$-\infty$	∞	∞	$-\infty$
CO_{dd}/δ_{dd}	2nd order	∞	∞	$-\infty$	$-\infty$	∞	$-\infty$	∞	$-\infty$	$-\infty$	∞	∞	$-\infty$
CO_{dD}/δ_{dD}	2nd order	∞	∞	∞	$-\infty$	∞	$-\infty$	∞	$-\infty$	∞	∞	∞	$-\infty$
CO_{Dd}/δ_{Dd}	2nd order	∞	∞	$-\infty$	∞	∞	$-\infty$	∞	$-\infty$	$-\infty$	∞	∞	$-\infty$
CO_{DD}/δ_{DD}	2nd order	∞	∞	∞	∞	∞	$-\infty$	∞	∞	$-\infty$	∞	∞	∞
CO_{dd}/CO_{dD}	2nd order	∞	∞	$-\infty$	$-\infty$	∞	$-\infty$	∞	$-\infty$	$-\infty$	∞	∞	$-\infty$
CO_{Dd}/CO_{DD}	2nd order	∞	∞	$-\infty$	∞	∞	$-\infty$	∞	$-\infty$	∞	∞	∞	$-\infty$

Phase boundary	Boundary type	Additional property	Relevant eigenvalue exponent y_1
CO_{dD}/CO_{Dd}	1st order	$2\mu - 2\nu + J - K - Q - 2R = 0$	3
CO_{dd}/δ_{dd}	2nd order	$t + \mu = 1.744253$	0.273873
CO_{dD}/δ_{dD}	2nd order	$t - \mu - J = 1.744253$	0.273873
CO_{Dd}/δ_{Dd}	2nd order	$t + U + \mu + P + V_w = 1.744253$	0.273873
CO_{DD}/δ_{DD}	2nd order	$t - U - \mu - J - L - P - 2V_n - V_w + 2Q + 4R = 0$	0.273873
CO_{dd}/CO_{dD}	2nd order	$2\mu + J = 0$	1.420396
CO_{Dd}/CO_{DD}	2nd order	$2U + 2\mu + J + L + 2P + 2V_n + 2V_w - 2Q - 4R = 0$	1.420396

Table 5.4: Interaction constants K_α, additional properties, and relevant eigenvalue exponents y_1 at the phase boundary fixed points. For first-order phase transitions, $y_1 = d = 3$, while for second-order phase transitions, $0 < y_1 < d - 1 = 2$.

5.4.1 The classical submodel $t = 0$

Setting the quantum effect to zero, $t = 0$, yields the classical submodel, closed under the RG flows. We do not need to extend the Hamiltonian with extra pa-

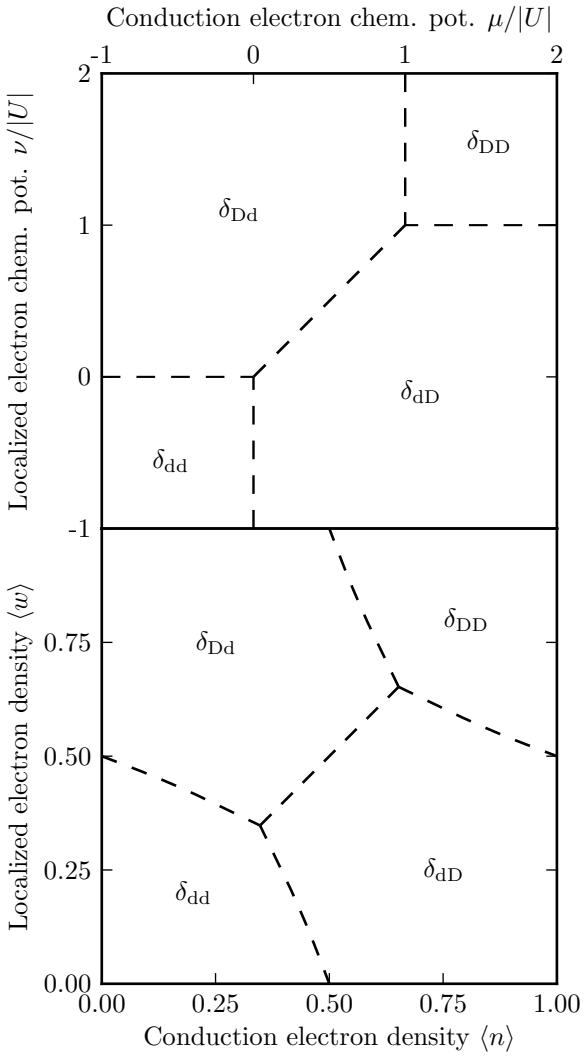

Figure 5.3: RG flow basins of the $t = 0$ classical submodel, in the chemical potentials (upper panel) and densities (lower panel) of the localized and conduction electrons. The dashed lines are not phase transitions, but smooth changes between the four different density regions of the disordered δ phase.

rameters, rather only an introduction of additive interaction assures a closed RG transformation. The global flow basins in $\nu/|U|$ and $\mu/|U|$ are the same for all U, given in Fig.5.3 above. There exist four regions within this submodel, which are localized-dilute-conduction-dilute, localized-dilute-conduction-dense, localized-dense-conduction-dilute, and localized-dense-conduction-dense regions, denoted

by $\delta_{\rm dd}$, $\delta_{\rm dD}$, $\delta_{\rm Dd}$, and $\delta_{\rm DD}$.[3] In the RG flows, each δ region is the basin of attraction of its own sink. The dashed lines between the different regions are not phase boundaries, but smooth transitions (such as the supercritical liquid – gas or up-magnetized – down-magnetized transitions), which are controlled by zero-coupling null fixed points.

It should be noted that the Suzuki–Takano and Migdal–Kadanoff methods are actually exact for this classical submodel, and yield exactly the same picture as obtained in [190].

5.4.2 The small $|U|$ regime

In this subsection, we present our results for $|U| = 0.1$, representative of the weak-interaction regime. The $t = 0$ phase diagram of Fig.5.3 evolves under the introduction of quantum effects via a non-zero hopping strength t. It should be noted that increasing the dimensionless Hamiltonian parameter t is equivalent to reducing temperature, as in all RG studies. The first effect is the decrease and elimination (Fig.5.4, left panels) of the (smooth) passage between the $\delta_{\rm Dd}$ and $\delta_{\rm dD}$ regions. With this elimination, all four regions meet at $\nu/|U| = \mu/|U| = 0.5$ and $\langle w_i \rangle = \langle n_i \rangle = 0.5$, the half-filling of both localized and conduction electrons. Further increasing t, (reducing temperature) four new, charge-ordered (CO) phases emerge at $t \simeq 0.6$. The CO phases occur at and near half-filling of conduction electrons for the entire range of localized electron densities. The CO phases grow with increasing t until saturation at high t (low temperature) (Fig.5.4, right panels).

All of the new CO phases have non-zero hopping density $\langle c_i^\dagger c_j + c_j^\dagger c_i \rangle = -a \equiv -0.629050$ at their phase sinks. Recall that the expectation values at the sinks are evaluated according to Eq.(4.42). In the CO phases, the hopping strength t diverges to infinity under repeated RG transformations (whereas in the δ phases, t vanishes under repeated RG transformations). The localized electron density is $\langle w_i + w_j \rangle = 0$ at the sinks of $\rm CO_{dd}$ and $\rm CO_{dD}$, while $\langle w_i + w_j \rangle = 2$ at the sinks of $\rm CO_{Dd}$ and $\rm CO_{DD}$, which throughout the corresponding phases calculationally translates [118] as low (d) and high (D) localized electron densities, respectively.

[3] In phase subscripts throughout this thesis, the first and second subscripts respectively describe localized and conduction electron densities, as dilute (d) or dense (D).

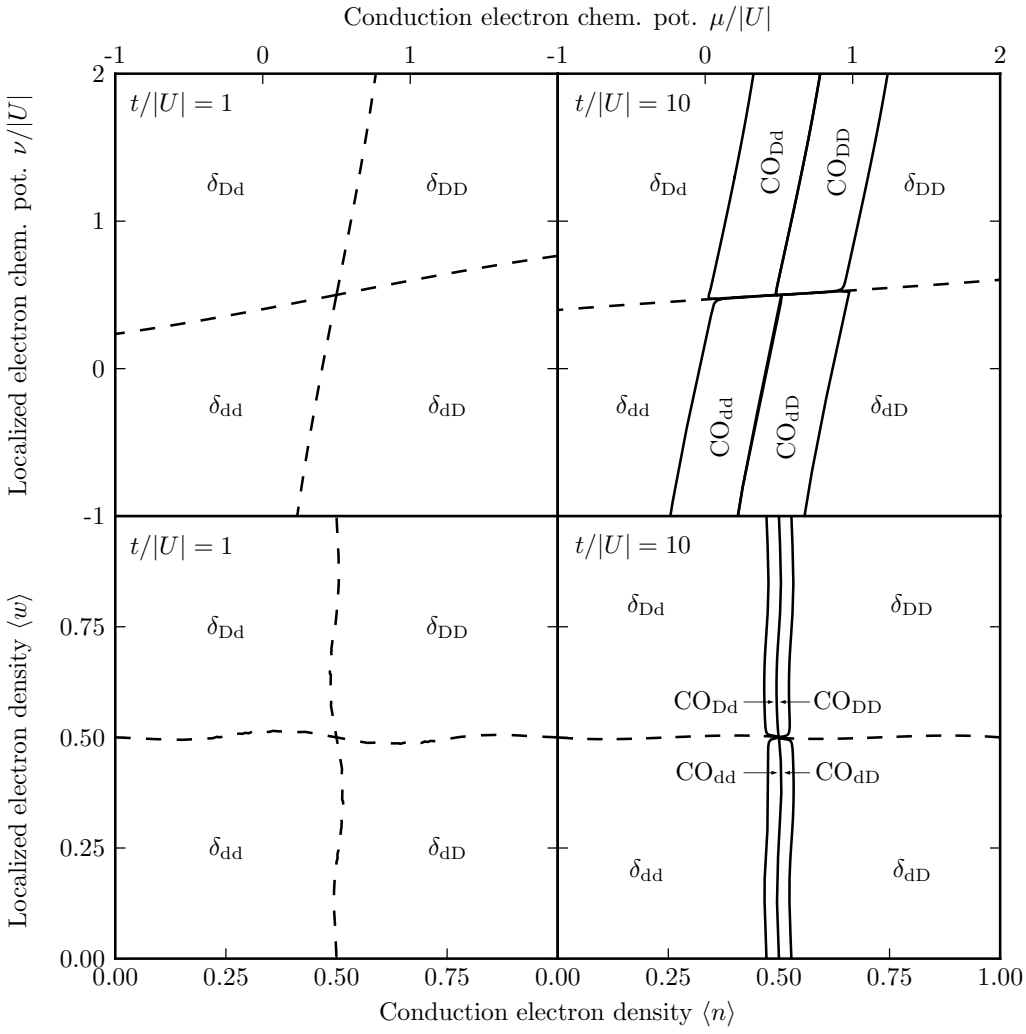

Figure 5.4: Constant $t/|U|$ cross-sections of the phase diagram for interaction $|U| = 0.1$, in the chemical potentials (upper panels) and in the densities (lower panels) of the localized and conduction electrons. In phase subscripts throughout this paper, the first and second subscripts respectively describe localized and conduction electron densities, as dilute (d) or dense (D). The full lines are second-order phase transitions. The dashed lines are not phase transitions, but smooth changes between the different density regions of the disordered δ phase. The charge-ordered phases are denoted by CO. Details are shown in Fig.5.5. Thus, for low values of the interaction, all phase boundaries are second order and there is no phase coexistence (phase separation).

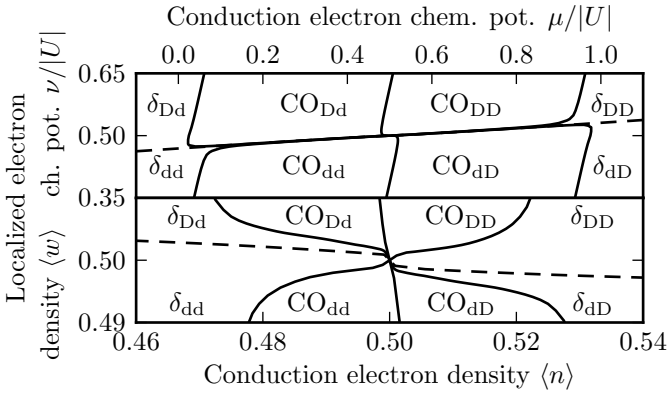

Figure 5.5: Zoomed portion of Fig.5.4, *i.e.*, of the $|U| = 0.1$, $t/|U| = 10$ phase diagram.

Recall that on phase labels, CO and δ, the first (second) subscripts describe localized (conduction) electron densities.

The conduction electron density is $\langle n_i + n_j \rangle = a = 0.629050$ at the sinks of $\rm CO_{dd}$ and $\rm CO_{Dd}$, while $\langle n_i + n_j \rangle = 2 - a = 1.370950$ at the sinks of $\rm CO_{dD}$ and $\rm CO_{DD}$. The nearest-neighbor conduction electron number correlation is $\langle n_i n_j \rangle = 0$ at the sinks of $\rm CO_{dd}$ and $\rm CO_{Dd}$, while $\langle n_i n_j \rangle = 1 - a = 0.370950$ at the sinks of $\rm CO_{dD}$ and $\rm CO_{DD}$. Consequently, for conduction electrons, if a given site is occupied, its nearest-neighbor site is empty at the sinks of $\rm CO_{dd}$ and $\rm CO_{Dd}$. The $\rm CO_{dD}$ and $\rm CO_{DD}$ phases are connected to the $\rm CO_{dd}$ and $\rm CO_{Dd}$ phases by particle-hole symmetry. Thus, in the CO phases, the lattice can be divided into two sublattices with different electron desities. The behavior at the CO sinks therefore indicates charge-ordering phases at finite temperatures, as also previously seen in ground-state studies [182, 191, 192]. Note that this charge-ordering is a purely quantum mechanical effect caused by hopping, since the SFKM Hamiltonian [Eq.(5.4)] studied here does not contain an interaction between electrons at different sites.

In the small $|U|$ regime, all phase boundaries of the CO phases are second order. As seen in the expanded Fig.5.5, all four CO phases and all four regions of the δ phase (as narrow slivers) meet at at $\nu/|U| = \mu/|U| = 0.5$ and $\langle w_i \rangle = \langle n_i \rangle = 0.5$, the half-filling point of both localized and conduction electrons. All characteristics of the sinks and boundary fixed points are given in Tables 5.3 and 5.4.

5.4.3 The intermediate $|U|$ regime

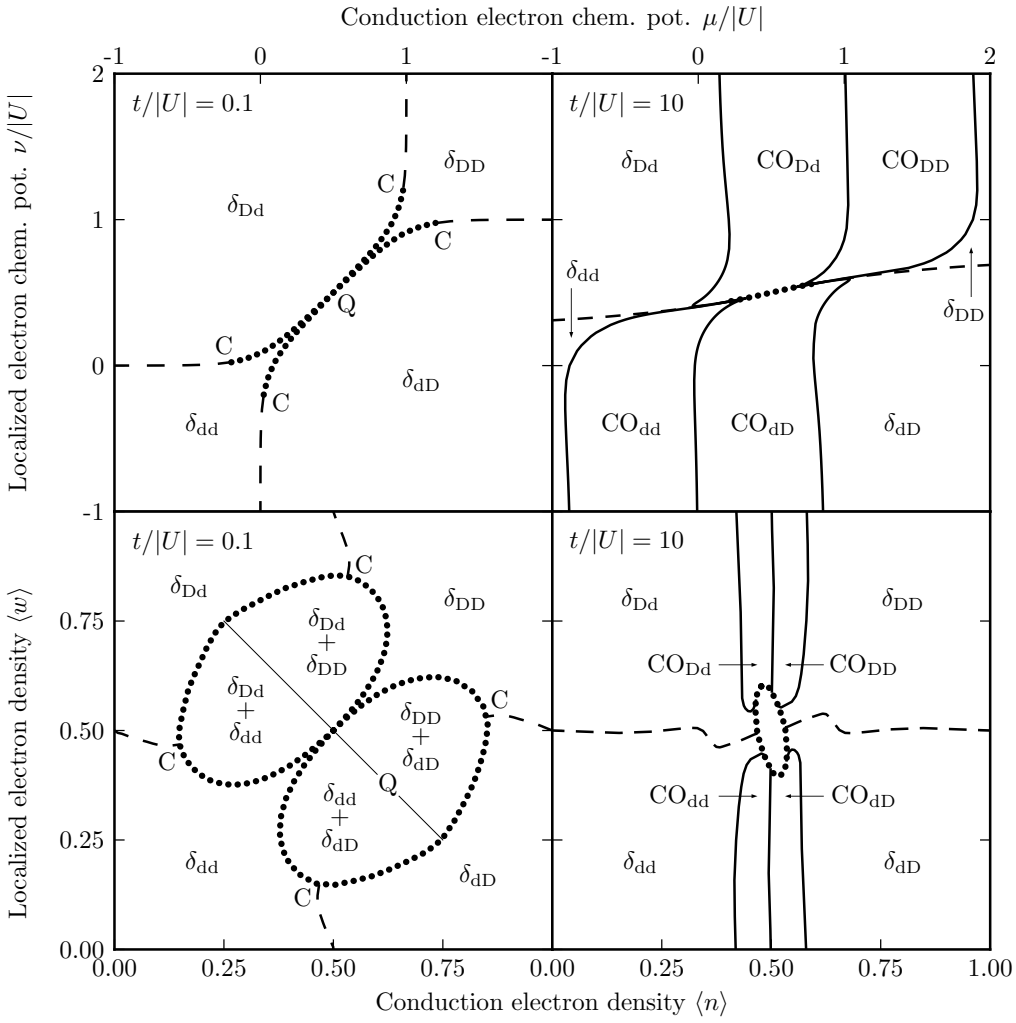

Figure 5.6: Constant $t/|U|$ cross-sections of the phase diagram for $|U| = 1$, in the chemical potentials (upper panels) and densities (lower panels) of the localized and conduction electrons. The dotted lines are first-order phase transitions. Phase separation, *i.e.*, phase coexistence occurs inside the dotted boundaries, as identified in the figure. The details of the coexistence region in the lower-right panel are given in Fig.5.7. The thick full lines are second-order phase transitions. The quadruple point Q tie line is shown as the thin straight line. The dashed lines are not phase transitions, but smooth changes between the different density regions of the disordered δ phase.

In this subsection, phase diagram for $|U| = 1$, representative of the intermediate-interaction regime, is presented. In Fig.5.6 above, we give constant $t/|U|$ cross-sections. First-order phase boundaries appear in the central region of the phase diagram, at and near the half-filling of both localized and conduction electrons.

For low t values (left panels of Fig.5.6), equivalent to high temperatures, two first-order phase boundaries, bounded by four critical points C, pinch at a quadruple point Q. In the (left-lower) density-density phase diagram, four phase separation (coexistence) regions mark the first-order phase transitions. Inside these regions, coexistence (phase separation) occurs between the phases on each side of these regions, as indicated on the figure. The tie line of the quadruple point is shown as the straight line. All four δ phases coexist (phase separate) on this line.

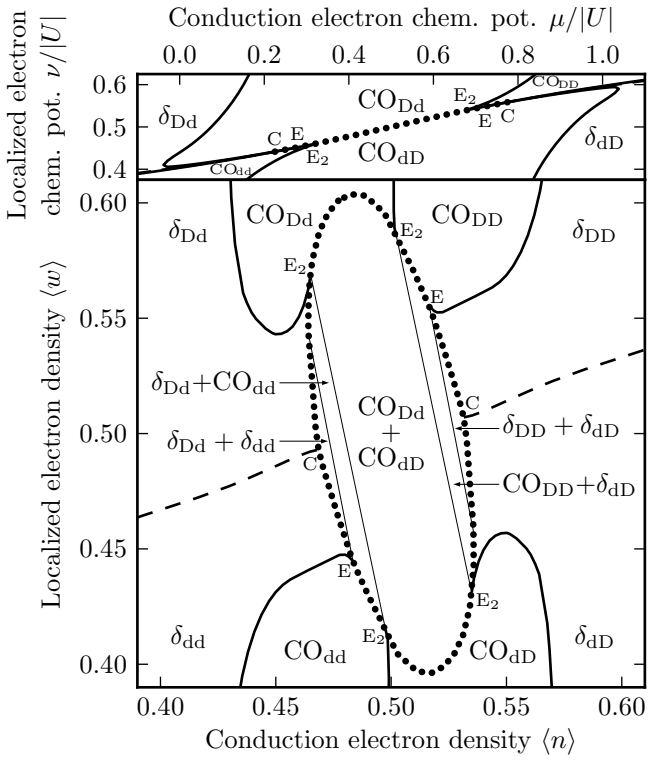

Figure 5.7: Zoomed portion of Fig.5.6, for the $|U| = 1$, $t/|U| = 10$ phase diagram. The coexistence tie lines of the critical endpoints E and of the double critical endpoints E_2 are shown. Inside each region delimited by dotted lines and the endpoint tie lines, phase separation, *i.e.*, phase coexistence occurs between phases as identified on this figure.

As t increases (temperature decreases), the four charge-ordered CO phases appear again at $t \simeq 0.6$. The CO phases again occur at and near half-filling of conduction electrons for the entire range of localized electron densities. The second-order transition lines bounding the CO phases terminate at two critical endpoints E [193] and two double critical endpoints E_2 on the first-order line in the central region (Fig.5.7). Thus, first-order transitions and phase separation occur between the pairs of δ_{Dd} and δ_{dd}, δ_{Dd} and $\mathrm{CO}_{\mathrm{dd}}$, $\mathrm{CO}_{\mathrm{Dd}}$ and $\mathrm{CO}_{\mathrm{dD}}$, $\mathrm{CO}_{\mathrm{DD}}$ and δ_{dD}, δ_{DD} and δ_{dD} phases, as indicated on Fig.5.7, at and near the half-filling of both localized and conduction electrons.

5.4.4 The large $|U|$ regime

The evolution of the global phase diagram, as the interaction strength is increased, is seen in the phase diagrams in Fig.5.8. The CO phases emerge again at $t \simeq 0.6$. With increasing t (decreasing temperature), the CO phases grow, until saturation seen in Fig.5.8. The topology of the phase diagram with five phases stays the same for all $t \gtrsim 0.6$.

The constant $t/|U|$ cross-sections of the phase diagram are given in Fig.5.8. For $U = 1.5$, the double critical endpoints E_2 have split into pairs of simple critical endpoints E, resulting in six separate critical endpoints. For $U = 1.845628$, the inner two critical endpoints have merged into a double critical endpoint. For $U = 10$, the double critical endpoint has split into two critical endpoints and the critical lines in the low-density and high-density localized electrons regions have disconnected from each other. In this strong interaction limit, the homogenous (non-phase-separated) charge-ordered phase occur again at and near half-filling of conduction electrons, but at the low- or high-density limit of the localized electrons. Away from these limits, the charge-ordered phases occur in coexistence (phase-separated from) the disordered phases. At and near the half-filling of both localized and conduction electrons, the coexistence of the disordered phases δ_{Dd} and δ_{dD} occurs. Two sets of three critical lines terminate in separate endpoints, as seen in the zoomed Fig.5.10. In this case, a characteristic shape of the density phase diagrams, which we dub "*chimaera*" coexistence, emerges. In the chimaera phase

diagram, coexistence can be found for essentially the entire range of conduction electrons densities or for most of the range of localized electron densities.

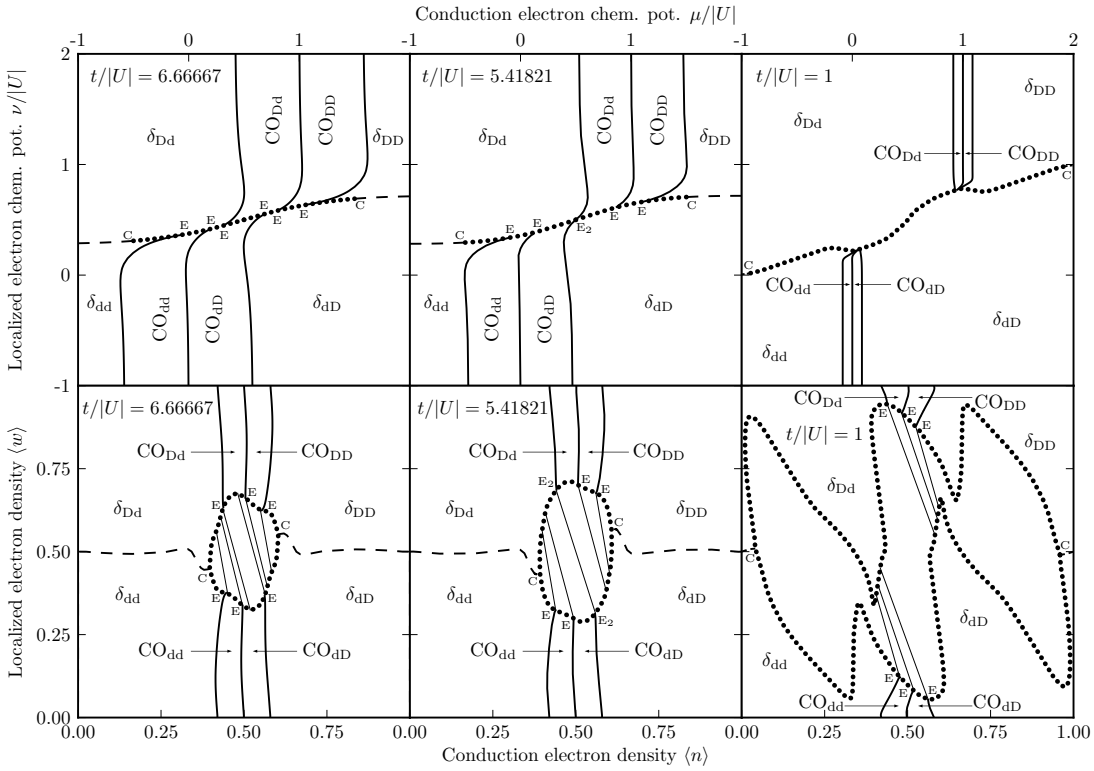

Figure 5.8: Constant $t/|U|$ cross-sections of the phase diagram for interactions $|U| = 1.5$, 1.845628, 10 (left to right), in the chemical potentials (upper panels) and densities (lower panels) of the localized and conduction electrons. The dotted and thick full lines are respectively first- and second-order phase transitions. The tie lines of the critical endpoints E and of the double critical endpoints E_2 are shown by thin straight lines. Phase separation, *i.e.*, phase coexistence occurs within the regions bounded by the dotted lines and the tie lines, this coexistence being between the phases seen on each side of the dotted lines. The dashed lines are not phase transitions, but smooth changes between the different density regions of the δ phase.

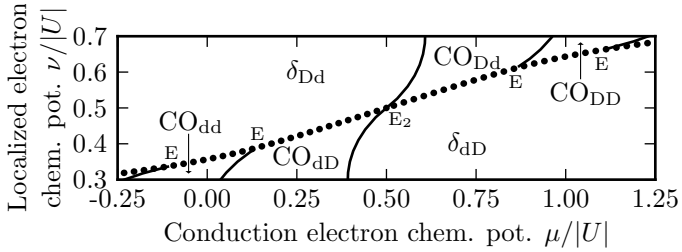

Figure 5.9: Zoomed portions of Fig.5.8, for the $|U| = 1.845628$, $t/|U| = 5.41821$ phase diagram.

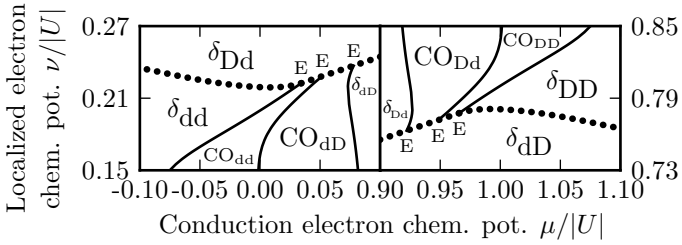

Figure 5.10: Two zoomed portions of Fig.5.8, for the $|U| = 10$, $t/|U| = 1$ phase diagram.

5.4.5 Evolution of phase diagrams with varying t

Finally, we present the evolution of the global phase diagram, as the hopping strength is increased, for the $|U| = 1$ case. In Fig.5.11 we begin with $t = 0.6$, where the CO phases emerge. The topology of this phase diagram stays the same with increasing t (decreasing temperature) until $t = 1$. Here, the four δ phases meet at the half-filling point for both localized and conduction electrons. Phase separations occur between different δ phases as seen in the figure. Two-phase coexistence regions are obvious. The triangles of tie lines in the density phase diagrams denote three-phase coexistence regions for $t/|U| = 0.6$ and 1. Inside the upper-right triangles $\delta_{\rm dd}$, $\delta_{\rm Dd}$, and $\delta_{\rm DD}$ coexist, while inside the lower-left triangles $\delta_{\rm dd}$, $\delta_{\rm dD}$, and $\delta_{\rm DD}$ coexist. In these two figures ($t/|U| = 0.6$, 1), $\delta_{\rm dd}$ and $\delta_{\rm DD}$ coexist on the common tie line of the two triangles. Note that the two phase separation regions that the CO phases touch (one between $\delta_{\rm Dd}$ and $\delta_{\rm DD}$, the other between $\delta_{\rm dd}$ and $\delta_{\rm dD}$) shrink with increasing t, while, in the meantime, the CO phases grow.

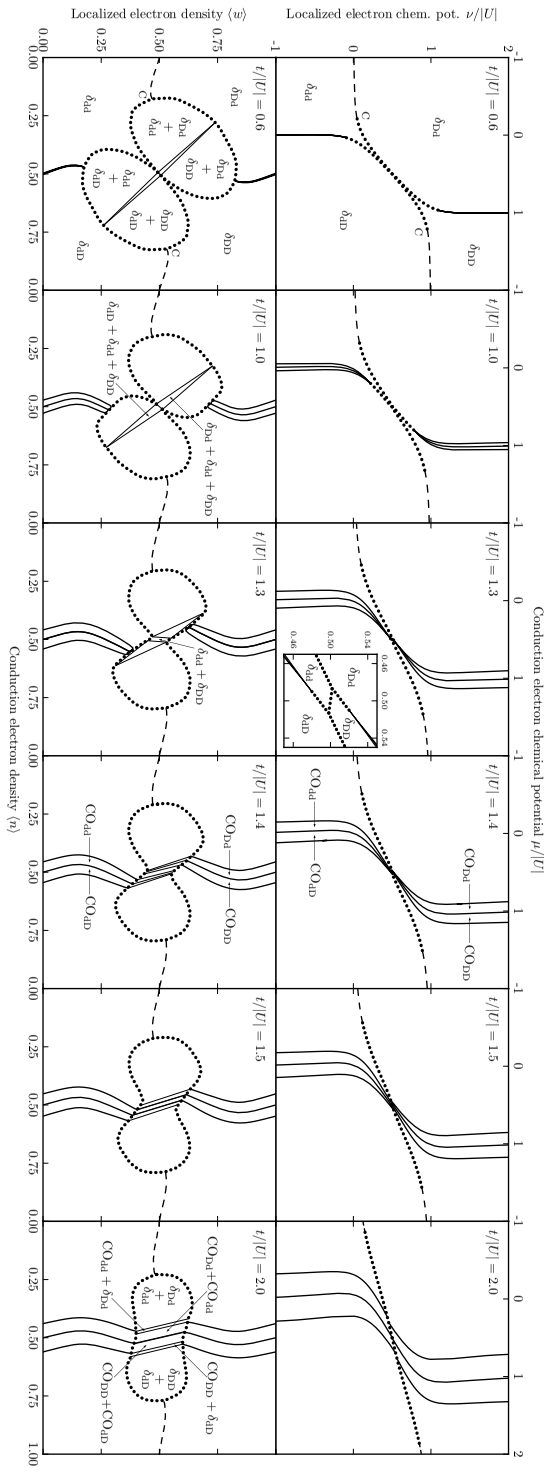

Figure 5.11: Evolution of the $|U| = 1$ phase diagram of constant $t/|U|$ (increasing from top to bottom) cross-sections in the chemical potentials (right panels) and densities (left panels) of the localized and conduction electrons. Lines are as in Fig.5.8. See text for details.

As one further increases t (decreases temperature), at some point between $t/|U| = 1$ and $t/|U| = 1.3$ a first order phase transition between δ_{dd} and δ_{DD} ruptures the phase diagram. This first-order phase boundary is seen in the $t/|U| = 1.3$ phase diagram and in the inset showing the zoomed half-filling region. As a result, the two-phase coexistence tie line opens up and a phase separation (between δ_{dd} and δ_{DD}) region intervenes between the three-phase triangular coexistence regions.

As the hopping strength further increases, CO phases grow enough to completely capture the two shrinking phase separation regions (one between δ_{Dd} and δ_{DD}, the other between δ_{dd} and δ_{dD}). As seen from the $t/|U| = 1.4$ phase diagrams, these two coexistence regions are completely vanished and instead, various phase separation regions between the CO and δ phases take place.

After this point, increasing t (decreasing temperature) results in CO phases moving towards and passing through the half-filling point for conduction electrons until a saturation (see phase diagrams for $t/|U| = 1.5$ and 2). Along the way, various critical endpoints and double critical endpoints emerge and vanish. The saturated picture depends on the strength of the on-site Coulomb repulsion, and a higher value of $|U|$ results in more detached CO phases, as was discussed in the previous subsections.

5.5 Conclusion

Therefore, we have obtained the global phase diagram of the $d = 3$ SFKM, which exhibits a fairly rich collection of phase diagram topologies:

For the $t = 0$ classical submodel, we have obtained disordered (δ) regions, dilute and dense separately for localized and conduction electrons, but no phase transition between them. The repartition of these regions, delimited by RG flows, quantitatively stays the same for the whole $|U|$ range and is exactly as obtained in Ref. [190]. For the whole $|U|$ range and $0 < t \lesssim 0.6$, the classical submodel phase diagram is perturbed in such a way that regions δ_{dd} and δ_{DD} intercede between regions δ_{dD} and δ_{Dd}, resulting in the δ_{dD} to δ_{Dd} passage to shrink and disappear.

All δ regions have vanishing hopping density at their corresponding sinks. For the whole $|U|$ range, upon increasing t (lowering temperature), at $t \simeq 0.6$ four new phases (CO) emerge with non-zero hopping density of $-a = -0.629050$ at their sinks. These CO phases are also either dilute or dense, separately, in the localized and conduction electrons ($\mathrm{CO_{dd}}$, $\mathrm{CO_{dD}}$, $\mathrm{CO_{Dd}}$, and $\mathrm{CO_{DD}}$) and are all charge ordered in the conduction electrons, a wholly quantum mechanical effect. In these CO phases the bipartite lattice is divided into two sublattices of alternating electron density. The CO phases occur at or near the half-filling of conduction electrons. The phase diagrams with all five phases for $t \gtrsim 0.6$ exhibit several different topologies, for the small, intermediate, and large $|U|$ regimes:

For the small $|U|$ (weak-interaction) regime, all phase boundaries are second order. All five phases meet at $\nu/|U| = \mu/|U| = 0.5$ and $\langle w_i \rangle = \langle n_i \rangle = 0.5$, the half-filling point of both localized and conduction electrons.

For the intermediate $|U|$ (intermediate-interaction) regime, a first-order phase boundary emerges in the central region of the phase diagram. This first-order boundary is centered at $\nu/|U| = \mu/|U| = 0.5$ and is bounded by two critical points C. The second-order lines bounding the CO phases terminate at critical endpoints E and double critical endpoints $\mathrm{E_2}$ on the first-order boundary. Due to this first-order phase transition at and near the half-filling of both localized and conduction electrons, a rich variety of phase separation (phase coexistence) occurs, as indicated on Figs. 5.6, 5.7, 5.8.

For the large $|U|$ (strong-interaction) regime, as $|U|$ is increased, the critical endpoints pass through each other by merging and unmerging as double critical endpoints. For large $|U|$, the $\mathrm{CO_{Dd}}$ and $\mathrm{CO_{DD}}$ phases are detached from the $\mathrm{CO_{dd}}$ and $\mathrm{CO_{dD}}$ phases, forming two separate bundles, at high- and low-densities of localized electrons respectively. First-order transitions occur between the variously dense and dilute δ. The global phase diagram underpinning all of these cross-sections is decidedly quite complex.

This compexity further levels up once we consider the evolution of the phase diagram with varying the hopping strength. We investigated the intermediate-interaction, $|U| = 1$, case in particular (*cf.* Fig. 5.11). Here, in the interval of $0.6 \lesssim t/|U| \lesssim 1.3$ three-phase coexistence regions emerge between two separate δ phase sets. The three-phase coexistence regions are divided by a two-phase coexistence line in the density phase diagram for $0.6 \lesssim t/|U| \lesssim 1$, and by a two-phase coexistence region for $1 \lesssim t/|U| \lesssim 1.3$.

Note that these phase diagram cross-sections in chemical potentials for $t \gtrsim 0.6$ are very similar to the ones reported in Refs. [174, 191, 192], while the classical submodel phase diagram is exactly the same as in [190]. Furthermore, the calculated phase diagrams exactly reflect the symmetries of the SFKM Hamiltonian. Therefore, we can assure that the RG method we used to calculate the global phase diagram implements a good approximation for the whole range of parameters.

As a future study, we can also calculate other related measurable physical quantities, such as specific heat, internal energy, *etc.*, in the RG framework [106, 107, 108], which will require only a minor effort over the one we accomplished already, and consequently, can relate theoretical work to experiments more tightly. Here, we should note that the charge ordered phases we obtained within the SFKM are experimentally verified for strongly correlated electron systems. The close interplay between the charge ordering (occuring around half-filling) and the high-temperature superconductivity or colossal magnetoresistance has been the subject of condensed matter experimental research, particularly in the last decade[4] [183, 184, 185, 186, 187, 188, 189, 194, 195]. Therefore, a better physical un-

[4]High-temperature superconductivity and colossal magnetoresistance do not only manifest charge ordering, but also orbital and magnetic ordering.

derstanding of the charge ordered phases would yield a theoretical insight on high-temperature superconductors or colossal magnetoresistors. We would like to provide the experimental pictures of charge ordering in $La_{1-x}Ca_xMnO_3$ and $Ca_{2-x}Na_xCuO_2Cl_2$ systems in Fig. 5.12.

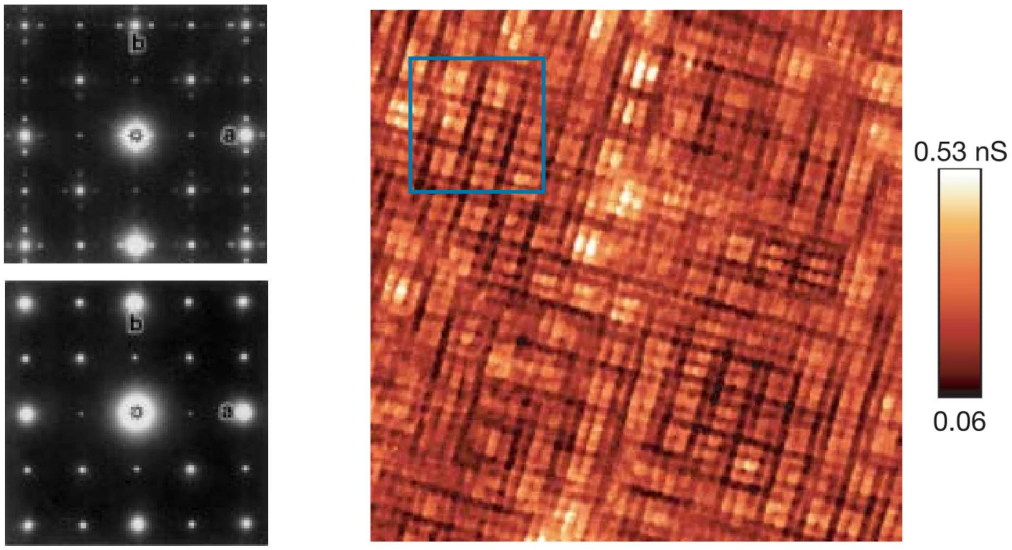

Figure 5.12: Charge ordering (CO) experimentally observed in $La_{1-x}Ca_xMnO_3$ ($x = 0.67$, left, after [183]), where CO is seen as superlattice spots at 200 K (top) in addition to the main spots seen at 300 K (bottom); and in $Ca_{2-x}Na_xCuO_2Cl_2$ ($x = 0.10$, right, after [195]), where the STM dI/dV conductance map taken at 24 meV and 100 mK exhibiting the 4×4 CO.

We can also consider bosonic cases seperately for each conduction and localized particles that can be experimentally realized by ultra-cold atomic systems [196]. These considerations as well as other extensions can be the subject of future studies.

Another model of our interest is the widely studied bosonic Hubbard model (Bose–Hubbard model). This model incorporates only one type of particle, which makes it easier to study compared to bosonic cases of the FKM. However, practically we should limit the model with a finite number of bosons at a lattice site, since calculation of the renormalized and unrenormalized Hamiltonian matrices are impossible for an unlimited number of bosons at a site. Our prediction is

that limiting the maximum value of bosons at a site to three (or even to two) will be enough to capture the first two cascades of the phase diagram of the model. A comparison with the well-known phase diagram of the model, that is widely studied in the literature, will provide further reliability of our method.

Chapter 6

OTHER DIRECTIONS

This chapter will mention briefly about other work of the present author during doctoral studies. These include hard-spin mean-field theory of $\pm J$ spin glass model, sequence alignment by simulated annealing, and molecular dynamics of water flow through carbon nanotubes. Each study will be discussed in a separate section below.

6.1 Hard-spin mean-field theory of $\pm J$ spin-glass model

The dimensionless Hamiltonian of the $\pm J$ spin glass model is given by

$$-\beta\mathscr{H} = \sum_{\langle ij \rangle} J_{ij} s_i s_j + H \sum_i s_i \ , \tag{6.1}$$

where $s_i = \pm 1$ is a classical spin-$\frac{1}{2}$ variable for the local magnetic degree of freedom, J_{ij} is a local exchange interaction between lattice sites i and j, and H is the uniform external magnetic field. In order to reflect the frustation nature of spin-glasses, J_{ij} is definded to be antiferromagnetic for some bonds, with probability p, and ferromagnetic for the rest, with probability $1-p$. Thus, for the probabilty distribution of the ineraction, we write

$$P(J_{ij}) = p\delta(J_{ij} + J) + (1-p)\delta(J_{ij} - J) \tag{6.2}$$

with $0 \leq p \leq 1$ and $J \sim 1/T$.

We use the hard-spin mean-field theory [197, 198, 199, 200, 201, 202, 203, 204, 205, 206, 207, 208, 209, 210, 211], to obtain the thermodynamic behavior of the model. The self-consistent equation for local magnetizations, m_i in hard-spin mean-field theory is given by

$$m_i = \sum_{\{s_j\}} \left[\prod_j P(m_j, s_j) \right] \tanh \left[\sum_j J_{ij} s_j + H \right] \ , \tag{6.3}$$

where the sum-j and product-j are over the nearest-neighboring sites to i, and the single-site probability distribution is given by

$$P(m_j, s_j) = \frac{1 + m_j s_j}{2} \ . \tag{6.4}$$

Using a 3-dimensional simple cubic lattice of $L \times L \times L$ sites with periodic boundary conditions, the problem is reduced to solve L^3-coupled equations of the type Eq.(6.3), and the solutions are obtained numerically by iteration up to a desired saturation error.

The hysteresis curves for the system above mark paramagnetic, ferromagnetic and spin-glass behavior. In the paramagnetic phase, the hysteresis area vanishes.

In ferromagnetic phase a jump occurs at the coercive field, H_c, while a continuous hysteresis curve denotes a spin-glass phase. We obtain these features and an expected phase diagram in J-p plane for the model, via the hard-spin mean-field theoretical approach. In Fig. 6.1 below, we present these three distinct hysteretic behavior, for representative values of J and p.

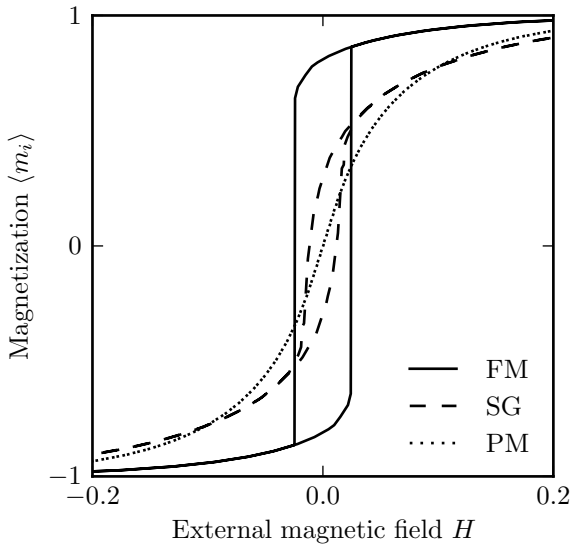

Figure 6.1: Diverse hysteretic behavior of the $\pm J$ model for representative ferromagnetic ($J = 0.50$, $p = 0.16$), spin-glass ($J = 0.50$, $p = 0.28$), and paramagnetic ($J = 0.20$, $p = 0.22$) cases, denoted by full, dashed, and dotted lines respectively. Hysteresis curves are obtained for a saturation error of $\epsilon(\langle m_i \rangle) = 10^{-6}$.

The saturation error mentioned above, in fact, determines the sweep rate of the external magnetic field: a higher saturation error corresponds to a faster sweep rate, and *vice versa*. During the time this thesis was being written, we were performing calculations for investigating the dependence of the hysteresis area on the magnetic field sweep rate. Another calculation concerns the properties of dynamical scaling with both J and p in the spin glass phase.

6.2 Sequence alignment using simulated annealing

Collaborating with Can Güven (University of Maryland), we applied simulated annealing to amino acid sequence alignment, a fundamental problem in bioinformatics, particularly relevant to evolution [212]. The Metropolis algorithm introduced in Ref. [213] was developed by Kirkpatrick *et al.* in Ref. [214], which reveals connections between statistical mechanics and combinatorial optimization by introducing a temperature-like variable that gives rise to efficient search for global optimum. There exist numerous reviews about simulated annealing that argue the algorithm in deep detail [215, 216, 217, 218, 219].

Some main problems of bioinformatics, onto which the simulated annealing methods have been applied during the last two decades, include phylogenetic tree search [220], homology modeling [221], improvement of threading-based protein models [222], secondary structure alignment [223, 224], tertiary structure prediction [225, 226, 227], RNA/DNA/protein multiple/pair sequence alignments [223, 228, 229, 230, 231, 232, 233].

We investigated if and how simulated annealing can be applied onto sequence alignment problem, for which the widely accepted method of solution is an application of dynamic programming, namely the Needleman–Wunsch algorithm [234] of time complexity $\mathcal{O}(N^2)$ for aligning two sequences both of length N. We studied the case of equal sequence lengths for simplicity, while the procedure can be well generalized to different sequence lengths. Our time complexity analysis suggests simulated annealing being better than the Needleman–Wunsch algorithm for sequences of lengths longer than median protein lengths, for which the optimal alignment cost deviation saturates to a fair value. It should be noted that the Needleman–Wunsch algorithm yields the exact optimal alignment, but cannot be extended to multiple sequence alignment, while this extension can be easily implemented for simulated annealing.

Briefly, the problem is how to match given amino acid sequences of different protein chains (or nucleotide sequences of DNA/RNA chains). A huge collection of experimental data on sequences has been obtained in the life sciences in recent decades that needs to be analysed. By performing sequence alignment analysis,

one can have an idea of how species evolved, which regions of sequences were conserved during evolution, and answer to other related questions.

BLOSUM (BLOcks of amino acid SUbstitution Matrix) [235] and PAM (Point Accepted Mutation) [236] matrices have been developed in order to compare the matching (or mismatching) between different residues of a protein chain. Basically, these 20×20 matrices constitute the scores (energy benefit or negative of energy cost in simulated annealing jargon) of exchanging two type of amino acids, with the diagonal (off-diagonal) elements corresponding to matching (mismatching) scores. In our calculations, we used the BLOSUM80 matrix, B, with each element multiplied by -1, and a gap opening penalty of $g = +8$, in order to make the optimization procedure a cost minimization one for conventionality. In general, given two sequences X and Y , having elements $\{x_i\}$ and $\{y_j\}$, the objective of sequence alignment is minimizing the cost function C given with the relation,

$$C = \sum_{\text{all path}} c_{ij} \quad , \quad c_{ij} = \begin{cases} B(x_i, y_j) & , \text{ for a mis/match between } x_i \text{ and } y_j \\ g & , \text{ for a gap in either sequence} \end{cases} . \tag{6.5}$$

Our careful calculations led the results summarized in Fig.6.2, in which we present a time complexity comparison of simulated annealing and Needleman–Wunsch algorithms. From this analysis, we observe that the simulated annealing provides faster implementations than the Needleman–Wunsch algorithm for sequences of length greater than 325, the number which is close to the median lengths of proteins (361 for Eukaryotes, 267 for Bacteria, and 247 for Archaea) [237]. In example, considering the fact that length of proteins can extend to several thousands, for aligning two sequences both of length 1000, simulated annealing offers 34% improvement in computational time over the Needleman–Wunsch algorithm.

Computation time improvement scales up with increasing sequence length as seen in Fig. 6.2. However, the complementary price for this improvement is that, simulated annealing does not provide the exact global optimum alignment, but a probabilistic one. We compared the results obtained by simulated annealing with the exact results for different lengths of aligned sequences. The deviation in

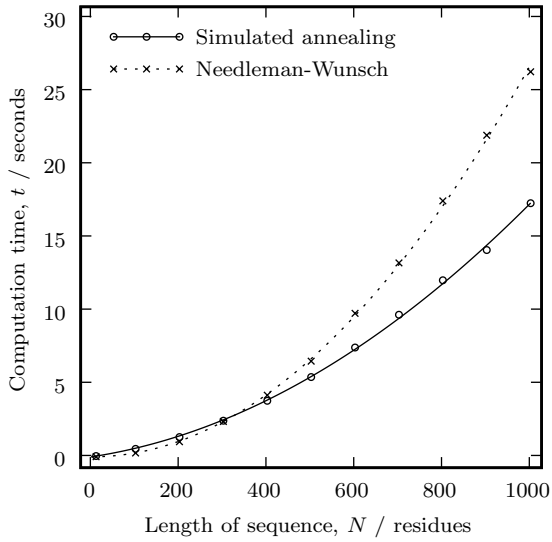

Figure 6.2: Complexity behavior of the simulated annealing (circles and solid line) and Needleman–Wunsch (crosses and dotted line) algorithms. Data points are obtained by averaging over 20 distinct runs of the implemented algorithms, and error bars are smaller than the markers. Lines denote fit results of $t = uN + vN^2$ for simulated annealing and $t = wN^2$ for the Needleman–Wunsch algorithm, with $u = (4.58865 \pm 0.19897) \times 10^3$ s/r, $v = (1.27525 \pm 0.02488) \times 10^5$ s/r^2, and $w = (2.67972 \pm 0.01143) \times 10^5$ s/r^2.

optimal cost is calculated by $\Delta C_o = C_o - C_o^*$, where C_o is the cost of the optimal solution obtained by simulated annealing and C_o^* is the exact minimal cost. The costs are calculated using BLOSUM80 multiplied by -1, for which the elements range in 24 units of cost, and for two different gap penalty values, namely, for $g = 8$, which is a standard value for BLOSUM80, and for a smaller gap penalty of $g = 3$. It is observed that the deviation in optimal cost per residue $\Delta C_o/N$, saturates to an approximate value of 3.3 units of cost in a large N limit for $g = 8$, while this saturation value becomes even smaller for decreasing gap penalty (approximately 2.0 units of cost for $g = 3$), as can be seen in Fig. 6.3 below, in which we present $\Delta C_o/N$ for $N \leqslant 1000$ by circles and squares for $g = 8$ and $g = 3$ respectively. Therefore, we conclude that the increase in computation time improvement does not yield worse results in the optimal alignment path.

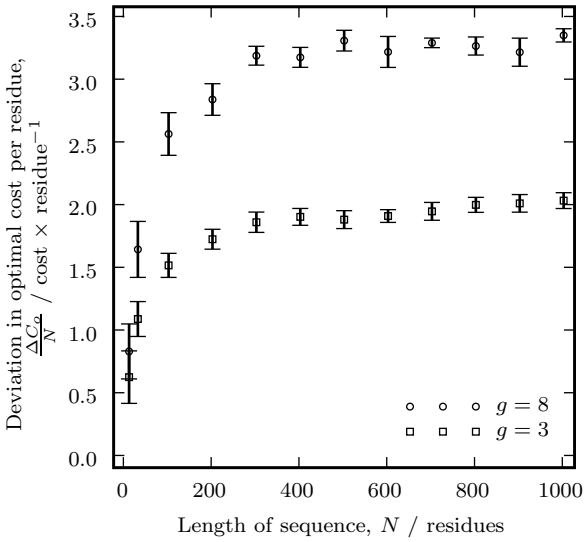

Figure 6.3: Deviations in optimal cost per residue plotted versus aligned sequence length for two different gap penalties of $g = 8$ and $g = 3$. The data and error bars are obtained by the means and standard deviations of 20 distinct runs for each N and g represented. It can be observed that for the standard gap penalty of $g = 8$ for BLOSUM80, the deviation in optimal cost per residue saturates to 3.3 units of cost for large N limit.

6.3 Molecular dynamics of water flow through CNTs

The very basic idea underlying molecular dynamics (MD) simulations is performing a work in the interplay of theory and experiment. It can be considered as the test of known theory. Essentially, the input is the theoretically known force fields, and the output is the dynamical evolution of the system. The MD scheme can be shortly summarized in four steps: (*i*) initializing the system of interest, thus assigning initial positions and velocities to the constituents of the system; (*ii*) calculating the forces acting on each constituent; (*iii*) moving each constituent under these forces for a very short period of time, thus updating their positions and velocities; and (*iv*) repeating the last two steps above as long as needed. This scheme yields the positions and velocities of each constituent at each time step, thus a microscopic evolution of the system. Experimentally observable macroscopic quantities can be in general related to the averages of microscopic quatities. A fairly basic example is the temperature of a dilute gas in a container, which actually is related to the average of velocities of the gas molecules.

In practice, there are several issues one has to consider while, or better before, performing MD simulations on a computer. The most common issue is the computation time problem. Since we want to simulate systems in thermodynamic limit, we deal with large number of particles. Practically achievable numbers are in the order of 10^3, which is much more smaller than the Avogadro's number, but large enough to cause huge computation times. Thus, the first problem one encounters is finding an effective way to perform steps (*ii*) and (*iii*) above. Moreover, the integration of forces is another issue, since computers are digital machines. Basically, the art of MD is finding an optimum trade-off between computation time and accuracy. We will not go into the details of practical MD simulations, but we must mention that the optimization problem in MD is solved by using several different methods. Among these, the principal ones are using peridiodic boundary conditions, truncating the short-range Lennard–Jones interactions by simple or shifted truncation, Ewald summing the long-range Coulomb interactions, and integrating the forces with higher order Taylor expansion algorithms.

Using each of the principle and widely accepted techniques mentioned above, one is performing an approximate work. In example, in the simple truncation scheme of Lennard–Jones potential, one assumes that the interactions vanish at a certain cut-off distance, r_c. This would yield artificial results for a system in which the typical interatomic distance is around r_c. Here, r_c is only one of the many defined simulation parameters, and one has to find the optimum simulation parameters for a particular system to simulate.

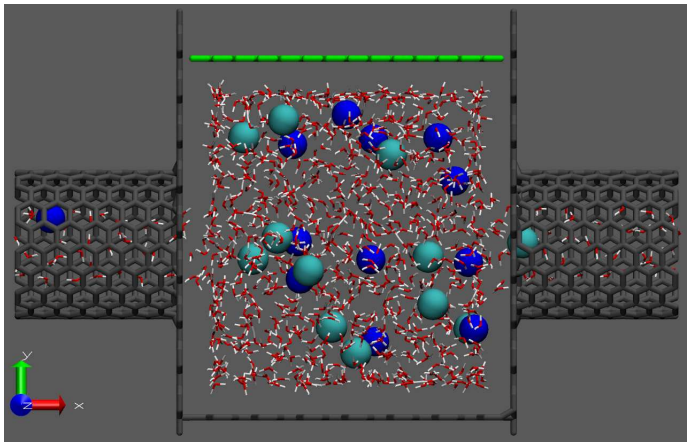

Figure 6.4: A typical system of ion solution flowing through a CNT that we use in our MD simulations. The simulation box contains $\sim 10^3$ water molecules, denoted by white H and red O atoms. The ions shown by spheres are Na^+ (blue) and Cl^- (cyan). The solution reservoir is formed from frozen graphene (two in yz-plane on left and right and one in xz-plane bottom), and together with the frozen CNT, they are shown in dark gray. The periodic boundary condition in x-direction assures an atom leaving the CNT from one end entering it through the opposite. Thus the CNTs at both ends are actually two parts of a single CNT. The single graphene sheet on top, shown in green, is used as a piston. We apply constant force onto this piston in $-y$-direction for pressure coupling, since we figured out that the standard pressure coupling algorithms cannot handle this type of systems properly due to large vacuum regions. Once we fill those irrelevant regions with water, we have to pay for the extra computational cost, that will double the required memory space and computation time.

We obtained a working scheme for studying the water flow through carbon nanotubes (CNTs). Using this set of simulation parameters we are investigating the ionic solutions, *e.g.*, a NaCl solution in water, flowing through CNTs (*cf.* Fig. 6.4). Our aim is to develop a nanoscale filter for anion-cation separation, thus, an electromechnanical power generator.

BIBLIOGRAPHY

[1] J. J. Thomson, The Electrician **39**, 104 (1897).

[2] P. K. L. Drude, Ann. Phys. (Leipzig) **1**, 566 (1900).

[3] P. K. L. Drude, Ann. Phys. (Leipzig) **3**, 369 (1900).

[4] P. K. L. Drude, Ann. Phys. (Leipzig) **7**, 687 (1902).

[5] H. A. Lorentz, *The Theory of Electrons and its Applications to the Phenomena of Light and Radiant Heat* (Dover, New York, NY 1952).

[6] A. Sommerfeld, Z. Phys. **47**, 1 (1928).

[7] W. Friedrich, P. Knipping, and M. von Laue, in *Sitzungsberichte der Kniglich Bayerischen Akademie der Wissenschaften* (Munich, Germany 1912), p. 303.

[8] M. von Laue, in *Sitzungsberichte der Kniglich Bayerischen Akademie der Wissenschaften* (Munich, Germany 1912), p. 363.

[9] M. von Laue, Ann. Phys. **41**, 971 (1913).

[10] W.L. Bragg, Proc. Cambridge Philos. Soc. **17**, 43 (1913).

[11] F. Bloch, Z. Phys. **52**, 555 (1928).

[12] F. Hund, Z. Phys. **36**, 657 (1926).

[13] F. Hund, Z. Phys. **40**, 742 (1927).

[14] F. Hund, Z. Phys. **42**, 93 (1927).

[15] F. Hund, Z. Phys. **43**, 805 (1927).

[16] F. Hund, Z. Phys. **51**, 759 (1928).

[17] F. Hund, Z. Phys. **63**, 719 (1930).

[18] R. S. Mulliken, Proc. Natl. Acad. Sci. U.S.A., **112**, 144 (1926).

[19] R. S. Mulliken, Phys. Rev. **29**, 637 (1927).

[20] R. S. Mulliken, Phys. Rev. **32**, 186 (1928).

[21] R. S. Mulliken, Phys. Rev. **32**, 761 (1928).

[22] R. S. Mulliken, Phys. Rev. **40**, 55 (1932).

[23] B. N. Finkelstein and G. E. Horowitz, Z. Phys. **48**, 118 (1928).

[24] J. E. Lennard-Jones, Trans. Faraday Soc. **25**, 668 (1929).

[25] J. C. Slater and G. F. Koster, Phys. Rev. **94**, 1498 (1954).

[26] M. Born and J. R. Oppenheimer, Ann. Phys. **84**, 457 (1927).

[27] D. R. Hartree, Proc. Cambridge Philos. Soc. **24**, 89 (1928).

[28] J. C. Slater, Phys. Rev. **34**, 1293 (1929).

[29] V. Fock, Z. Phys. **61**, 126 (1930).

[30] P. Hohenberg and W. Kohn, Phys. Rev. B **136**, 864 (1964).

[31] W. Kohn and L. J. Sham, Phys. Rev. A **140**, 1133 (1965).

[32] N. W. Ashcroft and N. D. Mermin, *Solid State Physics* (Harcourt, Orlando, FL 1976).

[33] A. M. Zagoskin, *Quantum Theory of Many-Body Systems: Techniques and Applications*, (Springer, New York, NY 1998).

[34] M. P. Marder, *Condensed Matter Physics* (Wiley, New York, NY 2000).

[35] P. L. Taylor and O. Heinonen, *A Quantum Approach to Condensed Matter Physics* (Cambridge University, Cambridge, UK 2002).

[36] U. Mizutani, *Introduction to the Electron Theory of Metals* (Cambridge University, Cambridge, UK 2004).

[37] F. Duan and J. Guojun, *Intoduction to Condensed Matter Physics* (World Scientific, Singapore, 2005).

[38] H. Bruus and K. Flensberg, *Introduction to Many-Body Quantum Theory in Condensed Matter Physics* (Oxford University, Oxford, UK 2009).

[39] L. M. Sander, *Advanced Condensed Matter Physics* (Cambridge University, Cambridge, UK 2009).

[40] J. N. Lalena and D. A. Cleary, *Principles of Inorganic Materials Design* (Wiley, Hoboken, NJ 2010).

[41] *Encyclopedic Dictionary of Condensed Matter Physics* edited by C. P. Poole Jr. (Elsevier, Amsterdam, The Netherlands 2004).

[42] *Encyclopedia of Condensed Matter Physics* edited by F. Bassani, G. L. Liedl, and P. Wyder (Elsevier, Amsterdam, The Netherlands 2005).

[43] N. Jarosik, C. L. Bennett, J. Dunkley, B. Gold, M. R. Greason, M. Halpern, R. S. Hill, G. Hinshaw, A. Kogut, E. Komatsu, D. Larson, M. Limon, S. S. Meyer, M. R. Nolta, N. Odegard, L. Page, K. M. Smith, D. N. Spergel, G. S. Tucker, J. L. Weiland, E. Wollack, and E. L. Wright, Astrophys. J. Suppl. Ser. **192**, 14 (2011).

[44] P. Fazekas, *Lecture Notes on Electron Correlation and Magnetism (Series on Modern Condensed Matter Physics, Vol. 5)*, (World Scientific, Singapore 2003).

[45] W. Heitler and F. London, Z. Phys. **44**, 455 (1927).

[46] W. Heisenberg, Z. Phys. **38**, 411 (1926).

[47] P. A. M. Dirac, Proc. R. Soc. London, Sect A **112**, 661 (1926).

[48] P. W. Anderson, Phys. Rev. **115**, 2 (1959).

[49] L. N. Bulaevskii, Zh. Eksp. Teor. Fiz. **51**, 230 (1966) [Sov. Phys. JETP **24**, 154 (1967)].

[50] D. J. Klein and W. A. Seitz, Phys. Rev. B **8**, 2236 (1973).

[51] J. Florêncio, Jr., and K. A. Chao, Phys. Rev. Lett. **35**, 741 (1975).

[52] J. Florêncio, Jr., and K. A. Chao, Phys. Rev. B **14**, 3121 (1976).

[53] C. L. Cleveland and R. Medina A., Am. J. Phys. **44**, 44 (1976).

[54] M. Takahashi, J. Phys. C **10**, 1289 (1977).

[55] K. A. Chao, J. Spałek, and A. M. Oleś, J. Phys. C **10**, L271 (1977).

[56] K. A. Chao, J. Spałek, and A. M. Oleś, Phys. Rev. B **18**, 3453 (1978).

[57] C. Gros, R. Joynt, and T. M. Rice, Phys. Rev. B **36**, 381 (1987).

[58] A. H. MacDonald, S. M. Girvin, and D. Yoshioka, Phys. Rev. B **37**, 9753 (1988).

[59] G. R. Stewart, Rev. Mod. Phys. **56**, 755 (1984).

[60] M. Imada, A. Fujimori, and Y. Tokura, Rev. Mod. Phys. **70**, 1039 (1998).

[61] K. Byczuk, in *Condensed Matter Physics in the Prime of the 21st Century: Phenomena, Materials, Ideas, Methods*, edited by J. Jędrzejewski (World Scientific, Singapore 2008), p. 1.

[62] W. Heisenberg, Z. Phys. **43**, 172 (1927).

[63] J. H. de Boer and E. J. W. Verwey, Proc. Phys. Soc. London **49**, 59 (1937).

[64] N. F. Mott and R. Peierls, Proc. Phys. Soc. London, **49**, 72 (1937).

[65] M. Roilos and P. Nagels, Solid State Commun. **2**, 285 (1964).

[66] B. Fisher and D. S. Tannhauser, J. Chem. Phys. **44**, 1663 (1966).

[67] J. G. Bednorz and K. A. Müller, Z. Phys. B **64**, 189 (1986).

[68] R. von Helmolt, J. Wecker, B. Holzapfel, L. Schultz, and K. Samwer, Phys. Rev. Lett. **71**, 2331 (1993).

[69] S. Jin, T. H. Tiefel, M. McCormack, R. A. Fastnacht, R. Ramesh, and L. H. Chen, Science **264**, 413 (1994).

[70] D. B. McWhan, A. Menth, J. P. Remeika, W. F. Brinkman, and T. M. Rice, Phys. Rev. B **7**, 1920 (1973).

[71] S. Yu. Ezhov, V. I. Anisimov, D. I. Khomskii, and G. A. Sawatzky, Phys. Rev. Lett. **83**, 4136 (1999).

[72] N. F. Mott, *Metal-Insulator Transitions*, (Taylor & Francis, London, UK 1990).

[73] N. F. Mott, Proc. Phys. Soc. London, Sect. A *62*, 416 (1949).

[74] N. F. Mott, Can. J. Phys. *34*, 1356 (1956).

[75] N. F. Mott, Philos. Mag. *6*, 287 (1961).

[76] N. F. Mott, Rev. Mod. Phys. **40**, 677 (1968).

[77] J. Hubbard, Proc. R. Soc. London, Sect. A **276**, 238 (1963).

[78] J. Hubbard, Proc. R. Soc. London, Sect. A **277**, 237 (1964).

[79] J. Hubbard, Proc. R. Soc. London, Sect. A **281**, 401 (1964).

[80] D. Bohm and D. Pines, Phys. Rev. **82**, 625 (1951).

[81] D. Pines and D. Bohm, Phys. Rev. **85**, 338 (1952).

[82] D. Bohm and D. Pines, Phys. Rev. **92**, 609 (1953).

[83] D. Davis, Phys. Rev. B **7**, 129 (1973).

[84] W. Heiseberg, Z. Phys. **33**, 879 (1925).

[85] P. A. M. Dirac, Proc. R. Soc. London, Sect. A **109**, 642 (1925).

[86] E. Schrödinger, Ann. Phys. (Leipzig) **79**, 361 (1926).

[87] E. Schrödinger, Ann. Phys. (Leipzig) **79**, 489 (1926).

[88] E. Schrödinger, Ann. Phys. (Leipzig) **79**, 734 (1926).

[89] E. Schrödinger, Ann. Phys. (Leipzig) **80**, 437 (1926).

[90] E. Schrödinger, Ann. Phys. (Leipzig) **81**, 109 (1926).

[91] P. A. M. Dirac, Proc. R. Soc. London, Sect. A **114**, 243 (1927).

[92] P. A. M. Dirac, Proc. R. Soc. London, Sect. A **114**, 710 (1927).

[93] P. Jordan and E. Wigner, Z. Phys. **47**, 631 (1928).

[94] A. A. Abrikosov, L. P. Gor'kov, and I. Ye. Dzyaloshinskii, *Quantum Field Theoretical Methods in Statistical Physics* (Pergamon, Oxford, UK 1965).

[95] G. D. Mahan, *Many-Particle Physics* (Kluwer Academic, New York, NY 2000).

[96] A. L. Fetter and J. D. Walecka, *Quantum Theory of Many-Particle Systems* (Dover, New York, NY 2003).

[97] M. Cini, *Topics and Methods in Condensed Matter Theory: From Basic Quantum Mechanics to the Frontiers of Research* (Springer, Berlin, Germany 2007).

[98] A. Altland and B. Simons, *Condensed Matter Field Theory* (Cambridge University, Cambridge, UK 2010).

[99] K. G. Wilson, Phys. Rev. B **4**, 3174 (1971).

[100] M. Suzuki and H. Takano, Phys. Lett. A **69**, 426 (1979).

[101] H. Takano and M. Suzuki, J. Stat. Phys. **26**, 635 (1981).

[102] A. Falicov and A. N. Berker, Phys. Rev. B **51**, 12458 (1995).

[103] P. Tomczak, Phys. Rev. B **53**, R500 (1996).

[104] P. Tomczak and J. Richter, Phys. Rev. B **54**, 9004 (1996).

[105] P. Tomczak and J. Richter, J. Phys. A **36**, 5399 (2003).

[106] M. Hinczewski and A. N. Berker, Eur. Phys. J. B **48**, 1 (2005).

[107] M. Hinczewski and A. N. Berker, Eur. Phys. J. B **51**, 461 (2006).

[108] M. Hinczewski and A. N. Berker, Phys. Rev. B **78**, 064507 (2008).

[109] O. S. Sarıyer, A. N. Berker, and M. Hinczewski, Phys. Rev. B **77**, 134413 (2008).

[110] C. N. Kaplan and A. N. Berker, Phys. Rev. Lett. **100**, 027204 (2008).

[111] C. N. Kaplan, A. N. Berker, and M. Hinczewski, Phys. Rev. B **80**, 214529 (2009).

[112] M. Suzuki, Phys. Lett. A **146**, 319 (1990).

[113] A. A. Migdal, Zh. Eksp. Teor. Fiz. **69**, 1457 (1975) [Sov. Phys. JETP **42**, 743 (1976)].

[114] L. P. Kadanoff, Ann. Phys. (N.Y.) **100**, 359 (1976).

[115] A. N. Berker and S. Oslund, J. Phys. C **12**, 4961 (1979).

[116] M. Kaufman and R. B. Griffiths, Phys. Rev. B **24**, 496 (1981).

[117] M. Kaufman and R. B. Griffiths, Phys. Rev. B **30**, 244 (1984).

[118] S. R. McKay and A. N. Berker, Phys. Rev. B **29**, 1315 (1984).

[119] D. J. Amit, *Field Theory, the Renormalization Group, and Critical Phenomena* (World Scientific, Singapore 1984).

[120] N. Goldenfeld, *Lectures on Phase Transitions and the Renormalization Group* (Perseus, Reading, MA 1992).

[121] M. E. Fisher, Rev. Mod. Phys. **70**, 653 (1998).

[122] M. E. Fisher, in *Lecture Notes in Physics, Vol. 186, Critical Phenomena*, edited by F. J. W. Hahne (Springer, Berlin, Germany 1983), p. 1.

[123] L. M. Falicov and J. C. Kimball, Phys. Rev. Lett. **22**, 997 (1969).

[124] R. Ramirez, L. M. Falicov, and J. C. Kimball, Phys. Rev. B **2**, 3383 (1970).

[125] R. Ramirez and L. M. Falicov, Phys. Rev. B **3**, 2425 (1971).

[126] C. E. T. Gonçalves da Silva and L. M. Falicov, J. Phys. C **5**, 906 (1972).

[127] M. Plischke, Phys. Rev. Lett. **28**, 361 (1972).

[128] T. Kennedy and E. H. Lieb, Physica A **138**, 320 (1986).

[129] E. H. Lieb, Physica A **140**, 240 (1986).

[130] J. K. Freericks and L. M. Falicov, Phys. Rev. B **41**, 2163 (1990).

[131] J. K. Freericks, Phys. Rev. B **47**, 9263 (1993).

[132] U. Brandt, A. Fledderjohann, and G. Hülsenbeck, Z. Phys. B **81**, 409 (1990).

[133] P. Farkašovský, Phys. Rev. B **60**, 10776 (1999).

[134] V. Zlatić, J. K. Freericks, R. Lemański, and G. Czycholl, Phil. Mag. B **81**, 1443 (2001).

[135] T. Minh-Tien, Phys. Rev. B **67**, 144404 (2003).

[136] R. Lemański, Phys. Rev. B **71**, 035107 (2005).

[137] P. Farkašovský and H. Čenčariková, Eur. Phys. J. B **47**, 517 (2005).

[138] P. M. R. Brydon and M. Gulácsi, Phys. Rev. B **73**, 235120 (2006).

[139] V. Zlatić and J. K. Freericks, Acta Phys. Pol. B **32**, 3253 (2001).

[140] V. Zlatić and J. K. Freericks, in *Open Problems in Strongly Correlated Electron Systems*, edited by J. Bonča, P. Prelovšek, A. Ramšak, and S. Sarkar, NATO ARW, Sci. Ser. II, Vol. 15 (Kluwer Academic, Dordrecht, The Netherlands 2001), p. 371.

[141] V. Zlatić and J. K. Freericks, in *Concepts in Electron Correlation*, edited by A. C. Hewson and V. Zlatić, NATO ARW, Sci. Ser. II, Vol. 110 (Kluwer Academic, Dordrecht, The Netherlands 2003), p. 287.

[142] P. Miller and J. K. Freericks, J. Phys.: Condens. Matter **13**, 3187 (2001).

[143] J. K. Freericks, B. N. Nikolić, and P. Miller, Phys. Rev. B **64**, 054511 (2001); **68**, 099901(E) (2003).

[144] J. K. Freericks, B. N. Nikolić, and P. Miller, Int. J. Mod. Phys. B **16**, 531 (2002).

[145] R. Allub and B. Alascio, Solid State Commun. **99**, 613 (1996).

[146] R. Allub and B. Alascio, Phys. Rev. B **55**, 14113 (1997).

[147] B. M. Letfulov and J. K. Freericks, Phys. Rev. B **64**, 174409 (2001).

[148] T. V. Ramakrishnan, H. R. Krishnamurthy, S. R. Hassan, and G. Venketeswara Pai, in *Colossal Magnetoresistive Manganites*, edited by T. Chatterji (Kluwer Academic, Dordrecht, The Netherlands 2003), p. 417.

[149] H. J. Leder, Solid State Commun. **27**, 579 (1978).

[150] J. M. Lawrence, P. S. Riseborough, and R. D. Parks, Rep. Prog. Phys. **44**, 1 (1981).

[151] W. Hanke and J. E. Hirsch, Phys. Rev. B **25**, 6748 (1982).

[152] E. Baeck and G. Czycholl, Solid State Commun. **43**, 89 (1982).

[153] S. H. Liu and K.-M. Ho, Phys. Rev. B **28**, 4220 (1983).

[154] S. H. Liu and K.-M. Ho, Phys. Rev. B **30**, 3039 (1984).

[155] T. Portengen, Th. Östreich, and L. J. Sham, Phys. Rev. B **54**, 17452 (1996).

[156] P. M. R. Brydon and M. Gulácsi, Phys. Rev. Lett. **96**, 036407 (2006).

[157] R. Kotecký and D. Ueltschi, Commun. Math. Phys. **206**, 289 (1999).

[158] C. D. Batista, Phys. Rev. Lett. **89**, 166403 (2002); **90**, 199901(E) (2003).

[159] W.-G. Yin, W. N. Mei, C.-G. Duan, H.-Q. Lin, and J. R. Hardy, Phys. Rev. B **68**, 075111 (2003).

[160] C. D. Batista, J. E. Gubernatis, J. Bonča, and H. Q. Lin, Phys. Rev. Lett. **92**, 187601 (2004).

[161] D. Ueltschi, J. Stat. Phys. **116**, 681 (2004).

[162] K. Michielsen and H. De Raedt, Phys. Rev. B **59**, 4565 (1999).

[163] D. Thanh-Hai and T. Minh-Tien, J. Phys.: Condens. Matter **13**, 5625 (2001).

[164] Z. Gajek and R. Lemański, Acta. Phys. Pol. B **32**, 3473 (2001).

[165] J. Wojtkiewicz and R. Lemański, Phys. Rev. B **64**, 233103 (2001).

[166] H. Čenčariková and P. Farkašovský, Int. J. Mod. Phys. B **18**, 357 (2004).

[167] H. Čenčariková and P. Farkašovský, Phys. Stat. Sol. B **244**, 1900 (2007).

[168] Ch. Gruber, N. Macris, A. Messager, and D. Ueltschi, J. Stat. Phys. **86**, 57 (1997).

[169] J. K. Freericks and V. Zlatić, Phys. Rev. B **58**, 322 (1998).

[170] J. Wojtkiewicz, J. Stat. Phys. **123**, 585 (2006).

[171] Ch. Gruber and N. Macris, Helv. Phys. Acta **69**, 850 (1996).

[172] J. Jędrzejewski and R. Lemański, Acta Phys. Pol. B **32**, 3243 (2001).

[173] J. K. Freericks and V. Zlatić, Rev. Mod. Phys. **75** 1333 (2003).

[174] Ch. Gruber and D. Ueltschi, in *Encyclopedia of mathematical physics*, edited by J.-P. Françoise, G. L. Naber, and T. S. Tsun (Academic, Oxford, UK 2006), Vol. 2, p. 283.

[175] J. K. Freericks, B. N. Nikolić, and P. Miller, Appl. Phys. Lett. **82**, 970 (2003); **83**, 1275(E) (2003).

[176] V. Subrahmanyam and M. Barma, J. Phys. C **21**, L19 (1988).

[177] J. K. Freericks and T. P. Devereaux, Phys. Rev. B **64**, 125110 (2001).

[178] J. K. Freericks, Ch. Gruber, and N. Macris, Phys. Rev. B **53**, 16189 (1996).

[179] J. K. Freericks, E. H. Lieb, and D. Ueltschi, Phys. Rev. Lett. **88**, 106401 (2002).

[180] J. K. Freericks, E. H. Lieb, and D. Ueltschi, Commun. Math. Phys. **227**, 243 (2002).

[181] U. Brandt and R. Schmidt, Z. Phys. B **63**, 45 (1986).

[182] U. Brandt and R. Schmidt, Z. Phys. B **67**, 43 (1987).

[183] A. P. Ramirez, P. Schiffer, S-W. Cheong, C. H. Chen, W. Bao, T. T. M. Palstra, P. L. Gammel, D. J. Bishop, and B. Zegarski, Phys. Rev. Lett. **76**, 3188 (1996).

[184] C. H. Chen and S-W. Cheong, Phys. Rev. Lett. **76**, 4042 (1996).

[185] P. G. Radaelli, D. E. Cox, M. Marezio, and S-W. Cheong, Phys. Rev. B **55**, 3015 (1997).

[186] Y. Moritomo, H. Kuwahara, Y. Tomioka, and Y. Tokura, Phys. Rev. B **55**, 7549 (1997).

[187] Y. Murakami, H. Kawada, H. Kawata, M. Tanaka, T. Arima, Y. Moritomo, and Y. Tokura, Phys. Rev. Lett. **80**, 1932 (1998).

[188] E. Dagotto, *Nanoscale Phase Separation and Colossal Magnetoresistance: The Physics of Manganites and Related Compounds (Springer Series in Solid-State Sciences, Vol. 136)* (Springer, Berlin, Germany 2003).

[189] K. M. Shen, F. Ronning, D. H. Lu, F. Baumberger, N. J. C. Ingle, W. S. Lee, W. Meevasana, Y. Kohsaka, M. Azuma, M. Takano, H. Takagi, and Z.-X. Shen, Science **307**, 901 (2005).

[190] N. Datta, R. Fernández, and J. Fröhlich, J. Stat. Phys. **96**, 545 (1999).

[191] C. Gruber, J. Iwanski, J. Jedrzejewski, and P. Lemberger, Phys. Rev. B **41**, 2198 (1990).

[192] I. Stasyuk, in *Order, Disorder and Criticality: Advanced Problems of Phase Transition Theory*, edited by Y. Holovatch (World Scientific, Singapore 2007), Vol. 2, p. 231.

[193] A. N. Berker and M. Wortis, Phys. Rev. B **14**, 4946 (1976).

[194] M. Vojta, Phys. Rev. B **66**, 104505 (2002).

[195] T. Hanaguri, C. Lupien, Y. Kohsaka, D.-H. Lee, M. Azuma, M. Takano, H. Takagi, and J. C. Davis, Nature **430**, 1001 (2004).

[196] M. Iskin and J. K. Freericks, Phys. Rev. A **80**, 053623 (2009).

[197] R. R. Netz and A. N. Berker, Phys. Rev. Lett. **66**, 377 (1991).

[198] R. R. Netz and A. N. Berker, J. Appl. Phys. **70**, 6074 (1991).

[199] J. R. Banavar, M. Cieplak, and A. Maritan, Phys. Rev. Lett. **67**, 1807 (1991).

[200] R. R. Netz and A. N. Berker, Phys. Rev. Lett. **67**, 1808 (1991).

[201] R. R. Netz, Phys. Rev. B **46**, 1209 (1992).

[202] R. R. Netz, Phys. Rev. B **48**, 16113 (1993).

[203] A. N. Berker, A. Kabakçıoğlu, R. R. Netz, and M. C. Yalabık, Turk. J. Phys. **18**, 354 (1994).

[204] A. Kabakçıoğlu, A. N. Berker, and M. C. Yalabık, Phys. Rev. E **49**, 2680 (1994).

[205] E. A. Ames and S. R. McKay, J. Appl. Phys. **76**, 6197 (1994).

[206] G. B. Akgüç and M. C. Yalabık, Phys. Rev. E **51**, 2636 (1995).

[207] J. E. Tesiero and S. R. McKay, J. Appl. Phys. **79**, 6146 (1996).

[208] J. L. Monroe, Phys. Lett. A **230**, 111 (1997).

[209] A. Pelizzola and M. Pretti, Phys. Rev. B **60**, 10134 (1999).

[210] A. Kabakçıoğlu, Phys. Rev. E **61**, 3366 (2000).

[211] H. Kaya and A. N. Berker, Phys. Rev. E **62**, R1469 (2000).

[212] O. S. Sarıyer and C. Güven, Physica A **389**, 3007 (2010).

[213] N. Metropolis, *et al.*, J. Chem. Phys. **21**, 1087 (1953).

[214] S. Kirkpatrick, C. D. Gelatt Jr., and M. P. Vecchi, Science **220**, 671 (1983).

[215] D. S. Johnson, *et al.*, Oper. Res. **37**, 865 (1989); **39**, 378 (1991).

[216] S. B. Gelfand, Ph.D. Thesis, Massachusetts Institute of Technology (1987).

[217] P. J. M. van Laarhoven and E. H. L. Aarts, *Simulated Annealing: Theory and Applications* (Kluwer, Dordrecht, The Netherlands 1987).

[218] N. E. Collins, R. W. Egelese, and B. L. Golden, Am. J. Math. Manag. Sci. **8**, 209 (1988).

[219] L. Ingber, Math. Comput. Model. **18**, 29 (1993); Control Cybern. **25**, 33 (1996).

[220] D. Barker, Bioinformatics **20**, 274 (2004).

[221] K. Ogata and H. Umeyama, J. Mol. Graph. Model. **18**, 258 (2000).

[222] A. Kolinski, et al., Proteins **37**, 592 (1999).

[223] S. Lindgreen, P.P. Gardner, and A. Krogh, Bioinformatics **23**, 3304 (2007).

[224] J. Kim, J. R. Cole, and S. Pramanik, Comput. Appl. Biosci. **12**, 259 (1996).

[225] G. Patargias, *et al.*, J. Med. Chem. **49**, 648 (2006).

[226] J. M. Bujnicki, *et al.*, Protein Eng. **14**, 717 (2001).

[227] A. R. Ortiz, *et al.*, Pac. Symp. Biocomput. **2**, 316 (1997).

[228] S.-M. Chen and C.-H. Lin, Int. J. Inform. Manag. Sci. **18**, 97 (2007).

[229] J. M. Keith, *et al.*, Bioinformatics **18**, 1494 (2002).

[230] M. Hernández-Guía, R. Mulet, and S. Rodríguez-Pérez, Phys. Rev. E **72**, 031915 (2005).

[231] H. Huo and V. Stojkovic, in *Proceedings of the 3rd International Conference on Natural Computation, vol. 2* (Hainan, China 2007), p. 270.

[232] Q.-w. Dong, *et al.*, in *Proceedings of the 27th Annual International Conference of the IEEE Engineering in Medicine and Biology Society, vol. 3* (Shanghai, China 2005), p. 2798.

[233] M. F. Omar, *et al.*, in *Proceedings of the 1st International Conference on Information and Communication Technologies: From Theory to Applications* (Damascus, Syria 2004), p. 455.

[234] S. B. Needleman and C. D. Wunsch, J. Mol. Biol. **48**, (1970) 443.

[235] S. Henikoff and J. G. Henikoff, P. Natl. Acad. Sci. U.S.A. **89**, (1992) 10915.

[236] M. O. Dayhoff, R. Schwartz, and B. C. Orcutt, in *Atlas of Protein Sequence and Structure, vol. 5, suppl. 3*, edited by M. O. Dayhoff, (National Biomedical Research Foundation, Washington, D.C 1978), p. 345.

[237] L. Brocchieri and S. Karlin, Nucleic Acids Res. **33**, 3390 (2005).

VITA

Ozan Sabahattin Sarıyer was born in Elbistan, Turkey, on September 2, 1981. Graduating in 1998 from Antalya Metin–Nuran Çakallıklı Anatolian High School, in 1999 he enrolled for the English Preparation Class, and in 2000 for the Physics Engineering Programme both at Istanbul Technical University (ITU). He did recitation teaching in sophomore and junior years based on his freshman year accomplishments. He graduated in High Honor List as the top ranked student among the Physics Department and the second top ranked student among the Faculty of Sciences and Letters in 2004 and was accepted for the M.Sc. Programme in Physics Engineering at ITU in the same year. He graduated as a M.Sc. under the supervision of Prof. Dr. A. Nihat Berker with thesis entitled "*Quantum phenomena in anisotropic XXZ Heisenberg spin chains with ferromagnetic and antiferromagnetic interactions: Renormalization-group calculation*". From 2005 to 2008, he was a research assistant at ITU, where he left after his first year of Ph.D. studies, and transferred to Koç University (KU) to be with his thesis advisor, Professor Berker.

During his doctoral studies, he also received scientific guidance from Dr. Michael Hinczewski (University of Maryland) on practical implementation of RG techniques; from Asst. Prof. Dr. Menderes Işkın (KU) on quantum bosonic lattice models; from Assoc. Prof. Dr. Alkan Kabakçıoğlu (KU) on hard-spin mean-field theory of $\pm J$ spin-glass model, and from Prof. Dr. Roland R. Netz (Technical University Munich) on molecular dynamics simulations of water flow through carbon nanotubes.

He has accepted a post-doctoral researcher position from Prof. Dr. Michael Rubinstein of the University of North Carolina at Chapel Hill (UNC), and expected to continue his studies on polymeric soft matter physics at UNC until 2013.